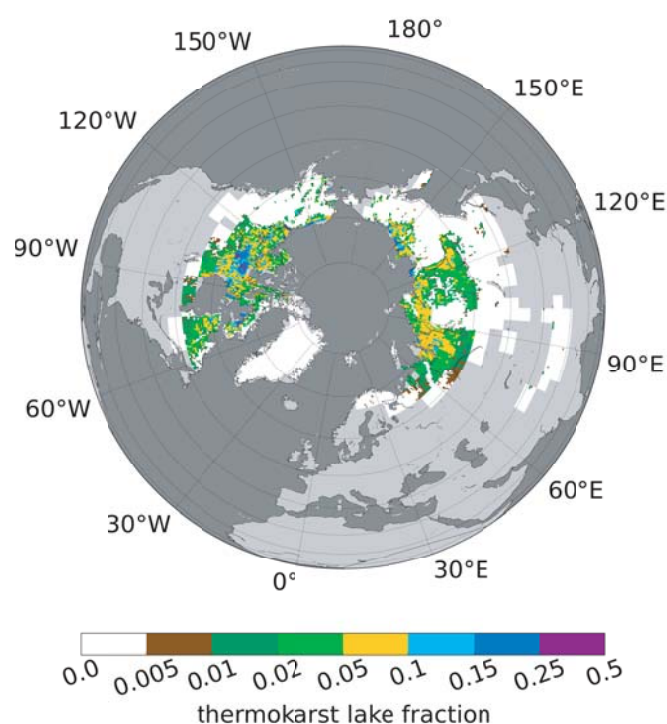




Climate impact on geophysical thermokarst processes during the past 6000 years



Thomas Schöngaßner

Hamburg 2016

Hinweis

Die Berichte zur Erdsystemforschung werden vom Max-Planck-Institut für Meteorologie in Hamburg in unregelmäßiger Abfolge herausgegeben.

Sie enthalten wissenschaftliche und technische Beiträge, inklusive Dissertationen.

Die Beiträge geben nicht notwendigerweise die Auffassung des Instituts wieder.

Die "Berichte zur Erdsystemforschung" führen die vorherigen Reihen "Reports" und "Examensarbeiten" weiter.

Anschrift / Address

Max-Planck-Institut für Meteorologie
Bundesstrasse 53
20146 Hamburg
Deutschland

Tel./Phone: +49 (0)40 4 11 73 - 0

Fax: +49 (0)40 4 11 73 - 298

name.surname@mpimet.mpg.de

www.mpimet.mpg.de

Notice

The Reports on Earth System Science are published by the Max Planck Institute for Meteorology in Hamburg. They appear in irregular intervals.

They contain scientific and technical contributions, including Ph. D. theses.

The Reports do not necessarily reflect the opinion of the Institute.

The "Reports on Earth System Science" continue the former "Reports" and "Examensarbeiten" of the Max Planck Institute.

Layout

Bettina Diallo and Norbert P. Noreiks
Communication

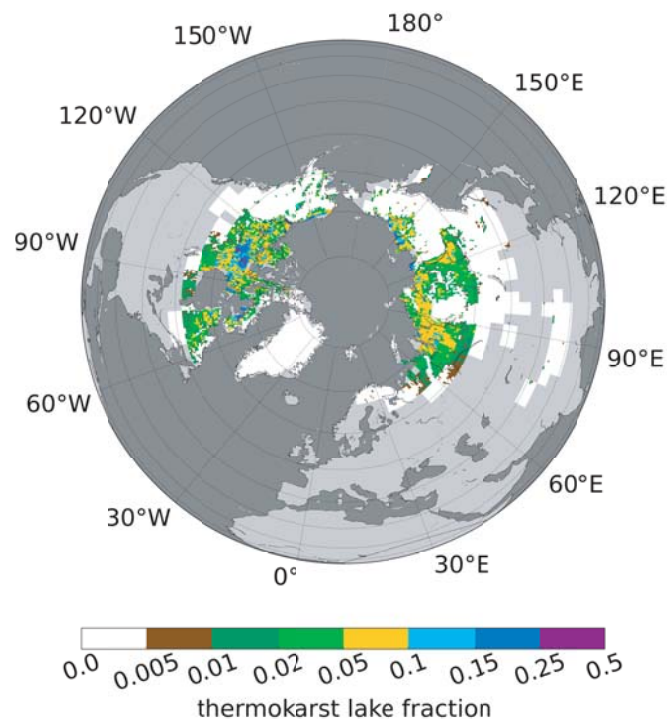
Copyright

Photos below: ©MPI-M

Photos on the back from left to right:
Christian Klepp, Jochem Marotzke,
Christian Klepp, Clotilde Dubois,
Christian Klepp, Katsumasa Tanaka



Climate impact on geophysical thermokarst processes during the past 6000 years



Dissertation with the aim of achieving a doctoral degree
at the Faculty of Mathematics, Informatics and Natural Sciences
Department of Earth Sciences of Universität Hamburg
submitted by

Thomas Schöngaßner

Hamburg 2016

Thomas Schöngaßner

Max-Planck-Institut für Meteorologie
Bundesstrasse 53
20146 Hamburg

Tag der Disputation: 30.11.2015

Folgende Gutachter empfehlen die Annahme der Dissertation:

Prof. Dr. Eva-Maria Pfeiffer
Dr. Stefan Hagemann

Abstract

About one quarter of all land surfaces in the northern hemisphere are underlain by permafrost. Permafrost soils contain a large amount of organic carbon and a destabilization due to the projected future amplitude of Arctic-climate warming might lead to a global-scale feedback mechanism due to enhanced emission of greenhouse gases.

This PhD study focuses on the novel development and evaluation of the first global-scale thermokarst model (TAPAS), which is applied to simulated climate conditions of the past 6000 years. Thermokarst is a coupled thermal-hydrological process, which leads to an enhanced thawing of ice-rich permafrost on local-to-regional scales. The TAPAS model dynamically simulates the development of thermokarst lakes (TKL) and the aggregation of excess-ice. It is developed for a future implementation into JSBACH, the land component of the Max Planck Institute - Earth System Model (MPI - ESM).

The TAPAS model includes the major steps of thermokarst formation. Little ponds develop after disturbance of the surface heat balance, which can be caused by warm summer temperature, high winter snow depth, wildfires, or flood events. The ponds expand to large lakes because of enhanced melting of excess-ice and thawing of adjacent soils until drainage of the lakes due to connection to subterranean drainage passages or river networks. Then empty basins are left and permafrost recovers again and excess-ice aggregates in the interior of the soil.

For present climate, the evaluation of the TAPAS model against satellite based observations shows good agreement of the modelled lake fraction in eastern Siberian lowlands, Lena River delta, Mackenzie River delta, and North Slope of Alaska. The regional distribution of TKL shows potential for improvement because the lake fraction is often overestimated as in Siberia and in northern parts of central Canada. Furthermore several climate scenarios are designed to investigate the responses of thermokarst to climate warming over several millennia. The simulations show that more lakes are formed in periods of climate warming, which agrees well to observations on regional-scale. However, drainage of lakes increases as well because the permafrost area decreases and less excess-ice accumulates, which are the main preconditions for thermokarst. Therefore, a smaller number of TKL is reached on a long-time scale.

In summary, the TAPAS model is able to simulate all principal stages of thermokarst cycle that are known from current research on thermokarst and shows long-term variability of lake covered areas in response to climate change. In future applications the TAPAS model can be introduced into an ESM to improve representation of the surface water balance in high latitudes and to receive hydrological boundary data for biochemical modelling of the permafrost carbon cycle. Overall this PhD thesis constitutes the first step to represent thermokarst processes in an ESM.

Zusammenfassung

Permafrostböden treten in etwa einem Viertel aller Landgebiete in der nördlichen Hemisphäre auf. Sie speichern eine große Menge organischen Kohlenstoff, welcher durch die prognostizierte arktische Klimaerwärmung freigesetzt wird. Dadurch erhöht sich die Emission von Treibhausgasen, was einen positiven Rückkopplungseffekt auslösen könnte.

Das Ziel dieser Doktorarbeit ist die erstmalige Entwicklung und Evaluierung des globalen Thermokarst Modelles (TAPAS). Dieses wird auf die modellierten Klimabedingungen der letzten 6000 Jahre angewendet. Thermokarst ist ein gekoppelter thermisch-hydrologischer Prozess. Dieser führt zu einem verstärkten Auftauen eisreichen Permafrostes auf lokaler bis regionaler Skala. TAPAS modelliert dynamisch die Entwicklung von Thermokarst Seen (TKL) und Exzesseis im Permafrost. Dieses Modell wurde für eine künftige Implementierung in JSBACH konzipiert, die Landkomponente des Max Planck Institut - Erdsystemmodelles (MPI - ESM).

Das TAPAS Modell beschreibt die wichtigsten Prozesse des Thermokarsts. Prinzipiell wird Thermokarst durch eine Störung des Wärmegleichgewichtes an der Bodenoberfläche ausgelöst. Störungen können durch warme Sommer, hohe Winterschneetiefen, Überschwemmungen oder durch Brandereignisse verursacht werden. Dabei entstehen kleine Pfützen. Diese wachsen zu großen Seen heran, da sie das Abtauen des Permafrostes und das Aufschmelzen des Exzesseises begünstigen. Die Seen laufen aus, sobald sie mit einem Fluss oder mit einem unterirdischen Drainagedurchgang in Kontakt kommen. Nach dem Auslaufen bleiben leere Becken übrig, in denen sich der Permafrost wieder zurückbildet und Exzesseis erneut akkumuliert.

Die Evaluierung des TAPAS Modelles mit Satellitenbeobachtungen zeigt eine gute Übereinstimmung des Seenanteiles in der Ostsibirischen Tiefebene, im Lenadelta, im Mackenziedelta und an der Nordküste Alaskas. Die regionale Verteilung der TKL sollte jedoch verbessert werden, da der Seenanteil regional oft überschätzt wird. Des Weiteren wurden mehrere Klimaszenarien entwickelt um mögliche Auswirkungen einer Klimaerwärmung auf einer Zeitskala von mehreren Jahrtausenden zu untersuchen. Die Simulationen zeigen, dass durch die Klimaerwärmung mehr Seen entstehen, was von verschiedenen Feldstudien bestätigt wurde. Allerdings taut auch der Permafrost auf und es bildet sich weniger Exzesseis, was eine Grundvoraussetzung für Thermokarst ist. Dadurch verringert sich die Anzahl an TKL auf langer Zeitskala.

Zusammengefasst kann das TAPAS Modell die wichtigsten beobachteten Thermokarstprozesse simulieren. Zudem reagiert die modellierte Seenfläche sensibel auf Klimaänderungen. Das Modell kann in ein ESM eingebaut werden um die Darstellung der Wasserbilanz in den hohen Breiten zu verbessern. Dabei werden auch Randbedingungen für eine biochemische Modellierung des Permafrost-Kohlenstoffkreislaufes geschaffen. Insgesamt ermöglicht diese Doktorarbeit die Implementierung von Thermokarst in ein ESM.

Contents

1	Introduction	1
1.1	Motivation	1
1.2	Research questions	3
1.3	Structure of the PhD thesis	3
1.4	State of the Art	4
2	Thermokarst distribution in periglacial Arctic environments	7
2.1	Periglacial Arctic climate	7
2.2	Distribution of permafrost soils	11
2.3	Thermokarst landscapes	13
2.3.1	Distribution of thermokarst lakes	14
2.3.2	Mechanisms triggering thermokarst	15
2.3.3	Thermokarst process	16
2.4	Ice rich sediments and massive ice wedges	18
2.4.1	Ice wedge polygons	19
2.4.2	Pingos and palsas	19
3	Development of a dynamic thermokarst module	21
3.1	Set up of a thermokarst model	21
3.1.1	Stages of thermokarst development	22
3.1.2	Age classes and lake properties	23
3.1.3	Overview of driving mechanisms and thresholds	26
3.2	Limitations regarding the formation of water bodies	27
3.2.1	Effects of slope on lake formation	27
3.2.2	Permafrost fraction and lake formation	30
3.3	Formulation of the main thermokarst mechanisms	34
3.3.1	Disturbances and formation of new ponds	34
3.3.2	Development of a talik below thermokarst lakes	40
3.3.3	Lake expansion rate	42
3.3.4	Drainage probability of thermokarst lakes	45
3.3.5	Accumulation of excess-ice	48
3.3.6	Energy balance and lake ice formation	51
3.4	Initialisation of the thermokarst model	52
3.4.1	Slope distribution	54
3.4.2	Excess-ice distribution	56

4	Tuning the dynamic thermokarst module	57
4.1	Reference thermokarst model run driven by CLIMBA	58
4.1.1	Overview of the model parameters and initial setting	58
4.1.2	Improvement of initial parameter settings	60
4.1.3	Results from the Ref-1 model run	62
4.2	Sensitivity to soil parameters	64
4.2.1	Excess-ice aggregation	65
4.2.2	Expansion rate	67
4.2.3	Drainage probability	69
4.3	Sensitivity to climate parameters	72
4.3.1	Infiltration disturbances	73
4.3.2	Temperature disturbance thresholds	74
4.3.3	Snow disturbance thresholds	75
4.3.4	Fire disturbances and surface runoff	75
4.3.5	Climate sensitivity	76
4.3.6	Absolute number of disturbances	79
4.4	Retuning model parameters	80
4.4.1	pore-size and drainage amplification	80
4.4.2	Area of new ponds and ice aggregation time-scale	81
4.4.3	Expansion rate and drainage probability	82
5	Response of thermokarst lakes to potential climate change	85
5.1	Overview of the climate scenarios	86
5.2	Influence of climate change on thermokarst without permafrost changes	88
5.2.1	Temporal evolution until pre-industrial times	88
5.3	Thermokarst distribution under different climates with interactive permafrost	93
5.3.1	Lake fraction under different climates at pre-industrial times	95
6	Uncertainty of thermokarst evolution during the Holocene to different forcing	99
6.1	Forcing of the TAPAS model	100
6.2	Climate of the past 6000 years	101
6.3	Potential thermokarst development of the past 6000 years	103
6.4	Modelled distribution of lakes at pre-industrial times	105
6.4.1	Evaluation of model runs with ECHAM5 and CLIMBA forcing	105
6.4.2	Evaluation against satellite based observations	107
7	Concluding remarks	113
7.1	Summary	113
7.2	Outlook	115
	List of Symbols	117
	List of Abbreviations	119
	Acknowledgements	125

1 Introduction

1.1 Motivation

About 24 % of the northern hemispheric land surface is covered by permafrost (Brown et al., 1997; Zhang et al., 1999). Permafrost is soil, which has been frozen for at least two years in a row. It can be differentiated by its spatial extend, thickness, the amount of ground ice, and its temperature. Ground ice deposits have sometimes accumulated over thousands of years and consist of massive ice bodies of several meters depth (French, 2007). Melting of these ice complexes leads to ground settlement and to accumulation of melting water within the developing depressions. This is a typical form of permafrost degradation, which causes growth of thermokarst lakes (TKL) (Wallace, 1948; Hopkins, 1949). Thermokarst is a very common phenomenon in the Arctic, sub-Arctic, and in Boreal lowland regions with ice-rich unconsolidated sediment deposits (Walter et al., 2007). In comparison to the slow top-down thawing of permafrost, thermokarst causes a rapid and deep permafrost degradation (Grosse et al., 2013). The thermokarst process is triggered by a disturbance of the ground thermal regime. Even though it is small in spatial extend, a widespread and frequent occurrence accumulates thermokarst to a very common feature in most permafrost areas (French, 2007; Grosse et al., 2013). TKL disrupt the surface energy balance in permafrost areas and trigger a feedback mechanism on the ground thermal regime (e.g. Jorgenson et al., 2010). This feedback comprises interactions between snow, permafrost, hydrology, and ecosystems, which include altered energy and water fluxes between atmosphere and land surface.

Most permafrost regions experienced warming and thawing since many decades. The warming trend is predicted to continue during this century (Romanovsky et al., 2010). Due to the Arctic amplification, these regions are prognosticated with larger and earlier impact of the global climate change than other regions on Earth (Hinzman et al., 2005; IPCC, 2007). Therefore, a large change of the hydrological and thermal state can be expected. A variety of climate components like terrestrial vegetation, permafrost, or sea-ice are already responding to the recent climate change (ACIA, 2005; Grosse et al., 2011).

Permafrost soils contain a large amount of soil organic carbon (SOC), which has accumulated over tens of thousands of years during the late Quaternary (Schirrmeister et al., 2011). Organic litter and vegetation have been embedded within fine-grained and frozen deposits. SOC is mostly concentrated within large ice-wedges, which together can reach a depth of up to 40 m. The knowledge about depth and extension of the organic layer allows projections of potentially released amount of Carbon-dioxide (CO₂) and Methane (CH₄) due to microbial decomposition. Approximately 50 % of the estimated global below-ground organic carbon pool is deposited

in the permafrost, which is more than twice the size of the current atmospheric carbon pool (Schuur et al., 2008). In total, between 1400 Pg and 1850 Pg of SOC are stored in permafrost regions (Grosse et al., 2011). However, the numbers are preliminary, because a small number of data points are extrapolated to large regions. For instance, a release of 1 Pg carbon would increase the atmospheric CO₂ concentration by 0.471 ppm (Battle et al., 2000). A destabilization of permafrost soils because of the expected amplitude of future Arctic climate warming would lead to a global-scale positive feedback mechanism due to enhanced emission of greenhouse gases (GHG).

Permafrost related processes are still rudimentary represented in global climate models (GCM) and in Earth system models (ESM). Probably, a large error propagates with projection of future Arctic climate. Since a large amount of carbon is stored within the soils, more precise estimations of amount and rates of GHG emission are needed to improve the climate model performance in high latitudes. Thus, a global scale thermokarst model is developed and discussed in this thesis. This will be the first step of the process to include thermokarst related processes into JSBACH, which fits into very recent developments with regards to permafrost melting and freezing (Ekici et al., 2013) and a dynamical wetland scheme (Stacke and Hagemann, 2012).

The main issue of this dissertation is to develop a thermokarst model for a GCM (Global Climate Model) to provide structural improvements and new parameterizations with regard to heat and water flow. Carbon and nitrogen dynamics are beyond the scope; the main focus is based on geophysical processes. Since thermokarst is a long-term process, which spans over several millennia (French, 2007), the model needs to be able to simulate the evolution of thermokarst lakes over several thousands of years to satisfactorily describe all stages of the thermokarst process. Therefore, the model will be established for the recent Holocene. Driving climate forcing data are available from two different studies, for the past 6000 years (Fischer and Jungclauss, 2010) and for the past 7000 years (Bruecher et al., 2014). There are several climate parameters, which have the potential to highly disturb the sub-soil heat balance and to trigger thermokarst (French, 2007). Detailed observations of TKL are not available for the time period under consideration. Therefore, the aim of this study will be to reach today's distribution of TKL and subsurface excess-ice. Furthermore, the model is supposed to be sensitive to climate variability and climate impacts like strong and rapid warming or cooling. Therefore, the model will be tested under different climates. If sensitivity to climate and today's lake distribution are reached for the Arctic permafrost regions, then the processes may be satisfactorily described and modelled.

1.2 Research questions

Emerging from the main focus of this PhD thesis, there are three research questions, which will be investigated.

1. Thermokarst lakes and soil excess-ice have successfully been modelled on local scale. Which parameterisations are needed to model these processes on global ESM grid scale? What is the sensitivity of the model to changes in these parameterizations?
2. What is the response of the thermokarst formulation introduced here to potential climate changes like cooling or warming of several degrees within one century? What is the timescale for adapting to a new equilibrium state?
3. How has thermokarst potentially developed during the Holocene? How has the rate of thermokarst formation changed over time? What is the sensitivity of the model to driving data from different sources?

After the thermokarst model is successfully developed and initialized, it may be possible to include thermokarst processes into JSBACH or another ESM. This would allow future projections of thermokarst development in the Arctic.

1.3 Structure of the PhD thesis

This PhD thesis is built up in 7 chapters including two chapters for introduction and conclusion. A short overview of the content can be found in chapters 2 - 6. The 1st research question is answered in chapters 3 and 4. The 2nd research question can be found in chapter 5. Chapter 6 deals with the 3rd research question.

Chapter-2 focuses on the Arctic climate and different permafrost related processes, which lead to thermokarst. It is a basic summary of findings in literature. The main issue is to give a comprehensive introduction into the topic of the thesis. First the periglacial Arctic climate is described, then distribution and properties of permafrost soils, then distribution and development of thermokarst lakes, and finally aggregation of excess-ice and formation of different complexes of massive ice.

Chapter-3 focuses on the development of a dynamic thermokarst module that spans over all stages of the thermokarst process. An adequate model is set up for modelling thermokarst on large scale. On the one hand, it should be able to consider small scale soil heterogeneities like slope distribution and permafrost fraction. On the other hand, it should include all steps of the thermokarst process.

Chapter-4 focuses on the sensitivity of the thermokarst model to different tuning parameters. A set of 25 parameters is initially performed for different soil and climate related processes (see Table 4.1). The thermokarst model is evaluated against satellite based observations of lake distribution derived from the ESACCI (Santoro et al., submitted) and observations of excess-ice

distribution from NSIDC (Brown et al., 1998).

Chapter-5 focuses on the response of the thermokarst model to climate change. Different scenarios have been adjusted to the CLIMBA Holocene runs (Bruecher et al., 2014). The scenarios describe warming of 2 °C, warming of 4 °C, and cooling of 2 °C, respectively, within a period of 100 years between 5000 BP and 4900 BP. The aim is to investigate effects of climate change on formation and evolution of thermokarst lakes and excess-ice.

Chapter-6 focuses on the potential evolution of thermokarst during the last 6000 years of the Holocene. Two different Holocene runs are available in the archive from Fischer and Jungclaus (2010) and Bruecher et al. (2014). Differences in chronological evolution of TKL are investigated. Then, differences within modelled distribution of lakes and excess ice at pre-industrial times are discussed.

1.4 State of the Art

Thermokarst is a small scale process, which needs to be added to the large scale global climate model. The evolution of lakes is severely dependent on surface and soil properties. Thermokarst lakes (TKL) span a large range of sizes and shapes. One thermokarst lake can measure between 1 m² and several 100 ha depending on annual expansion rates and on surface topography. The shape of the lakes can be squares like in the polygonal tundra or circles or ellipsoids. Even triangle shaped lakes can be seen in Eastern Siberia on satellite imagery.

The development of single lakes could successfully be modelled in 1D and 2D numerical models. They describe TKL with fundamental mechanical and thermal processes (Ling and Zhang, 2003; Zhou and Huang, 2004; Pelletier, 2005; West and Plug, 2008; Plug and West, 2009; Taylor et al., 2008). Van Huissteden developed a 2-dimensional landscape model to consider interactions between lakes and rivers (Huissteden et al., 2011). If one TKL connects to a river network because of lateral expansion it drains completely or at least a part of it. The water table changes due to lateral inflow and outflow, which in turn alters the ground thermal regime beneath the lakes. A 3-dimensional numerical model of a TKL and a neighbouring basin of a drained lake was presented by Kessler et al. (2012). Topographic interactions were included to simulate water flow into the lake as well as subsurface mass movement and slope wash at the lake edges. West and Plug (2008) have developed a numerical model of conductive heat transfer, phase change, and soil subsidence. Shape and depth of thermokarst lakes depend on lake age, steady state property of the talik, and the ice-content of the underlying ground.

All mentioned references have one point in common. They only simulate single lakes at local scale. Actually, there is no thermokarst model available at the global scale. One challenge can be that there are thousands of lakes and modelling each lake would require too many resources. However, the development of one lake is very dependent on small scale features like slope distribution, connection to drainage paths, and subterranean distribution of massive ice bodies. With increasing size of the lake the influence on the ground thermal regime can change dramatically if lakes do not freeze up to the bottom during winter. In that case talik grows also

during winter and the lake expansion rate increases. Parameterizations need to be found for simulating the average lake evolution. Another challenge is that the distribution of thermokarst lakes is not well known on Arctic scale. There are satellite based observations, but it is hard to judge the type and origin of the water bodies. They can also be ancient glacier lakes or simply filled topographic depressions. From the satellite's point of view all water bodies appear as dark areas surrounded by brighter permafrost (Muster et al., 2012; Morgenstern et al., 2011). Therefore, it may be tricky to evaluate global thermokarst models.

2 Thermokarst distribution in periglacial Arctic environments

This thesis is focused on thermokarst, which is typical for the periglacial Arctic regions. Thermokarst is defined as a process, by which characteristic landforms develop as a result of thawing of ice-rich permafrost and melting of massive ice bodies (Van Everdingen, 1998). These landscapes usually consist of little ponds, large lakes, and drained basins. The thermokarst process is a coupled thermal-hydrological mechanism, which leads to enhanced thawing of permafrost soils and depletion of soil organic carbon on local to regional scales.

This chapter consists of 4 parts and is supposed to give an overview of climate and soil conditions including processes, which lead to thermokarst. It is a basic summary of findings in literature. First, the periglacial Arctic climate is described. Which climate conditions are responsible for thermokarst affected landscapes? How does the region of periglacial Arctic climate differ from regions of other climates? The second part is considered to the main phenomenon of periglacial Arctic regions, the permafrost. How is permafrost distributed around the globe and what are the main properties of areas underlain with permafrost? Permafrost is the main precondition for thermokarst, which is explained in the third part. Thermokarst is unevenly distributed around the Arctic. Where does thermokarst occur and which mechanisms trigger formation of thermokarst lakes? An overview of the entire process is provided from the onset of little ponds until drainage of large lakes. Thermokarst primary develops in regions with ice-rich permafrost soils. The fourth part is focused on the aggregation of excess-ice within the soil. Ice accumulates to different forms of massive ice bodies, which appear in form of polygons and hills at the surface.

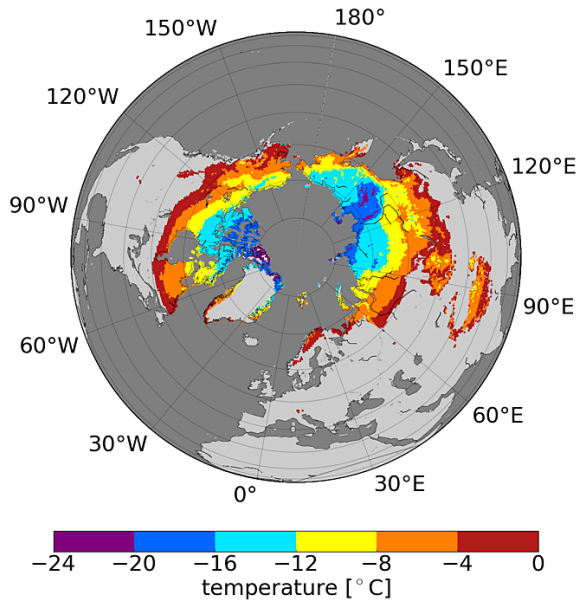
2.1 Periglacial Arctic climate

This section is focused on the periglacial Arctic climate. The term 'periglacial' relates to the area adjacent to a glacier or an ice sheet. The periglacial Arctic is characterized by repeated periods of seasonal freezing and thawing. Distinctions exist between glacial, periglacial, and Arctic conditions, which are based on different climates and soil forming mechanisms.

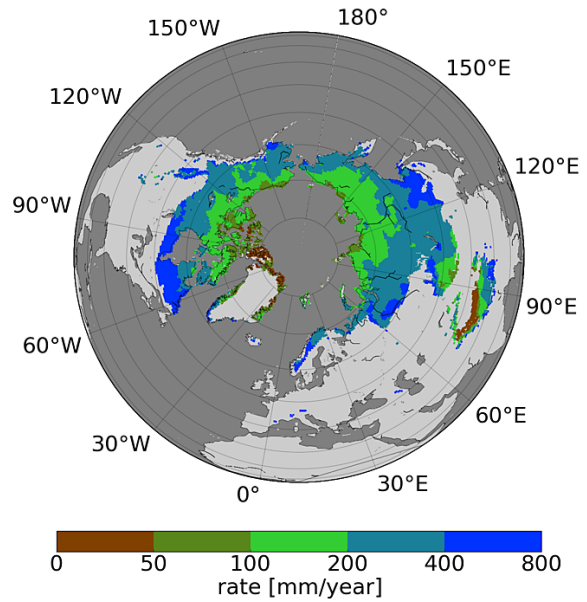
In glacial environments, the soil is prevented from melting and freezing processes, because glaciers isolate them from atmospheric influences. Due to their high albedo, glaciers absorb less radiation. The air temperature becomes cooler during the day and less energy is transferred to underlying soil layers than in non-glaciated regions. Furthermore during night-time the air becomes colder than in non-glaciated regions due to the lower heat capacity of snow in

comparison to soil.

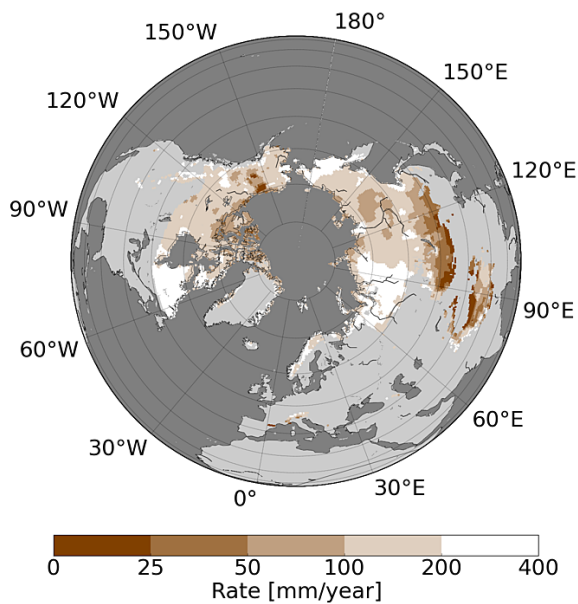
Long term mean annual air temperature



Long term mean annual rainfall



Long term mean annual snowfall



Long term mean short wave radiation

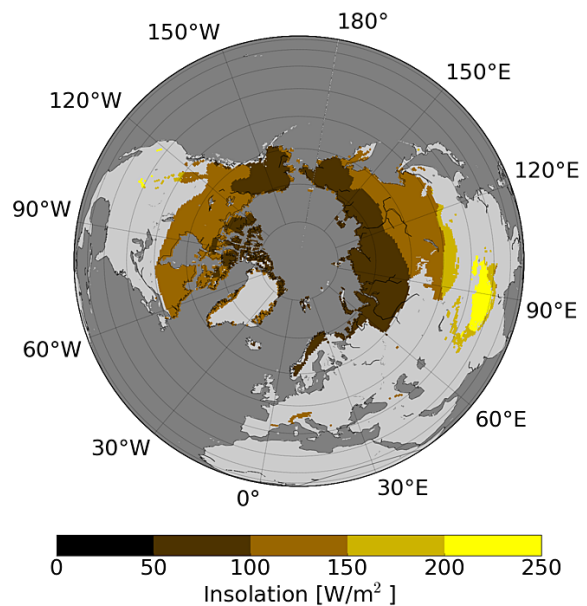


Figure 2.1: This figure shows long term means of annual air temperature (upper left panel), annual rainfall (upper right panel), annual snowfall (lower left panel), and incoming short-wave radiation (lower right panel) as derived from WATCH forcing data (Weedon et al., 2011) for the 43-year period 1958 - 2000. The maps were all masked with the overall extension of permafrost areas (Brown et al., 1998)

Contrary to glacial environments, the periglacial environments are characterized by freezing

and melting processes, since the air temperature is often around the freezing point of water. A permanently frozen ground layer (permafrost) develops within the soil, if the freezing depth exceeds the thawing depth (Tricart, 1968). Melting water from snow flows off at the surface or freezes again after infiltrating into the soil. The formation of ice bodies leads to so-called non-glacial geomorphologic processes and to formation of massive ice bodies in the interior of the soil.

Periglacial environments mainly cover tundra regions north of the treeline (French, 2007; Brown et al., 1998). This definition does not mean that periglacial processes are limited there. They also extend southwards into the Boreal taiga. During the last ice age permafrost has developed far into the south and often remained after the return of Boreal woods due to the large depths of the permafrost layer and the isolation effect of woody vegetation on the surface.

The largest parts of the global periglacial environment exist in Russia, Canada, and Alaska. Periglacial processes also occur on smaller areas in Greenland, Iceland, Scandinavia, Andes, and Tibet. In the Antarctica, only small parts are counted as periglacial and permafrost covered, because the most part of the continent is covered with large glaciers.

The climate of the periglacial Arctic is characterized by very long and cold winters and rather short summers. Figure 2.1 shows long term means of air temperature, rainfall, snowfall, and radiation. All the data are derived from WATCH forcing data of the 20th century for the 43-year period 1958 - 2000 (Weedon et al., 2011).

The long term mean annual air temperature varies between 0 °C at the southern edges and -24 °C in Eastern central Siberia or the northern Canadian Archipelago (see Fig. 2.1). The coldest regions are placed in Central Siberia, Yakutia, Northern parts of Alaska, North Western Territories, and Nunavut, where the annual mean temperature is mostly below -10 °C.

The annual total amount of precipitation is very low there and rarely reaches more than 200 mm. The periglacial Arctic generally receives little amount of rainfall. Values of more than 400 mm are only reached in Quebec, the southern Hudson Bay lowlands, Scandinavia, and at the SW and the SE edge of the Russian permafrost area (see Fig. 2.1). The driest regions with less than 100 mm are located in Tibet, the Canadian Archipelago, and at some coastlines of the Arctic ocean (Beaufort Sea, Laptev Sea, East Siberian Sea).

Snowfall is possible all the year round and usually accumulates to a closed snow layer during winter, which persists over several months. Coinciding with rainfall, little amount of snow is falling in Yakutia and Nunavut. Even less snow, with not more than 0.5 m, falls in large parts of Tibet and in southern Siberia. The highest amount of snow is observed in regions close to the oceans. More than 2 m are yearly accumulating in mountainous regions like the Rocky mountains, the Scandinavian mountains, and at the south western edge of the Himalayas. Also Northern Quebec, the far east of Siberia, and the western Siberian lowlands, receive more than 2 m of snow.

French (2007) defined five broad categories of periglacial climates based on insulation, temperature, and elevation with the goal to incorporate unique climate conditions of high plateaus, mountain, and flatlands. Generally, insulation reaches extreme states in both summer and winter. Due to the seasonal cycle of the day-length, for example the North Pole receives a higher amount of radiant energy than the Equator during summer. High elevated plateaus like Tibet receive more solar radiation than adjacent regions on sea-level, because water vapour and aerosol content of the atmosphere decreases with increasing elevation. This causes higher

transparency of the atmosphere. Here follows a summary of the five main categories of periglacial climate as classified by French (2007).

- I **High Arctic Climates** appear in polar latitudes and occupy the tundra regions. They are characterized by small daily but large annual temperature range. This is due to the perpetual darkness during the winter months, when temperature falls to a range of between -30°C and -20°C . Temperature rises above freezing only for 2 to 3 months, and reaches 4°C - 6°C on average. Therefore, the maximum thaw depth varies between 0.3 m and 1.5 m. The annual precipitation is very low and barely reaches more than 100 mm. Characteristic places with high-Arctic climate can be found in Spitsbergen (78°N) and in the Canadian Arctic (72°N).
- II **Continental Climates** appear in sub-Arctic latitudes south of the treeline within the Boreal woods. The mean air temperature is slightly higher than in the High Arctic, but the amplitude of the annual cycle is much larger due to excessively cold winters and very warm summers. The temperature rises above zero for about 5 - 6 months. Therefore, the maximum thaw depth is with 2 - 3 m larger than in the high Arctic. Typically 200 - 600 mm rainfall is measured throughout the year, while the most of it is falling during summer. Due to the high evaporation the water balance of the soil is negative. Continental climate is attributed to places like Yakutsk, Central Siberia (62°N) and Fairbanks, Alaska (65°N).
- III **Alpine Climates** appear in mid-latitudinal mountain environments above the timberline. Depending on the geographic location, the timberline ranges between 2000 m and 4000 m in the North American Rockies and in the European Alps. There, the climate is characterized by well developed diurnal and seasonal patterns of precipitation and temperature. Therefore, temperature oscillates around the freezing point with a higher frequency than in tundra and taiga regions. Winters are not as extreme as in the High Arctic. The total annual precipitation is with 750 - 1000 mm much larger than in the High Arctic. A typical place with alpine climate is Colorado Front Range, USA (40°N).
- IV **Qinghai-Xizang (Tibet) plateau climates** appear in high elevated low-latitudinal mountain regions. They are characterized by well developed diurnal and seasonal patterns of radiation and temperature, but with above-normal insulation. The annual mean temperature ranges between -2°C and -6°C . Although the annual precipitation measures between 200 mm and 600 mm, the water balance of the surface is more negative than in continental environments. Due to the extremely high evaporation rate during summer, the surface is covered by steppe-tundra vegetation. A typical place is Fenghuo Shan (34°N).
- V **Climate of very low annual temperature range** appear in sub-Arctic oceanic locations like Jan Mayen and Bear Island and in sub-Antarctic oceanic locations like the Falkland Islands and South Georgia. The annual mean temperature is settled below 3°C , while the annual cycle is relatively small with 10°C . These regions are characterized by high frequency of short freeze-thaw cycles. Due to the high precipitation of 1000 - 2000 mm/year

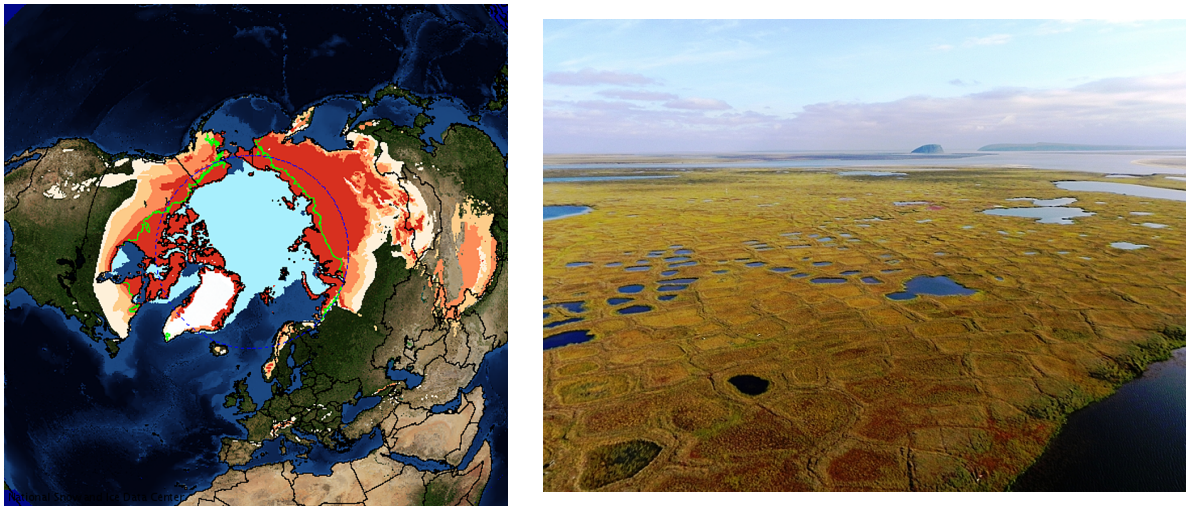


Figure 2.2: The left panel pictures the horizontal map of permafrost presence. The nuances of red show the permafrost extension from continuous permafrost (dark) to isolated permafrost (light). The green circle is the tree line, and the purple line the Arctic circle. The light blue area is the sea ice extension in July (Brown et al., 1998). Right panel shows a typical tundra landscape with continuous permafrost located in Samoylov, (Lena River Delta, Russia) (AWI, Research Group Sparc, 2010)

the weather is of unstable cyclonic type with much low cloud cover and fog. Similar climates occur in summits of low latitudinal mountain ranges like in Mauna Kau, where the diurnal cycle is larger than the weak annual cycle.

2.2 Distribution of permafrost soils

Approximately 23 - 25 % of the land areas of the northern hemisphere are underlain with permafrost (Brown et al., 1997; Zhang et al., 1999). These numbers would be even larger, if areas below glaciers and ice-sheets were counted as well. The largest part of it, about 72 %, is located in mountains, uplands and plateaus (Brown et al., 1997).

If a permanently frozen layer remains in the interior of the soil for at least two years in a row, then it is called permafrost. It is located below the active layer, which is the zone of annual freezing and thawing cycle. The maximum thawing depth or active layer depth (ALD) marks the transition from the seasonally to the permanently frozen soil (permafrost table). Depending on climate and surface conditions, ALD changes over time. If for example a thermokarst lake develops at the top, then the freezing depth decreases while the thawing depth increases (further explanations are given in section 2.3). Then a permanently thawed layer evolves between the active layer and the permafrost table, called talik. As visible in figure 2.3, there are several forms of talik. A smaller lake produces an open talik below it, while a larger lake develops a trough talik, which completely thaws the permafrost below it.

One property of a permafrost area is the fraction of surface underlain with permafrost. It is called permafrost fraction (PF) and has the unit m^2/m^2 . The permafrost regions are intersected

in four classes of PF (Brown et al., 1998), as listed in table 2.1. Figure 2.2 shows the four classes of PF as different nuances of red ranging from dark-red for continuous permafrost to light-red for isolated permafrost. In continuous permafrost regions, permafrost is present at all localities except beneath water bodies and river channels. Whereas in regions with sporadic permafrost, permafrost is restricted to isolated “islands” that are often located beneath peaty organic sediments.

Permafrost label	Permafrost fraction
Continuous permafrost	90 % - 100 %
Discontinuous permafrost	50 % - 90 %
Sporadic permafrost	10 % - 50 %
Isolated permafrost	00 % - 10 %

Table 2.1: Following permafrost fractions were provided by NSIDC (Brown et al., 1998).

Existence and absence of permafrost depends on the geographic location (latitude and altitude) and the climate conditions there. In this sense, the permafrost regions can be divided in three categories as classified by French (2007).

Latitudinal permafrost: About 50 % of Canada, 80 % of Alaska, almost 50 % of Russia (forest zone east of the Yenisei river), and parts of China (Tibetan Plateau and northeaster China) are underlain with permafrost (French, 2007). In north America, the southern border of continuous permafrost follows the -8°C to -6°C mean annual temperature isotherm except east of the Hudson Bay. The geographic extension of continuous permafrost decreases from 55°N in western areas to 60°N in Quebec. This is due to the high snow accumulation rates and the isolation effect of snow. The southern line of discontinuous permafrost coincides more or less with the -1.1°C isotherm (Péwé and Brown, 1973). Southwards, permafrost becomes restricted to peat lands, north-facing slopes, and shady river-banks. Usually the thickness of continuous permafrost ranges between 15 m and 30 m, but it sometimes reaches depths of 500 m. In general, permafrost is thicker in Russia than in North America. The largest permafrost thickness is observed in northern Yakutia, where it reaches a depth of 1600 m. Discontinuous permafrost is distributed in northern Scandinavia, the Kola Peninsula, and in the tundra and between regions between White Sea and Ural mountains. East of the Ural mountains, a broad zone of discontinuous permafrost extends over the taiga and reaches a depth of about 25 – 30 m. The northern boundary of the boreal forests (treeline) marks the transition line between continuous and discontinuous permafrost.

The differences of the permafrost properties in Siberia and in North America result from the Quaternary glacial history. In Siberia the lowlands remained ice free (aridity, vastness), while north America was covered by glaciers with several 1000 m thickness over large parts of the Pleistocene. Formation of extensive post-glacial lakes and marine inundation has accompanied glacier retreat in North America (French, 2007).

Alpine permafrost: In mountainous environments, permafrost properties are highly dependent on latitude, altitude, and distance from the nearest ocean. The regions are characterized by steep slope and bedrock terrain. Continuous permafrost is settled below the snow limit and crosses over to discontinuous permafrost at lower altitudes. The lower limit rises from 100 m at 60°N in North America to over 3000 m at 35°N in the Alps. The alpine permafrost is very

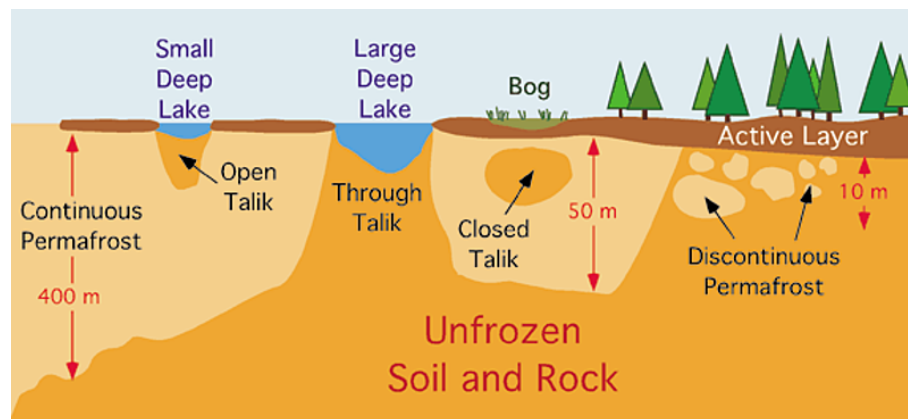


Figure 2.3: This figure shows the vertical cross section of the transition zone between continuous and discontinuous permafrost as well as different types of taliks connected to various stages of thermokarst lake formation (Pidwirny, 2006)

heterogeneous, while heterogeneity results from regionally very different pattern of temperature and precipitation. For instance, in some humid maritime valleys, glaciers extend far into forested areas, while in dry continental areas (central Asia) the glacier equilibrium line is located far above timberline. The lower limit of alpine permafrost in the Rocky Mountains and the Alps is marked by a mean annual air temperature of between 0 °C and -1 °C (Péwé, 1983).

Montane permafrost of central Asia and China: Montane permafrost forms on plateaus and in continental climates. It is a mixture of latitudinal and alpine permafrost and develops in China, Mongolia, and Kazakhstan. These mostly discontinuous permafrost regions are located in lower latitudinal high altitudes and are characterized by high aridity. Often, not more than 7 cm of snow are accumulating over one year. The Tibetan plateau is characterized by flat areas intersected by large mountain ranges. Depending on latitude, the Tibetan plateau permafrost reaches a thickness of 10–30 m .

The lower limit of Tibetan permafrost increases from 4000 m to 4800 m from north to south, indicating an increase of 110 m per degree north. Generally the lower limit of permafrost extension is marked by an average annual air temperature of -2.5 - -3.6 °C (French, 2007).

2.3 Thermokarst landscapes

This section is focused on distribution and evolution of thermokarst lakes (TKL). An overview is given about the formation of new lakes and the main steps of the life-cycle of one lake until drainage. Examples for some TKL are shown in figure 2.4

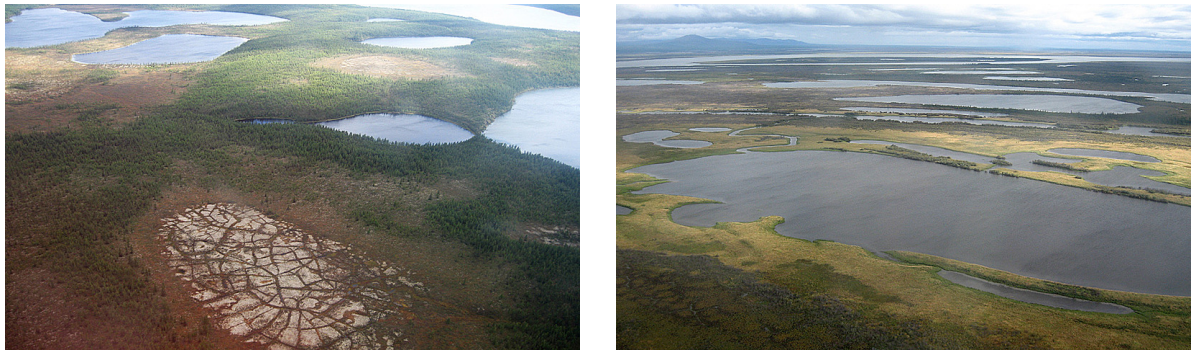


Figure 2.4: The figures show two areal pictures of several thermokarst lakes in the Kolyma-Region, Siberia. A drained thermokarst basin is visible in the left panel as well. (Grosse, 2014 in Kubny (2014)).

2.3.1 Distribution of thermokarst lakes

About one quarter of all global lakes larger than 10 ha are located in the northern mid and high latitudes between 45°N and 70°N (Lehner and Döll, 2004; Grosse et al., 2013). The majority of them are located in periglacial environments. As visible in figure 2.5, lakes in permafrost regions contribute strongly to lake covered surface area in latitudes north of 50°N. Isolated and sporadic permafrost regions strongly contribute to the lake area between 50°N and 60°N. North of 60°N, large areas of discontinuous and continuous permafrost regions are covered with lakes. Between 65°N and 70°N, the total lake area exceeds the observed area of lakes in mid- and low-latitudes even though much less land areas are present. There, the average lake fraction (65-70°N) in continuous permafrost region measures 19.6 %. The data are gained from satellite based observations from ENVISAT within the ESACCI project (Santoro et al., submitted).

Thermokarst lakes are widespread in periglacial Arctic regions and play an important role for the regional hydrology. The highest occurrence of TKL is observed in lowland permafrost regions with an ice-content of larger than 10 % in volume and with a thick overburden layer. Grosse et al. (2013) attributed following regions as being vulnerable to thermokarst: parts of the Northeast Siberian coastal lowlands, west Siberia north of the river Ob, Alaska north slope, Yukon-Kuskokwim delta region, Mackenzie delta region, Lena delta region, and the Hudson Bay lowlands.

A total number of 610000 lakes with an area of larger than 10 ha exist there. Together, they cover an area of 207000 km². Grosse et al. (2013) derived these numbers from analysis of pan-Arctic lake (Lehner and Döll, 2004) and permafrost databases (Brown et al., 1997). However, Grosse et al. (2013) stated, that a total lake covered area of about 250000 - 380000 km² is more realistic. The datasets on ground ice distribution, sediment type, overburden layer thickness, and lake extent are provided on a resolution of 0.5°. This leads to an underestimation of the total lake area. For instance, in northeaster Siberia, between 22 % and 82 % of the total TKL area is not captured by the global lake water dataset (Grosse et al., 2008).

The regional distribution of TKL is very heterogeneous and depends on various climatic, permafrost, and ground ice conditions. Generally, TKL develop better in regions with unconsolidated ice-rich sediments than in regions with bare bedrock (French, 2007). The small pore-size

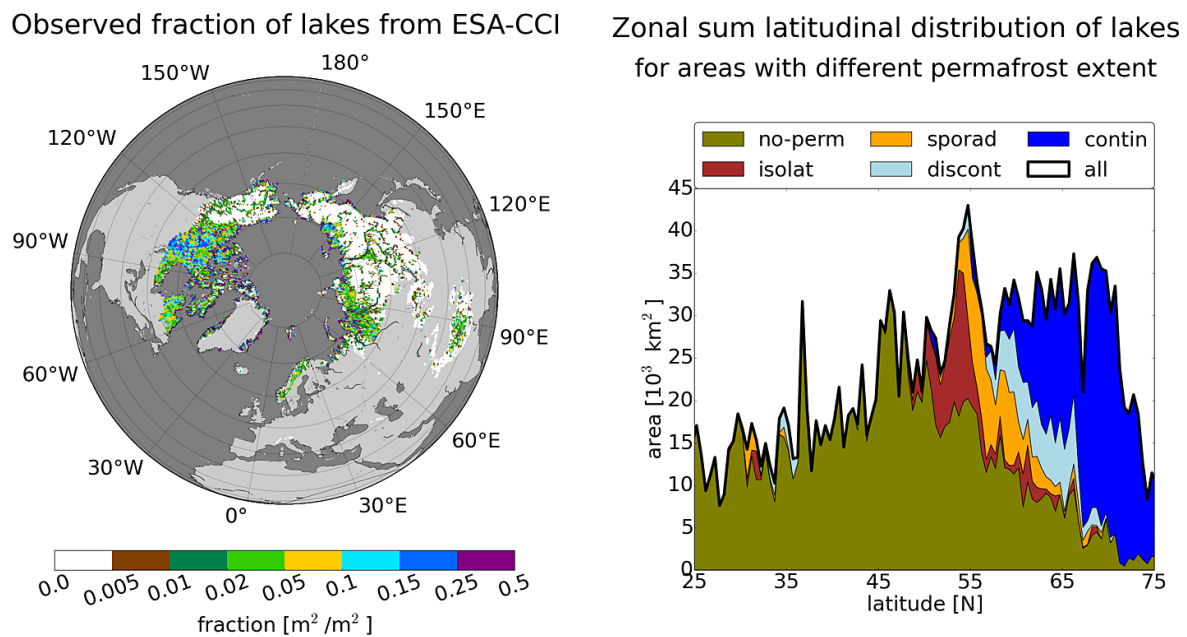


Figure 2.5: ENVISAT based observations of Arctic lakes larger than approximately 4.5 ha from the ESACCI project (Santoro et al., submitted). The data have been upscaled on 0.5° resolution and masked with the NSIDC permafrost extension (Brown et al., 1998) (left panel). The right panel shows the latitudinal distribution of zonal summed lake area.

of fine grained sediments promotes ice segregation and development of massive ice bodies. Thermokarst is rarely reported from mountainous regions and is largely absent in the ice-free extreme high latitudes. This is due to the high aridity there, which only allows low amount of segregated ice within the soil sediments. Thermokarst is most likely in areas with warm permafrost, which show a near-surface ground temperature of close to 0°C (French, 2007). There, vegetation cover and organic layer are crucial for preservation of permafrost and a small change can trigger formation of new TKL. Cold permafrost regions have small ALD and a short thawing period. There, a larger thermal change is required to trigger TKL.

2.3.2 Mechanisms triggering thermokarst

This section mainly bases on French (2007) and is focused on the trigger mechanisms of thermokarst. One thermokarst event is triggered by an initial disruption of the thermal equilibrium of the soil. ALD increases and segregated ice is melted. Cavities are left in the interior and upper-laying soil subsides. Depressions form at the surface and fill up with melting water. The water bodies promote thawing during summer and impede freezing up during fall and winter. At the early stage, thermokarst is widespread and very common in poorly drained tundra lowlands. A disturbance of the thermal heat balance occurs, if the annual main soil temperature increases or if the amplitude of the summer temperature enhances, i.e. progressive increase of seasonality. Disturbances can be classified in three different types, depending on the mechanism, which is acting on the soil. Thus, a disturbance can either be of geomorphic, vegetation, or climatic origin.

All of them are leading to melt of excess-ice and to the formation of a new TKL.

- * **Geomorphic impacts:** In some cases, the active layer is actively removed due to vehicle movements, road cuts, or drainage changes, which cause thawing of lower levelled ice-rich permafrost layers. Slumping and standing water in context of flood events increase ALD due to isolation of lower levelled soil layers against freezing periods. Cavities are washed out in the interior, and overlying soil layers subside. Thermokarst can also be triggered by lateral migration of rivers towards steeper slope at the coast. River banks slump and large ice-wedges expose then.
- * **Vegetational impacts:** Often, new TKL are triggered after the destruction of the isolating vegetation layer at the surface. ALD increases due to reduced shadowing and loss of isolation against seasonal variability of temperature. Disruption of vegetation can be induced either by economic activities such as constructions, vehicle movements, and deforestations. Vegetation can also be destroyed by natural phenomena like plant succession and lightning induced forest-fires. Wildfires are characteristic for Boreal forest and commonly appear in the tundra.
- * **Climatological impacts:** The climate warming of the past 100 years is capable of increasing thermokarst activity during the past decades. Higher temperature increases ALD, which causes melt of excess-ice during summer. The effect of continuously increasing annual mean temperature on ALD can be quite different. On the one hand higher temperature leads to a higher cloud cover and to more precipitation. This may reduce heat transfer within the soil due to colder surface temperature. On the other hand, a higher winter temperature leads to larger snowfall during winter. Due to the isolation effect of snow the freezing depth reduces. Therefore, a larger thawing depth can be reached during summer and ALD increases.

Predictions of future thermokarst events will be accompanied by large uncertainty. Beside a gradual change of annual mean air temperature, also increasing seasonality may result in higher potential for onset of thermokarst events due to higher range of soil temperatures and summer thaw depths (French, 2007).

2.3.3 Thermokarst process

Thermokarst is a self-promoting coupled thermal-hydrological process, which leads to enhanced thawing of permafrost soils with ice-rich sediments and depletion of soil organic carbon on local to regional scales. Melting of massive ice bodies lead to formation of thermokarst landscape features like drained basins (also called alasses), large lakes, and ponds (also called mounds) (Van Everdingen, 1998). Examples of different stages of the thermokarst process can be seen in figures 2.2 and 2.4. Thermokarst is severely affecting the Arctic tundra and permanently alters the appearance of its surface. Principally, a characteristic thermokarst process consists of five major stages and is described after French (2007) and Morgenstern et al. (2011). A schematic sketch of the first four steps is shown in figure 2.6.

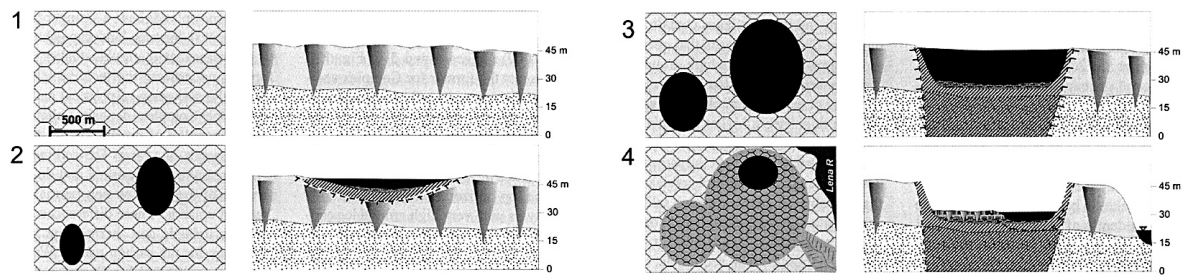


Figure 2.6: Stages of thermokarst process from undisturbed polygonal tundra to drained basins (alasses) with recovering permafrost (Morgenstern et al., 2011) after some adaptations.

In the beginning, there is flat undisturbed polygonal tundra with ice-rich unconsolidated sediments. Thermokarst is limited to localized ice-rich organic, maritime, and lacustrine deposits. The typical regions are characterized by High Arctic and Continental climate conditions (Sect. 2.1) with a thin active layer thickness of about 2 m. A trigger event is needed to disrupt the thermal equilibrium of the soil (Sect. 2.3.2). The annual thaw depth increases and causes enhanced melting of ground ice. Cavities are left in the interior and the above laying soil column subsides into depressions (mostly visible along large ice-wedge polygon systems). The depressions fill up with melting and precipitating water. Continued lateral and vertical expansion leads to slumping and disruption of the vegetation cover and to development of thermokarst mounds. These are distinct ponds with a width of 3-15 m and a depth of 3 - 4 m. Figure 2.2 shows an example of polygonal tundra, intersected with isolated ponds. The next stage is characterized by progressive collapse and decay of the ponds. If depressions develop in the centre of the thermokarst affected terrain, then they usually contain a large hollow with a lower levelled bottom than the adjacent ponds (French, 2007). Then, a distinct and large depression forms as a result of continuous merging of the central depression with smaller mounds in the surroundings. It is oval or circular shaped and consists of steep slides and a flat bottom. At this stage the water body is called a thermokarst lake (TKL). Examples are shown in figure 2.4. Permafrost thawing is continued due to progressive soil subsidence and slope wash at the margins resulting in lateral and vertical growth. At a certain depth, the TKL is not freezing up during winter, which promotes lake expansion and talik formation. The thermal erosion at the margins depends on ice-content and relief gradient (slope). While expansion is permanently ongoing, the vertical growth is limited as soon as a new soil surface heat balance and steady stage is reached. Figure 2.6 sketches a mature lake with a fully developed talik. The diameter can range between 100 m and 10 km.

Permafrost degradation and lake expansion stop as soon as the TKL disappears. This can be caused either by infilling of sediments from the walls or by connecting to a river network, a gully, or a neighbouring lower levelled basin (French, 2007). The remaining basin either forms a deep trough with steep slope and flat bottom or a depression with gentle slope and undulating floor. The depth of the basins can be up to 60 m in extreme case depending on the volume of melted excess-ice. After drainage, permafrost recovers and excess-ice accumulates again. The result is a basin with an area of up to 25 km², which consists of complex thermokarst valleys with different manifestations of excess-ice (Sect. 2.4). The aggregation of excess-ice continues until new thermokarst lakes are triggered. Generally, these lakes do not reach the same size and round shape as lakes of the first generation. Repeated cycles of permafrost degradation



Figure 2.7: Left panel shows a vertical cross section of one large ice wedge polygon system (AWI, Research Group Sparc, 2006). Right panel shows low-centred (foreground) and high-centred (background) ice-wedge polygons and one pingo (<http://sis.agr.gc.ca/cansis/images/nt/peri/index.html>).

and permafrost aggregation lead to a continuous change of the surface appearance of the Arctic landscape (French, 2007).

2.4 Ice rich sediments and massive ice wedges

Here, a short overview is given about different manifestations of excess-ice and the processes behind their formation. Excess-ice exists in various forms of massive ice-bodies, which appears as different surface structures. Pingos and palsas are hills with a lenticular-shaped ice-body in the interior. Polygons are hummocks intersected with rims and channels and contain a wedge-shaped ice-body in the interior.

Generally, ice occupies a larger volume than water due its lower density. Therefore, freezing of water leads to thermal expansion and to frost heave of upper soil layers. The magnitude of frost heave is mainly driven by available moisture within the soil. If one ice feature develops, then more water is attracted from the surroundings and freezes at the ice body. The volume of ice held within frozen sediment often exceeds the amount of water, which can be hold in thawed state.

The amount of excess-ice depends on various soil properties, which promote different mechanisms of ice formation. In fine grained soils with small pore-size and clayey texture, suction-based water movement dominates gravity. They mostly contain a high content of organic material and develop large bodies of excess-ice. In comparison to it, suction is small in coarse grained sediments like sandy and silty soils due to the large pore-size. In regions with coarse grained sediments infiltration leads to ice formation.

The highest amount of massive excess-ice bodies can be found in lowlands of northern and central Siberia. There, the terraces consist of thick sequences of fine-grained alluvial and very ice-rich sediments with ice constitution of up to 30 - 60 % in volume on local scale (French, 2007). However, in some other regions like higher elevated mountain ridges or high plateaus in

central Asia, ground ice is relatively absent.

2.4.1 Ice wedge polygons

Ice-wedge polygons are very common and widespread in tundra lowlands (central Alaska, northern Canada, and Siberia), which are underlain with continuous permafrost. Polygons primarily develop in sandy soils with unconsolidated sediments and usually contain excess-ice in form of large ice-wedges. One polygon can reach an area of between 15 m and 40 m. It is less pronounced in bedrock areas, where it may reach a diameter of 5 - 15 m. Polygons are mostly ordered in orthogonal patterns. Orthogonal systems develop in the vicinity of ponds and lakes, where cracks develop at right angles to the water body and to other cracks.

Ice-wedge polygons are frequent in regions with annual mean air temperature of less than -4°C (Washburn, 1980). The active layer depth is sufficiently thin to allow quick freeze up during fall and large temperature changes of the permafrost soils during winter (Black, 1976). If the surface temperature decreases fast enough with for instance -1.8°C/day over a period of 4 days, then thermal contraction of the soil leads to cracking due to large tension of the materials (Black, 1976). Amplitude and gradient of temperature change influence size and shape of the cracks. Other parameters like snow-cover and vegetation influence soil cracking as well. For instance, accumulated snow of large depth isolates the soil layers against the winter temperature regime. The cracks are filled up with snow and hoarfrost during winter. If temperature rises, then the snow cover melts and water infiltrates into these cracks and refreezes there again. Volumetric expansion of freezing water widens the crack to an ice wedge and pushes soil material sideways. Linear and volumetric expansion of freezing water is controlled by the mineral composition of the soil. The cycle of cracking of soil and freezing of infiltrating water is repeated over decades until the ice wedges reach a width of up to 5 - 6 m and a depth of up to 10 m (Black, 1976). The growth is limited by sideward pressure of expanding soil during summer and by uplift pressure of the overlaying active layer. Usually soil is pushed sideward from the centre of one polygon towards its margins. Between two ice wedges the soil material is raised up to a rim, which can reach a height of 0.5 - 1.0 m. In this way, ice-wedge polygons develop. An example is shown in figure 2.7.

2.4.2 Pingos and palsas

Pingos develop areas with coarse-grained water-saturated sediments, preferably after drainage of TKL. The highest concentration of so-called hydraulic pingos occurs in Tuktoyaktuk peninsula, northern Canada. They are also very frequent in northern Alaska and in central Siberia (French, 2007). Generally, pingos appear in regions with discontinuous and continuous permafrost regions with annual mean temperatures of less than -1°C (Washburn, 1980).

After drainage, the talik shrinks due to loss of isolating water at the surface. Usually, the talik of a drained basin consists of water saturated sands. Permafrost recovers and advances upwards from the permafrost table and sideward from the margins. Freezing of pore water causes water expulsion and frost heave of the lake bottom. Expulsion water moves towards the centre of the

drained basin, where it concentrates and freezes to a massive ice body in form of a thick lens. If cracks develop in the interior, water infiltrates the surface and freezes at surface of the ice body. If the hydrostatic uplift pressure equals or exceeds the overburden pressure of the upper lying soil layers, then the ice body heaves the soil above of it to a round or oval hill. A pingo can reach a basal diameter of 200 - 600 m and a height of up to 40 m (French, 2007).

Palsas mainly develop in wetlands with bogs and fens, which are underlain with fine-grained mineral soil. They appear in regions with sporadic or discontinuous permafrost, where the annual mean temperatures range between -1 °C and -8 °C (Washburn, 1980).

Palsas appear as hills, which contain a core of alternating segregated ice and mineral soil. These hills can reach a diameter of up to 100 m and a height of 1 - 7 m (French, 2007).

Palsa formation is usually initiated locally on places where less snow accumulates than around. For instance, less snow accumulates at the top of the hills during winter than in the lower-laying surroundings, because winds blow off snow from the hills. Also growing spruce trees on a sedge tussock in a bog and local wind turbulences can cause thinning of snow cover on some places. A thinner snow cover results in a larger frost penetration depth. Frost penetrates through the peaty layer at the top into the under-lying mineral soil. Water is attracted from the surrounding wetlands via cryosuction and freezes in the interior, which results in a further growth of the palsas (French, 2007).

3 Development of a dynamic thermokarst module

3.1 Set up of a thermokarst model

This chapter provides a description of the novel development of the first thermokarst model on global scale (TAPAS, Thermokarst Affecting Permafrost and Soil). A new method for generalizing the thermokarst mechanisms is discussed. The aim is to consider all stages of thermokarst from formation of new lakes over drainage of old lakes to aggregation of excess-ice in drained basins (see Sect. 2.3.3 for further details). Since the stages are driven by very different mechanisms, the whole thermokarst process can not be described with one formula. Therefore, the model is not a single process model. It is a combination of different observed processes.

Basically, this chapter is divided into four sections. Firstly, the set-up of the model is described. It consists of 42 age classes, while each of them contributes to one or more stages of the thermokarst process. The age classes contain lakes and basins of certain age. With every timestep, which is set to one year, the elements are shifted from one class to another one. Secondary, the distribution of thermokarst lakes (TKL) is severely limited by the topographic slope and the permafrost fraction (PF), which is defined as the fraction of surface underlain with permafrost. Therefore, TKL are very heterogeneously distributed over the Arctic (see Sect. 2.3.1). Thirdly, the processes are described in more detail. The processes which have been implemented in the TAPAS model, are as follows: formation of new lakes due to disturbances, growth of TKL with a size-dependent expansion rate, drainage of lakes as a function of time and PF, and aggregation of excess-ice in drained basins. Ice growth is a function of decaying ice deficit towards a maximum ice depth and is limited by slope and available liquid water. Fourthly, the model was initialized with an undisturbed permafrost surface. The distributions of excess-ice and slope are prescribed in the beginning. During the spin-up period, more and more parts of one grid cell are included into the model.

The TAPAS model is driven by data from the CLIMBA Holocene run from Bruecher et al. (2014) over a period of the past 7000 years. CLIMBA is a coupled climate-carbon model, which combines CLIMBER-2 with JSBACH (Bruecher et al., 2014). See section 6.2 for further descriptions.

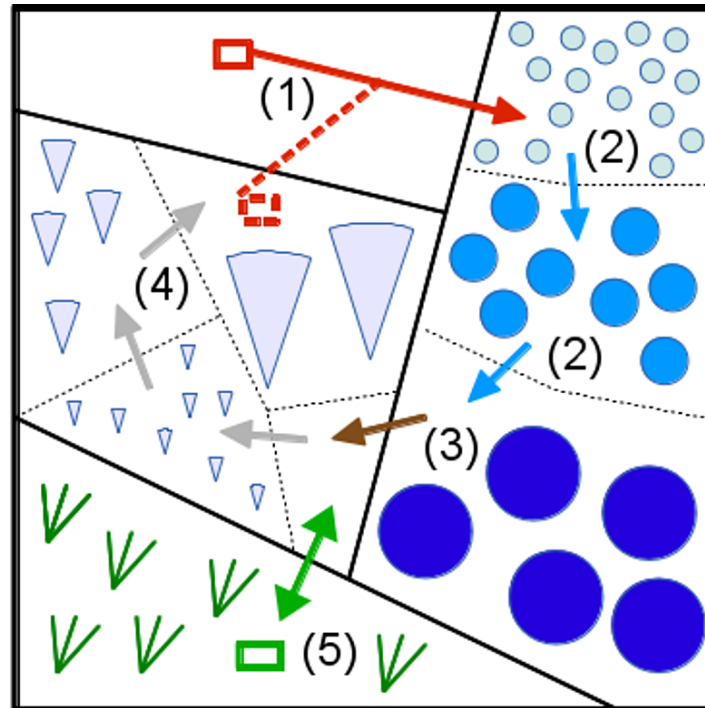


Figure 3.1: This figure shows a schematic sketch of the TAPAS model within one grid box. It includes thermokarst lakes (blue), excess-ice features in drained basins (blue-grey), and vegetation in permafrost free areas (green).

3.1.1 Stages of thermokarst development

The critical tasks for a global scale thermokarst model are to adequately represent all stages of the thermokarst process (Sect. 2.3), to regard sub-scale surface heterogeneities, and to build a simulation module for the entire Arctic without using too many computing resources. Several generalizations of the thermokarst process were needed to develop the TAPAS model. Generally the model consists of five parts, following figure 3.1

1. In the first part, the formation of new ponds is simulated. Thermokarst events are triggered by different disturbance events (1). The thermal equilibrium of the soil can be disrupted by different climatic, geomorphological, and vegetation impacts, which increase the active layer depth (maximum thaw depth during summer, ALD). The most important ones are for instance hot summers, floods, snow-rich winters, and wildfires. The number of new lakes is dependent on the magnitude of disruption (Sect. 3.3.1).
2. The second part considers lake expansion (2). New lakes are initialized as little ponds and expand to large lakes with a size of more than 500 ha. Due to progressive development, the size correlates to the age of the lakes (Sect. 3.1.2). Properties of the lakes, like expansion rate and drainage probability, are changing, since a permanently thawed layer (talik) develops below large lakes.

3. The third part considers drainage of lakes (3). Lakes leave drained basins with zero ice content after drainage. This part is also used for regarding changes in PF. Newly frozen regions (5) can be modelled like newly drained lakes, because excess-ice starts to develop there (Sect. 3.2.2 and 3.3.3).
4. The fourth part simulates aggregation of excess-ice in drained basins (4). The growth of massive ice wedges continues until new thermokarst is triggered. The growth is generalized with a logarithmic function and continues until a maximum ice depth is reached or thermokarst is triggered again (1). Development of different massive bodies of excess-ice like polygons and pingos are considered here (see Sect. 2.4 for closer descriptions).
5. The fifth part is the distinction between permafrost areas (1 - 4) and non-permafrost areas (5). This restricts the model on the frozen part of the grid cell. A typical grid cell consists of steeper hilly regions and of flatter plain parts. The distribution of the subgrid slope can be described as a b-function, following Stacke and Hagemann (2012) (for closer details see section 3.4.1). In steady state, the slope function is only used for the non-permafrost part. For the model, it is assumed that steeper sloped terrains are more likely frozen than flat terrain, because solar insulation decreases with angle of incidence.

3.1.2 Age classes and lake properties

In section 3.1.1, I described the basic structure of the TAPAS model which represents the major steps of the thermokarst process. The steps are split in categories or age classes, because they imply different physical mechanisms that can not be described with a single continuous function. As a matter of fact, the thermokarst process describes a wide range of lakes and basins, while the properties are highly dependent on the age and on thermal and hydrological states. The ages of a TKL span several millennia (West and Plug, 2008). Due to progressive expansion they reach a size of several km² (Grosse et al., 2008). One lake can drain at any time. Then, a basin is left where permafrost recovers again and excess-ice accumulates. Detailed models have been developed to describe the life-cycle of one TKL. Expansion and drainage depend on relief and soil constitution, while the lake depth is primary controlled by the ice content (Kessler et al., 2012). Sections 3.3.1 - 3.3.5 describe the mentioned mechanisms in detail.

All these mechanisms and limitations have to be considered for the development of a thermokarst model on the global scale. In fact not every single TKL can be modelled, but they can be clustered to different age classes. Lakes are expected to have similar characteristics, if they are at the same age or at the same stadium of the thermokarst process. The age is defined as the number of years after the lake has formed.

The age classes span over 2 domains (one for lakes and one for basins) with altogether 42 distinctions. The first domain consists of 33 classes and is attributed to lake development from initialization as little ponds until drainage. Altogether the TAPAS model spans a range of 7000 years. In principal, drainage can occur at any time. Jones et al. (2011) observed a drainage probability of larger than 0.0032. Therefore, lakes can hardly reach an age of 7000 years. New lakes start as circular ponds with an initial area of 1 m² (A_{ave}) in class 1. Different initial areas will be tested within the sensitivity studies in chapter 4. This initial area was chosen, because

Class	Years	Mean Age	dn_{in}	dn_{out}
1	<i>1</i>	<i>1</i>	0.000	1.000
2	<i>2</i>	<i>2</i>	1.000	1.000
3	<i>3</i>	<i>3</i>	1.000	1.000
..	1.000	1.000
9	<i>9</i>	<i>9</i>	1.000	1.000
10	<i>10 - 19</i>	<i>15</i>	1.000	0.100
11	<i>20 - 29</i>	<i>25</i>	0.100	0.100
..	0.100	0.100
18	<i>90 - 99</i>	<i>95</i>	0.100	0.100
19	<i>100 - 199</i>	<i>150</i>	0.100	0.010
20	<i>200 - 299</i>	<i>250</i>	0.010	0.010
..	0.010	0.010
27	<i>900 - 999</i>	<i>950</i>	0.010	0.010
28	<i>1000 - 1999</i>	<i>1500</i>	0.010	0.001
29	<i>2000 - 2999</i>	<i>2500</i>	0.001	0.001
..	0.001	0.001
33	<i>6000 - 6999</i>	<i>6500</i>	0.001	0.000
34	<i>0</i>	<i>0</i>	0.000	1.000
35	<i>1 - 200</i>	<i>100</i>	1.000	0.005
36	<i>201 - 400</i>	<i>300</i>	0.005	0.005
..	0.005	0.005
42	<i>1401 - 1600</i>	<i>1500</i>	0.005	0.000

Table 3.1: Overview of all age classes. From left to right, the table lists class, years represented by the class, average age, added fraction per year of previous class, and shifted fraction per year to the next class.

thermokarst can already start with ponds of this size (L. Kutzbach, 2014, pers. comm.). The number of years of each age class increases from 1 year (age class: 1 - 9), over 10 years (10 - 18) and 100 years (19 - 27) to 1000 years (28 - 33), see table 3.1. The second domain is attributed to accumulation of excess-ice in drained basins and consists of 9 age classes from class 34 to 42. It spans 1600 years, and ice wedges grow until the area is affected by thermokarst again. Drained lakes end up in age class 34 as empty basins. The number of years of the age classes is evenly set to 200 years, except for class 34 with 1 year. Age class 34 works as a transition from draining lakes to empty basins.

The stack sizes for the lake domain is set in different steps. For younger lakes, the stack size of the age classes is set to several years and decades, because of the large response of heat and mass transport to climate anomalies, Yi et al. (2014) have simulated the ground thermal regime of the talik below TKL under various climate conditions. For example, ponds are very small and expand relatively slowly (Jones et al., 2011). It is possible that they evaporate and disappear due to their small water volume. Considering the water balance of young TKL, precipitation contributes with 39 - 46 % to the total water input (Fedorov et al., 2014). In reality, the thermokarst process would be reversed until a new disturbance event occurs. Actually, early stage ponds are covering a very small fraction of the grid box. The magnitude of this fraction

ranges in an order of about $10^{-9} m^2/m^2$. Within the model, the thermokarst process of ponds younger than 10 years is stopped for one year after a year with very small surface runoff. Runoff is closely connected to precipitation. Ponds of up to an age class 9 remain within their age class. It is likely that the hollows, which have been formed by the ponds, will be filled with water again in one of the following years. Then, the thermokarst process continues. Therefore, the first 9 years are considered separately one by one.

The talik depth increases to a depth of more than 10 m within the first 200 years, as it will be described in section 3.3.2. All subterranean ice is depleted below the lakes. After that age, the lakes are only changing in area and volume due to lateral expansion and melt of segregated ice at the margins. Lakes with a depth of more than 2 m are more stable than shallower lakes and show a fully developed talik (Yi et al., 2014). Therefore, more lakes are added to one age class. The higher classes are introduced for maintaining the surface heterogeneity.

Depending on the magnitude of one disturbance event, a number of new lakes (n_{new}) is added to the first class. Every year, they are shifted from one age class to the following age class. They keep their attributed properties. This means, if the lakes were triggered on steep terrain with little amount of excess-ice, the soil properties attribute the lakes through all age classes until drainage. The technical realization will be explained here. The number of lakes within one age class at time t ($n_{lakes}(age, t)$) depends on the number of lakes at time $t - 1$ remaining within the age class ($lakes_{remain}$) and number of lakes of time $t - 1$ entering the age class ($lakes_{input}$) (see Eq. 3.1-3.3). Depending on stack size, a part of the lakes is leaving (dn_{out}) and a part is entering (dn_{in}) the age class, see table 3.1. Additionally, some lakes are draining (dn_{drain}). Drainage is dependent on the average age of the lakes, see section 3.3.4. The number of lakes within each class is firstly calculated for the highest age class and then stepwise for lower ones.

$$lakes_{input} = dn_{in} * n_{lakes}(age - 1, t - 1) \quad (3.1)$$

$$lakes_{remain} = 1 - dn_{out} - \min(dn_{drain}, 1 - dn_{out}) * n_{lakes}(age, t - 1) \quad (3.2)$$

$$n_{lakes}(age, t) = lakes_{input} + lakes_{remain} \quad (3.3)$$

$$slope_{ave}(age, t) = \frac{slope_{ave}(age - 1, t - 1) * lakes_{input} + slope_{ave}(age, t - 1) * lakes_{remain}}{lakes_{input} + lakes_{remain}} \quad (3.4)$$

$$ice_{cont}(age, t) = \frac{ice_{cont}(age - 1, t - 1) * lakes_{input} + ice_{cont}(age, t - 1) * lakes_{remain}}{lakes_{input} + lakes_{remain}} \quad (3.5)$$

$$(3.6)$$

Every age class has a specific slope ($slope_{ave}(age, t)$) and a specific ice content ($ice_{cont}(age, t)$), which can change with time because lakes with different soil properties may enter. Usually, one age class, where a specific slope and a specific ice-content is attributed to each of them. The parameters of each lake determine the average values of the age classes. Since lakes are shifted from one age class to the following one, the average at time t depends on lakes entering the age class ($lakes_{input}$) and lakes remaining in the age class ($lakes_{remain}$). The new average ice content ($ice_{cont}(age, t)$) is calculated as the weighted mean of the ice content of lakes entering the age class ($ice_{cont}(age - 1, t - 1)$) and the ice content of lakes remaining within the age class ($ice_{cont}(age, t - 1)$) (Eq. 3.5). The same scheme is applied for computing the new average slope ($slope_{ave}(age, t)$) (Eq. 3.4).

$$A_{land} = land_{fract} * A_{box} \quad (3.7)$$

$$dist_{fract}(age) = n_{lakes}(age) * A_{ave}(age) / A_{land} \quad (3.8)$$

Altogether, the lakes of one age class are covering a certain fraction of available land areas within one grid cell (A_{land}). The available land area is known from the area (A_{box}) and the land fraction ($land_{fract}$) of one grid cell (Eq. 3.7). Here, the lakes are used as a synonym for thermokarst affected area. But only in the ideal case of zero slope the water covered fraction ($lake_{fract}$) is the same as the thermokarst affected fraction, as it is described in section 3.2.1. This fraction is called disturbance fraction of one age class ($dist_{fract}(age)$). For the age classes 1 - 33, it describes the area thawed by thermokarst and for the other age classes, it shows the areas with a certain amount of excess-ice. It is calculated as the ratio between the total area covered by the age class and A_{land} (Eq. 3.8). The total area of one age class follows from the number of lakes within one age class and the average area of lakes within one age class ($A_{ave}(age)$), as it will be explained in section 3.3.3.

3.1.3 Overview of driving mechanisms and thresholds

In sections 3.1.1 and 3.1.2, I described the basic structure of the TAPAS model and the technical realization in form of age classes. Following the stages of the thermokarst process there are four main driving mechanisms in the model that regulate changes in lake fraction. These are formation of new lakes, lake expansion, lake drainage, and ice accumulation. The processes are constrained to certain boundary conditions. These conditions are usually of climatic origin, like temperature and precipitation. Moreover, soil properties are important for lake formation on thermokarst affected areas. Ice accumulation correlates with slope and is constrained to annual mean air temperature. This paragraph is thought to give a short overview of driving mechanisms and thresholds, which can be altered during sensitivity studies to optimize the model parametrization. Details can be found in the following sections 3.2 and 3.3.

1. **Number of new lakes:** Four different climate events are triggering the formation of new TKL in the TAPAS model. These are anomalies of winter snow water equivalent depth (SWE_{winter}), summer air temperature ($T2M_{summer}$), infiltration rate ($infil$), and burned area fraction ($burn$). Climate extremes are expected to trigger thermokarst due to disturbance of the ground thermal regime. For summer temperature, winter snow depth, and infiltration the anomaly from the long term mean is compared to the long term standard deviation. The number of new lakes triggered by wildfires ($burn$) is calculated as a linear function of the accumulated yearly burned area fraction.
2. **Expansion of lakes:** The expansion rate increases with time, because winds can transfer a higher amount of kinetic energy to larger lakes than to smaller ponds. Therefore, the erosion due to waves acting on the margins increases. A step function was assumed to be the best solution for parametrizing changes in expansion rate ($expand$). The reasons are shifts within the thermal and kinetic regimes of lakes after passing certain thresholds

(Morgenstern et al., 2011; Jones et al., 2011; Yi et al., 2014). Expansion is modelled for estimating the fractions affected by thermokarst and covered with thermokarst lakes.

3. **Drainage of lakes:** In continuous permafrost zones, drainage of thermokarst lakes can be triggered by expansion towards a lower levelled adjacent basin, connection to river and drainage networks, or coastal erosion (Hinkel et al., 2007; French, 2007; Grosse et al., 2011). The probability of drainage increases with time, as it was shown by Jones et al. (2011). Since permafrost stabilises water within depression, drainage is assumed to increase with decreasing PF. Actually no study has quantified the effect of decaying permafrost on drainage, but permafrost stabilizes the soils around a TKL. The derivation of the drainage probability function (*drain*) occurs in two steps. Firstly, a specific drainage probability is chosen for lakes with an age of 100 years and lakes with an age of 1000 years. Secondary, a dependency with PF is added, see section 3.3.4.
4. **Excess-ice growth:** Excess-ice appears in form of segregated ice and ice-wedges. Ice wedges grow with an order of millimetres per year until they reach a maximum depth of a few meters (Black, 1976), while segregated ice can grow to several tens of metres under optimum conditions within 1000 years (Konrad, 1990). Analogous to Kessler et al. (2012), the excess-ice (z_{ice}) is modelled as a decay of the ice deficit toward a specified maximum excess depth. The rate of increase is governed by the time-scale and the difference between the actual and maximum ice depth. Concluding from a threshold study between observed ice content and slope (Sect. 3.3.5), ice growth is severely limited by slope. It is also limited by drainage or the available amount of liquid water within the soil. Three thresholds have been introduced to separate warmer permafrost regions, where ice segregation is dominant, from colder permafrost regions, where ice wedges are dominant.

3.2 Limitations regarding the formation of water bodies

3.2.1 Effects of slope on lake formation

The slope severely limits the formation of TKL. Here, I want to introduce a limitation factor called area ratio (A_{ratio}), which accounts for the slope effect. It estimates the reduction of the water covered fraction or lake fraction ($lake_{fract}$) in comparison to the disturbance fraction (dis_{fract}). As described in section 2.3, mountainous regions consist of far less lakes than plain areas.

In principle, soil layers are orientated horizontally on flat terrain including active layer, ice wedges, permafrost table, and bedrock. The layered structure is also visible in regions with steeper hillsides. There, the layers are still orientated parallel to the surface. Actually, every grid cell fraction can be affected by a disturbance impact. Then, ALD increases and soil subsides due to melt of segregated ice. A depression is left, but depending on the gradient of the terrain, more or less parts of it are lying below the water outflow depth, where water can accumulate within the depression. This part of the melting water remains, while the other part flows off down-slope. An illustration is provided in figure 3.2. If an area is heated after a disturbance impact, the

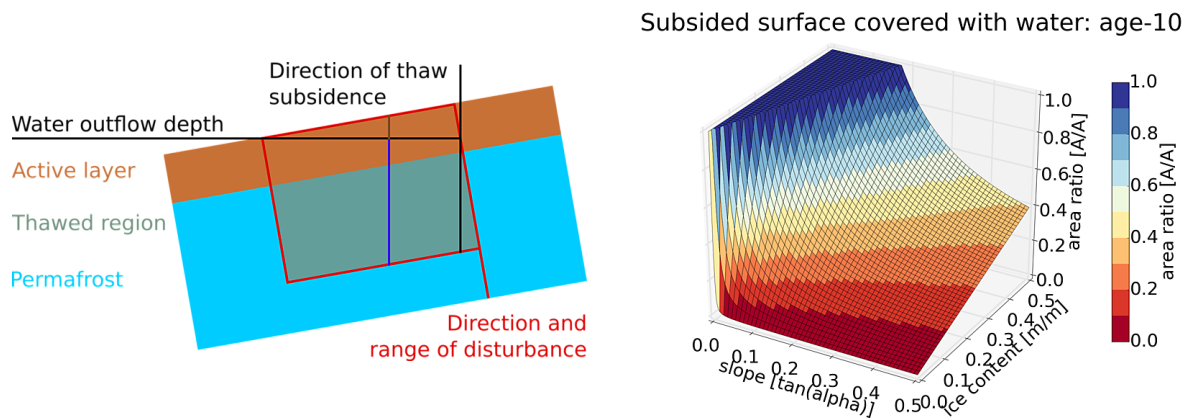


Figure 3.2: Left panel shows the structure of soil and the components for calculating the area of disturbed permafrost (35 m^2) covered with water. It includes active layer depth (ALD), permafrost, and talik. The results of computing the area ratio is shown on right panel for a sample of slopes and ice-contents.

closest frozen soil element will be thawed first. Therefore, ALD increases orthogonally to the surface, which is called direction of disturbance in figure 3.2. The melted ice depth can be considered to be independent of slope. It can be derived from the thawed permafrost height (h_{thaw}) and the ice content of the soil (ice_{cont}). To consider the limitation effect of slope, the melted ice is calculated along the direction of subsidence (Eq. 3.9), because the ratio between subsided soil and melted ice is important.

The depth of melting water (h_{melt}) is equal at any point below the affected area below one age class, which is considered as squares, because the initial area of new ponds and the expansion rates are very rough estimates. Furthermore, the thawed permafrost area is not more than a simple average of all lakes within one age class ($\rightarrow A_{ave}$).

In completely flat terrain, the total subsided area will be covered with water. The area ratio between disturbed area and the lake area is equal to one ($A_{ratio} = 1$). The water outflow depth can not be reached due to higher density of water in comparison to ice. How does slope influence the water filled area? The area ratio must decrease, because the water outflow depth falls below the surface of the evolving depression in steeper regions. As a matter of fact, melting water leaves cavities and soil subsides vertically along Earth's gravity (see figure 3.2). Therefore, the height of subsiding soil (h_{soil}) increases with the tangent of the gradient's angle (α_{slope}) (Eq. 3.10). At a certain point it is possible, that more soil is subsiding than cavities have formed. The resulting surface of the terrain is higher elevated than the water outflow depth and remains dry. Thus, melting water is flowing off as surface runoff. The depression is filled with water as long as the height of melted ice is larger than the height of subsided soil ($h_{melt} > h_{soil}$) (Eq. 3.9 and 3.10). The length of the disturbed area along the slope is known to be 2 times the average radius (r_{ave}) of the disturbed area (A_{ave}) since all lakes are defined as circular water bodies. The length in slope direction, at which the subsided soil equals the melted ice, is called the water length (l_{water}) (Eq. 3.11). It gives the largest possible extent of water. The area ratio is actually the ratio between the water length and the disturbance length along the slope (Eq. 3.12).

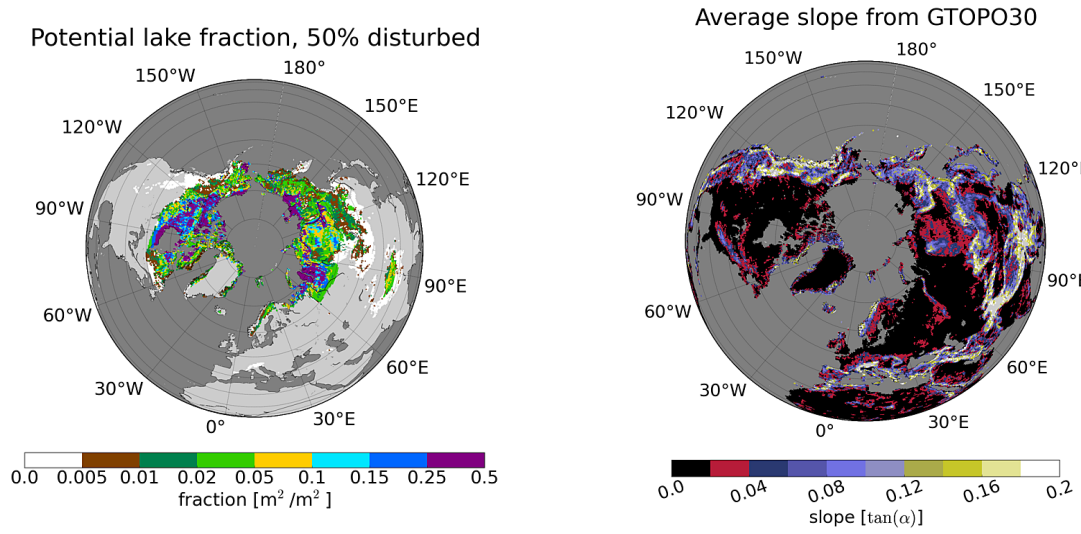


Figure 3.3: Left panel shows potential limnicity in the Arctic, if 50 % of the permafrost area is affected by thermokarst. All lakes are 500 years old. The soil conditions are average slope of grid cell (Stacke and Hagemann, 2012) (on right panel) and ice-content derived from NSIDC (Brown et al., 1998), as shown in figure 3.11.

$$h_{melt} = \frac{h_{talik} * ice_{cont}}{\cos(\alpha_{slope})} \quad (3.9)$$

$$h_{soil} = l_{water} * \tan(\alpha_{slope}) \quad (3.10)$$

$$l_{water} = \frac{h_{talik} * ice_{cont}}{\sin(\alpha_{slope})} \quad (3.11)$$

$$A_{ratio} = \min\left(1, \frac{l_{water}}{2 * r_{lakes}}\right) \quad (3.12)$$

The area ratio always has a value between zero and one. In figure 3.2, the sensitivity of the area ratio is evaluated against slope and ice content for new ponds with a disturbance length of 2 m. The slope ranges between zero and 0.5 m/m or 26°, while the ice content increases from zero to 80 %. As expected, the area ratio increased linearly with the ice content. The slope is assumed to be homogeneous for single lakes. Therefore, the subsided soil and the water length are increasing linearly with melted ice. The behaviour of the area ratio regarding the slope is much more sensitive due to the tangent function. It decreases fast for low ice contents and decreases slightly slower for high ice contents. The radius of the disturbed area is increasing with time. Larger parts of subsided area are located above the water outflow depth and, therefore, the area ratio decreases for older lakes. As a result, the best effect is visible for the first age class.

Obviously the lake fraction $lake_{fract}$ is highly sensitive to slope. Thus, the area ratio function provides a method to describe the limitation effect. The reliability of the limitation function was tested within a potential thermokarst study. Let us assume that one half of all permafrost areas is disturbed or affected by thermokarst. Which fraction of the grid cell would be filled with water at the end? After 500 years a new pond has developed to a lake with a radius of more than 100 m. The area exceeds 1 ha and talik extends to a depth far larger than 10 m. In this example all

lakes are of this age. The average radius measures 100 m ($r_{ave} = 100$) and the disturbance length 200 m. One half of the permafrost area is affected by thermokarst ($dist_{fract} = 0.5$). A simple talik thickness of 8 m ($talik_{depth} = 8$) is used to regard a former ALD of about 2 m. Following equations 3.13 and 3.14, the area ratio is calculated with the average slope ($slope_{mean}$) of the grid cell (Stacke and Hagemann, 2012) and a feasible ice content value based on data from NSIDC (Brown et al., 1998).

$$\alpha_{slope} = \arctan(slope_{mean}) \quad (3.13)$$

$$A_{ratio} = \min\left(1, \frac{8 * ice_{cont}}{2 * 100 * \sin(\alpha_{slope})}\right) \quad (3.14)$$

$$lake_{fract} = dist_{fract} * A_{ratio} \quad (3.15)$$

With disturbance fraction and the area ratio, it is possible to calculate the lake fraction (Eq. 3.15). In this study, 50 % of the permafrost area is affected by thermokarst. The fraction of grid cell covered by lakes is computed as $0.5 * lake_{fract} * perm_{fract}$. The permafrost fraction ($perm_{fract}$) ranges between zero and one and works as a second major limitation factor of formation of TKL. PF and ice content were both derived from NSIDC data and are shown in figures 3.4 and 3.11. The potential lake fraction or limnicity is shown in figure 3.3. Most lakes can develop in flat terrain of north-west Canada, North Slope of Alaska, Laptev Sea Coast, and western Siberia. The limnicity decreases southwards due to lower PF, as it is visible south of the Hudson Bay. Generally, low lake fraction values appear in mountainous regions with steep terrain. The slope data were masked with the permafrost distribution. Obviously at the southern border of the permafrost region, only very steep regions imply permafrost areas. There the steepness is closely linked to elevation.

3.2.2 Permafrost fraction and lake formation

Soils underlain with permafrost are a precondition for the development of TKL. Therefore, it is crucial to include PF into TAPAS model. Distribution and depth of permafrost vary strongly throughout the Arctic due to soil and surface heterogeneities. For instance, higher elevated terrains freeze earlier than lower plains due to lower annual mean air temperature and longer period with snow cover. In mountainous regions, southward orientated slopes are easier thawed than northward sided slopes. Snow is melting earlier on southward slope because of higher insulation, but this may balance with the northward part. Some other regions are covered by marshes, rivers, or lakes. There, water is influencing the ground thermal regime and limits freezing of soil.

A GCM grid box usually consists of a mixture of surface characteristics. Resulting from this, a larger or smaller part of it is underlain with permafrost. Four classes have been defined by NSIDC ranging from continuous to isolated permafrost, as it is listed in table 2.1 and shown in figure 3.4 (see section 2.2). Several models have been developed to simulate PF. Nelson and Outcalt (1987) retrieved and evaluated different methods.

The frost number (F), for instance, is a first estimation of the zonal distribution of permafrost continuity on continental scale (Nelson and Outcalt, 1983). Originally it is a function of degree days. Further improvements enabled inclusions of more parameters, like frost and thaw

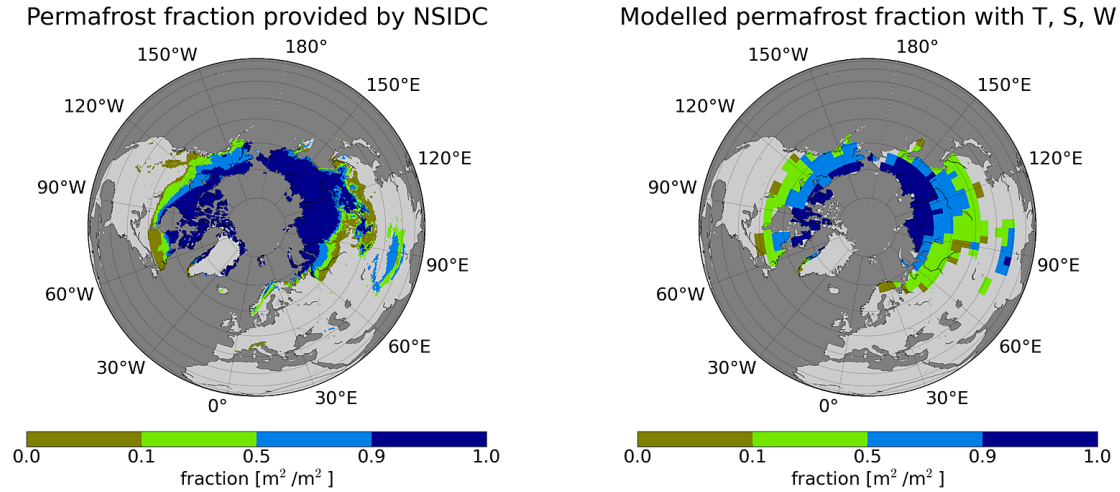


Figure 3.4: Comparison between permafrost fraction provided by NSIDC (left panel) (Brown et al., 1998) and derived as a function of air temperature, winter snow depth and wind speed or $T2M_{\text{mean}_{\text{snow}}}$ (right panel).

penetration depth. Based on the Stefan-equation, thawing depth (z_{thaw}) and freezing depth (z_{freeze}) are computed as a function of freezing-degree-day (FDD) and thawing-degree-day (TDD) (Nelson and Outcalt, 1987). Frost index is a relation between thawing depth and freezing depth, see Eq. 3.16.

$$F = \frac{z_{\text{freeze}}}{z_{\text{freeze}} + z_{\text{thaw}}} \quad (3.16)$$

Permafrost develops, if freezing depth equals or exceeds thawing depth. For instance, a frost number of 0.5 is reached, if $z_{\text{freeze}} = z_{\text{thaw}}$. This is the case, if FDD equals TDD . Then the annual mean air temperature ($T2M_{\text{mean}}$) is 0°C . Thus, PF is larger zero for $F \geq 0.5$ or for $T2M_{\text{mean}} \leq 0.0^\circ\text{C}$.

A frost index of 0.666 is reached, if z_{freeze} is twice the value of z_{thaw} . This is the case, if $FDD = 4 * TDD$. Following an example in Nelson and Outcalt (1987), the ratio between freezing and thawing degree days fits to an annual air temperature of -10°C . Regions poleward of locations with $F = 2/3$ are completely underlain with permafrost (Nelson and Outcalt, 1987). Thus PF is one for regions with $T2M_{\text{mean}} \leq -10.0^\circ\text{C}$. Equator-ward permafrost is discontinuous and decreases linearly with freezing index.

Following the conclusions above, PF can be directly expressed as a function of $T2M_{\text{mean}}$, like in equation 3.17. Thus, PF drops from 1.0 to 0.0 between an $T2M_{\text{mean}}$ of -10°C and 0°C .

$$PF = \max(0, \min(1, -1/10 * T2M_{\text{mean}})) \quad (3.17)$$

Freezing and thawing degree days are retrieved from daily mean temperatures. However, for the TAPAS model, only monthly mean driving data have been available from the Holocene runs. Therefore, it seems to be reasonable to retrieve PF from $T2M_{\text{mean}}$ which is computed with the monthly mean values. Figure 3.5 shows PF derived from $T2M_{\text{mean}}$ in comparison to the NSIDC data and to a second method, which is described in the following.

The second method includes the influence of snow depth and snow density on the annual cycle

of freezing and thawing depth. The snow parameters depend on wind and air temperature. To come closer to reality, the winter temperature was corrected via regarding heat conductivity and heat capacity of snow (Nelson and Outcalt, 1987). The damping depth of snow (z_{damp}) has been introduced for this issue. Equations 3.18-3.22 are showing the method. Nelson and Outcalt (1987) assumed a sine shaped progression of daily temperature throughout a year. Amplitude and average temperature are used to derive length of winter (l_{winter}) and summer (l_{summer}) season, respectively freezing and melting season. Nelson defined winter as the period, when the curve is located below 0 °C. The winter temperature is adjusted to the isolation effect of winter snow cover, since the sub-snow temperature is influencing the thermal properties of soil. First the average snow density (ρ_{snow}) is calculated with the average wind speed (u_{winter}) and with the average winter temperature (T_{winter}) (see Eq. 3.18).

$$\rho_{snow} = 152 - 0.31 * T2M_{winter} + 1.9 * u_{winter} \quad (3.18)$$

The damping depth (z_{damp}) is a function of thermal diffusivity (α_{snow}) (Eq. 3.21) and period length (π) of the annual cycle. The thermal diffusivity is the relation between the thermal conductivity (λ_{snow}) (Eq. 3.19) and the heat capacity (C_{snow}) (Eq. 3.20) of snow. The knowledge of thermal diffusivity and average winter snow water equivalent depth enables to estimate the effect of a snow layer of a certain average thickness on the average winter soil temperature ($T2M_{winter_{snow}}$), which is calculated according to Nelson and Outcalt (1987).

$$\lambda_{snow} = 2.1e - 2 + 4.2e - 4 * \rho_{snow} + 2.2e - 9 * \rho_{snow}^2 \quad (3.19)$$

$$C_{snow} = 7.79 * T2M_{winter} + 2115 \quad (3.20)$$

$$\alpha_{snow} = \frac{\lambda_{snow}}{C_{snow} * \rho_{snow}} \quad (3.21)$$

$$z_{damp} = \sqrt{\alpha_{snow} * 365 * 86400 / \pi} \quad (3.22)$$

Due to the damping effect of snow, $T2M_{winter_{snow}}$ differs from $T2M_{winter}$. Therefore, the annual mean temperature alters $T2M_{y_{mean_{snow}}}$ which is a weighted mean of summer temperature and the new winter temperature, see Eq. 3.23. The weights are given by the period lengths of the seasons. Finally, PF is computed with $T2M_{y_{mean_{snow}}}$.

$$T2M_{y_{mean_{snow}}} = \frac{T2M_{winter_{snow}} * l_{winter} + T2M_{summer} * l_{summer}}{l_{winter} + l_{summer}} \quad (3.23)$$

Here, both methods of computing PF are evaluated against NSIDC observations. The first method is $PF(T2M_{y_{mean}})$ and the second one $PF(T2M_{y_{mean_{snow}}})$. The zonal distribution of PF can be reached more or less satisfactory. Figure 3.5 illustrates a comparison between modelled PFs (green and blue bars) and observed PF from NSIDC (black bars). The observed absolute frequency of PF within a certain category is better reached by the green bars than by the blue bars. Thus PF accords better to reality if it is computed with $T2M_{y_{mean}}$. With both methods, permafrost is falsely visible in western Russia, northern Scandinavia, and coastal regions of eastern Asia. Generally, permafrost extends less far into the south if computed with the first method. Although the second method includes more physical properties than the first one,

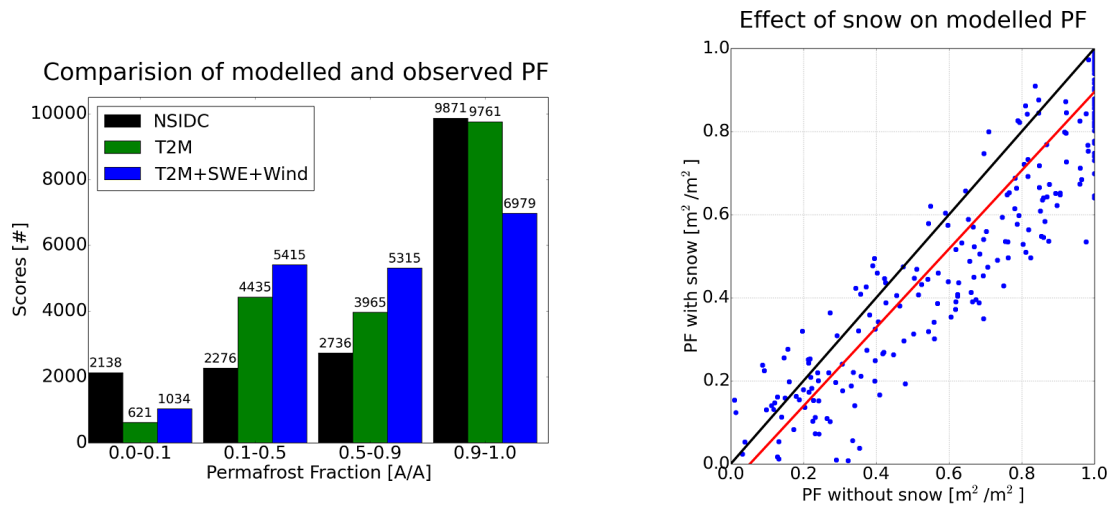


Figure 3.5: Left panel shows the number of grid cells classified with different PF classes for NSIDC at 0.5° resolution in comparison to two different approaches to derive PF. The right panel illustrates a comparison of PF derived with two different methods. One time simply $T2M_{mean}$ was used and the other time $T2M_{mean}$ was adjusted to the effects of snow and wind. The black line represents the one-to-one fit and the red line the mean regression line between both approaches.

differences between NSIDC and model are smaller for the first method. Large regions of central Siberia are not regarded as continuous permafrost from the second method. This explains the differences between green and blue bars in figure 3.5. Therefore, PF is computed with the first method within the TAPAS model.

The effect of snow is visible in the scatter plot in figure 3.5. As expected, it decreases PF by up to 45 % in cold regions. Snow isolates and damps cooling of soil layers during winter in cold regions. PF increases in some warm areas, which probably arises due a shift of the starting point of thawing of the soil. At the onset of the melting season, much energy needs to be invested for melting of snow. However, regarding the "snow-effect" does not improve the model results. In reality, PF is probably driven by other properties like details of the snow cover.

Changes within PF have to be regarded within the TAPAS model, because permafrost is changing over years and centuries. For future projections it will be very important, because a large decay in permafrost fraction is expected for the current and the following centuries. Also in the last 7000 years, there have been changes in air temperature and, therefore, also in permafrost fraction.

If PF increases, the new PF is added to the age class for drained basins, which is age class 34 in table 3.1. As it is the case for drained lakes, the ice content is zero and massive ice bodies start to develop. If PF decreases, ALD increases and permafrost thaws. Actually, lakes are kept within a permafrost layer like an enclosed hollow. Drainage occurs sideward within the thawed layer. In Boreal regions, lakes are settled several meters below the ground level (L. Kutzbach, 2014, pers. comm.). A lake will drain if permafrost disappears at its margins. Therefore, the drainage probability of TKL increases with decreasing PF. Usually, there is a fluctuation within

PF, wherefore PF changes faster than lakes are developing. In extreme cases, PF can decrease by up to 30 % within a few centuries.

Within the TAPAS model, the age class for drained lakes (class 34) is used to add new PF at one time and to subtract lost PF the other time. Sometimes, permafrost decreases much faster than lakes are draining. Then, drained basins of higher age classes are reduced as well. These basins already contain excess-ice, which melts because of thawing permafrost. The volume of melted water is added to the drainage.

For regions with very little permafrost fraction ($PF < 10\%$), there may not be enough space within the age classes for drained basins. Therefore, a lower threshold for permafrost fraction has been introduced into the TAPAS model. Thus, the model is applied to grid cells with PF of at least 10 %. Anyway, these regions are very warm and permafrost only exists in very isolated patches.

3.3 Formulation of the main thermokarst mechanisms

3.3.1 Disturbances and formation of new ponds

As described in section 3.1.1, thermokarst starts with the formation of new ponds. Among others new ponds also develop due to climate extremes, which disrupt the heat balance within the soil. Depending on the magnitude of the climate impact, more or less new ponds are forming. A disturbing event is defined as a process that abruptly increases the ALD, which leads to melting of segregated ice. The magnitude of a disturbance must be a function of the anomaly. The larger a climate extreme is, the more ponds develop.

Statistically, about two third of all events are falling within one standard deviation around the mean value. Events below 1σ are very common and do probably not alter the ground thermal regime too much. About 16.7 % of all events are above 1σ , about 2.5 % above 2σ , and less than 0.5 % are above 3σ . For instance, the summer temperature of one region is 5°C on average with standard deviation of 1°C . This means, that over a period of 1000 years, 5 summers are warmer than 8°C and 167 are warmer than 6°C . The impact is much higher for higher anomalies than for lower ones. I assume, that the number of triggered thermokarst events is increasing exponentially with the number of standard deviations above. 6°C are very common and are reached every 6 summers. Only single ponds are developing. In comparison, 8°C are relatively seldom and are reached every 200 years. This is enough time for accumulation of large ice masses, between two occurrences. Therefore, I assume, that a much higher number of new ponds develop if the summer temperature measures 8°C than if it is 6°C .

Generally, the connections between trigger mechanisms are known (Grosse et al., 2011). Grosse et al. (2011) have studied depletion of soil organic carbon in general and distinguished between press and pulse events. They mapped a network of connections and interrelations of climatic and geological mechanisms acting in the Arctic. Thermokarst is only one disturbance of many, which are acting on the soil organic carbon stock. It is counted to the pulse processes with more local than widespread occurrence and acts on timescales from seasons to decades. Primary, thermokarst is caused by wildfires, hydrological changes, vegetation changes, top-down thawing of permafrost, and erosion. For instance, the following interrelationships lead to thermokarst

formation.

- Erosion processes are enhanced by floods, which in turn arise due to hydrological changes.
- Erosion increases after changes in the hydrology, coastal and fluvial erosion and floods.
- Wildfires develop during droughts, which are connected to hydrological changes.
- Vegetation changes after changes in soil temperature or hydrology.
- Top-down thawing of permafrost increases due to warming of soils.
- Top-down thawing of permafrost also increases due to hydrological changes.
- Droughts lead to vegetation changes and to increased top-down thawing of permafrost.
- Vegetation changes can lead to wildfires, which in turn lead to enhanced top-down thawing of permafrost

As already mentioned, the number of new ponds probably increases with the strength of a disturbance impact. Actually, there are no studies available about frequency of thermokarst events after a certain climate impact. A relationship needed to be derived and tested. This thesis establishes a connection between the number of newly triggered TKL and the magnitude of a disturbance impact, which is applicable for large scale climate models. Different functions have been tested during the sensitivity studies (Chapter 4). A reasonable climate dependent development of the lake fraction is found.

Top-down thawing of permafrost is an important disturbance. Upper soil layers are frozen during winter and are thawed within the short summers between June and August. The final depth of the active layer depends on the average summer temperature ($stemp$). The importance of single heat waves is marginal. Important is the final thaw depth. Therefore, the number of temperature disturbances ($ndist_{stemp}$) is computed as a function of the anomaly from average summer temperature between June and August ($stemp - \mu_{stemp}$) and the standard deviation (σ_{stemp}) (Eq. 3.24).

$$ndist_{stemp} = \max \left(0, a_{stemp} * \frac{stemp - \mu_{stemp}}{\sigma_{stemp}} \right)_{stemp}^b \quad (3.24)$$

Coefficients a_{stemp} and b_{stemp} are factor and exponent of the relationship. They are initially set to $a_{stemp} = 1$ and $b_{stemp} = 3$ during the first tests. TAPAS is driven by forcing from the CLIMBA Holocene run. Figure 3.6 shows modelled the maximum number of disturbances due to summer temperatures within the 300-year period 4300 BC - 4000 BC (P1). The largest number of disturbances occurs in the Rocky Mountains, in western Siberia east of the river Yenissei, northern Quebec, and in the coastal regions of Alaska. They are rare around the rivers Ob and Lena, eastern Siberia, and in the plateaus west of the Hudson Bay. Time period P1 is characterized by continuously decreasing 30-year running mean annual T2M. This time period is compared with a second 300-year period between 2100 BC and 1800 BC (P2) with continuously increasing 30-year running mean annual T2M. Figure 3.6 also shows the modelled change of average number of disturbances per year during P1 relative to P2. A large increase is visible over most parts of Siberia and the high north Canadian Arctic. While in western Canada and in

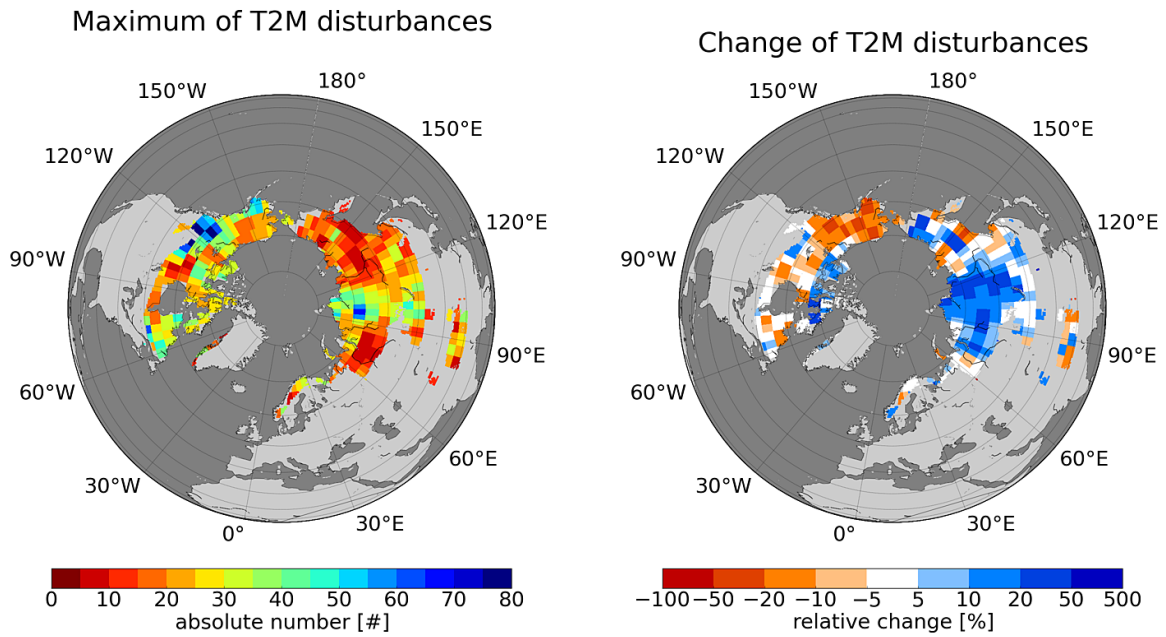


Figure 3.6: The annual number of disturbance events by average summer air temperature is shown for a period (P1) of decreasing 30-year mean T2M (4300 BC - 4000 BC) and for a period (P2) of increasing 30-year mean T2M (2100 BC - 1800 BC). The left panel shows the maximum during P1 and the right panel shows the relative change of the average number of disturbances from P1 to P2.

Alaska the number of disturbances decrease. A regional cooling might have occurred there. Changes in vegetation cover are a second source for thermokarst. They play a role in regions of tundra and taiga with significant vegetation cover. Vegetation is dried out during droughts. Therefore, it becomes vulnerable to wildfire. Intensive wildfires can burn deep layers of the biomass resulting in enhanced top-down thawing of permafrost. Every fire event can trigger thermokarst, independent from burned area fraction of the grid-cell (*burn*). Large fires can act just surficial while local fires can reach large depths. The probability of a unit area to become thermokarst is assumed to be homogeneous. Therefore, the number of disturbances due to wildfires ($ndist_{burn}$) linearly increases with burned area fraction (see Eq. 3.25).

$$ndist_{burn} = burn * k_{burn} \quad (3.25)$$

The coefficient k_{burn} was set to 20000 for the first tests. Actually, CLIMBA modelled an average burned area fraction of $0.000011 \text{ m}^2/\text{m}^2$ between 55°N and 75°N within period 5999 BC and 5000 BC (Bruecher et al., 2014). A maximum burned area fraction of 0.000713 has been reached during the period, resulting in 14 disturbances due to wildfires with the parameter setting above. As expected, the maximum number of disturbances during period P1 is lowest in tundra regions and zero in regions with mainly bare soil. Therefore, the highest number of triggered events can be found in the southern regions of the permafrost areas. These are for example western Siberia, central Canada, flatlands south of Hudson Bay, and Lake Baikal in southern Siberia, as it is visible in figure 3.7. The number of disturbances has dropped by more than 20 % in most parts of Siberia and in the Rocky Mountains, and in Alaska from period P1 to P2. The increase

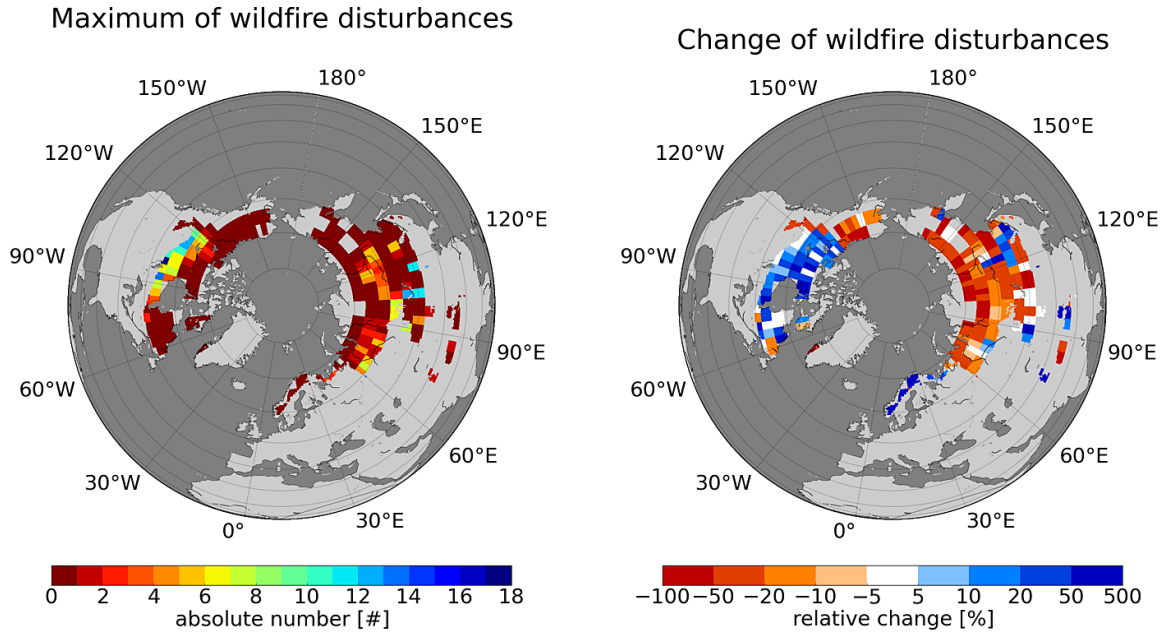


Figure 3.7: The annual number of disturbance events by accumulated burned area fraction is shown for a period (P1) of decreasing 30-year mean T2M (4300 BC - 4000 BC) and for a period (P2) of increasing 30-year mean T2M (2100 BC - 1800 BC). The left panel shows the maximum during P1 and the right panel shows the relative change of the average number of disturbances from P1 to P2.

of wildfire events in Canada can be related to vegetation growth in general, since glaciers of the last glacial period have still remained during the early parts of the Holocene.

Changes within the hydrology can be a main source of thermokarst. One consequence can be an increase in top-down thawing of permafrost. In this case, changes in hydrology mean an increase in available water or snow. Snow can have a severe influence on the soils heat balance, especially during the winter season. Since snow dampens winter temperature exponentially with depth, early snow cover and a thick snow layer can prevent freezing of the upper soil layers during winter (section 3.2.2). The thermal state of the soil changes and heat can penetrate into deeper layers of the soil and causes upper permafrost layers to thaw during the following summer season. The damping effect increases exponentially with winter snow water equivalent depth ($wsnow$). Therefore, the number of snow disturbances ($ndist_{wsnow}$) increases exponentially with the ratio between the anomaly from average snow depth between November and April ($wsnow - \mu_{wsnow}$) and the standard deviation (σ_{wsnow}), as formulated in equation 3.26. April and November have been chosen because freezing is dampened. Later in May, snow is preventing soil from being thawed and limits formation of thermokarst.

$$ndist_{wsnow} = \max \left(0, a_{wsnow} * \frac{wsnow - \mu_{wsnow}}{\sigma_{wsnow}} \right)_{wsnow}^b \quad (3.26)$$

Coefficients a_{wsnow} and b_{wsnow} are factor and exponent of the relationship. For the first tests they have been set to $a_{wsnow} = 1$ and $b_{wsnow} = 3$ and will be evaluated in chapter 4. The maximum number of triggered disturbances due to winter-snow-water-equivalent depth within the time period P1 is observed in the mountains south of the Lena River, at the southern coasts of eastern

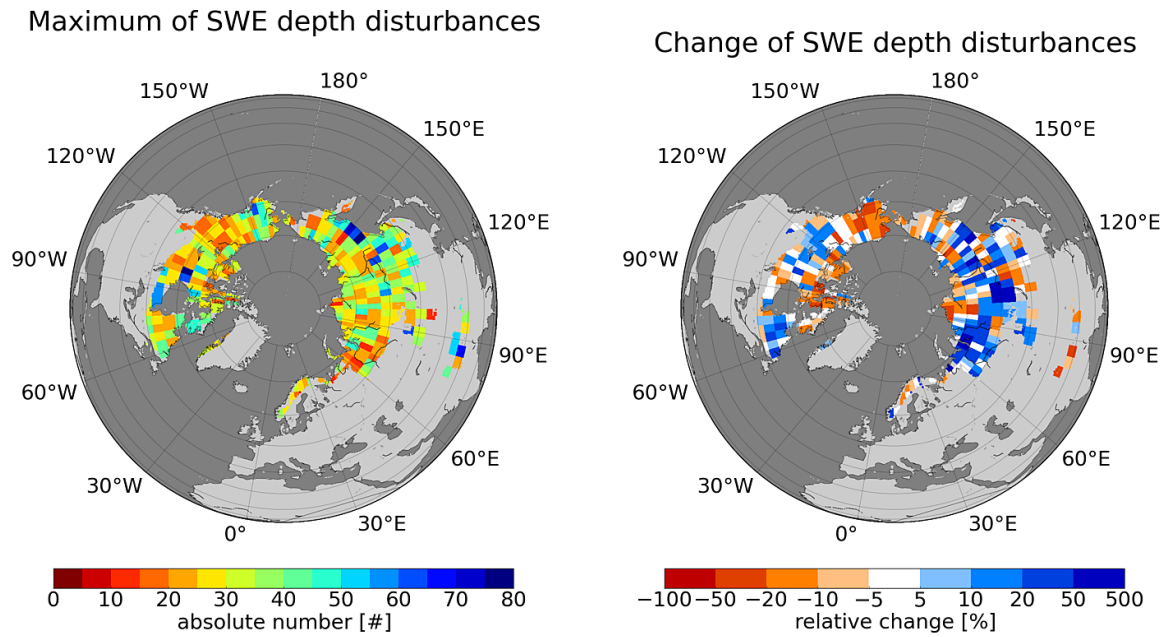


Figure 3.8: The annual number of disturbance events by average winter snow water equivalent depth is shown for a period (P1) of decreasing 30-year mean T2M (4300 BC - 4000 BC) and for a period (P2) of increasing 30-year mean T2M (2100 BC - 1800 BC). The left panel shows the maximum during P1 and the right panel shows the relative change of the average number of disturbances from P1 to P2.

Siberia and Hudson Bay, most parts of Alaska, and west of the Hudson Bay. In Siberia the pattern of higher and lower number of disturbances is very inhomogeneous. Nevertheless, disturbances are rare around the Ob River, in the Rocky Mountains, around the Mackenzie River, and in central Canada, see figure 3.8. The number of disturbances increases by more than 10 - 50 % in most parts of Siberia and Canada from period P1 to P2. However, $dist_{wsnow}$ decreases in Alaska, in northern Siberia, and in the Canadian Archipelago.

Another consequence of hydrological changes is the enhanced erosion and flood activity. If more water is added to a grid box than leaves, water accumulates at the surface and floods develop. Floods cause erosion in many forms, like fluvial erosion along the rivers, coastal erosion at the sea coasts, and surface erosion. The reason of water excess can be either a heavy rainfall event or voluminous snow melt. In the Arctic, snow melt usually occurs from May to early June. The amount of melted water within one month depends on snow depth and on the temperature. Soil moisture is computed with the 5-layer hydrology model in JSBACH (Hagemann and Stacke, 2014). Changes of the soil moisture can be linked to water input. Surface water either flows off as surface runoff (*surf*) or infiltrates into the soil (*infil*). One part of the infiltrating water increases the water table and the other part leaves the soil column as drainage (*drain*). The sum of drainage and surface runoff is called runoff (*runoff*). If runoff equals the total water input, the soil moisture remains constant. The Holocene run from CLIMBA provides soil moisture data on a monthly basis. Actually, a relative change from beginning to the end of one month would be needed to judge a flood event.

Another way to calculate infiltration is to build a water balance at the surface. Water input

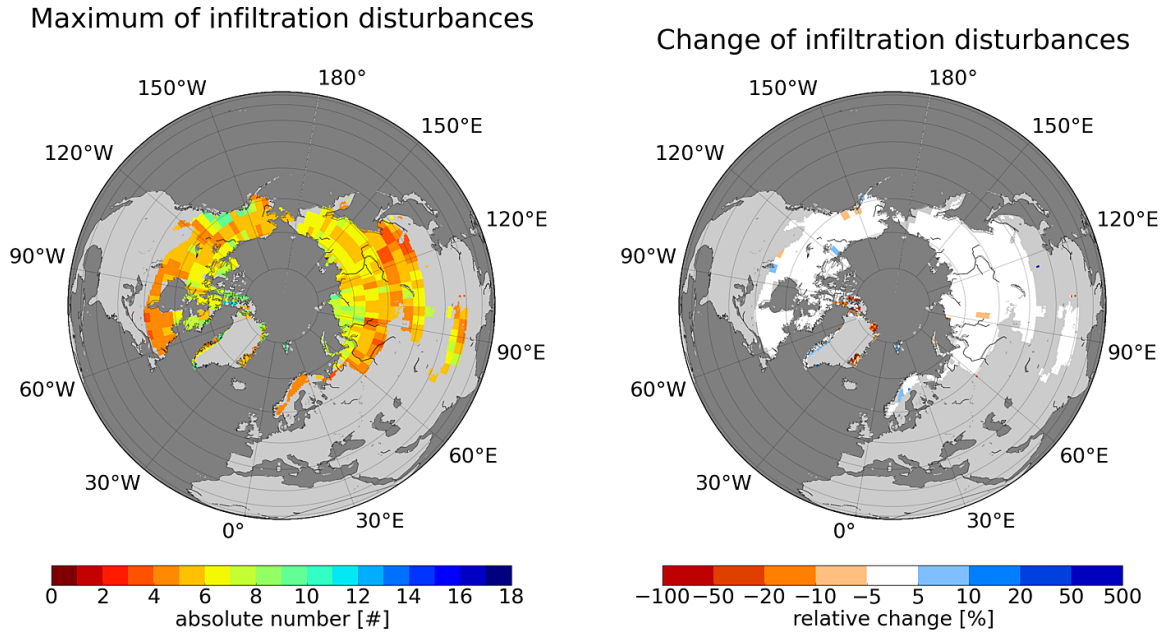


Figure 3.9: Annual number of disturbance events by infiltration for a period (P1) of decreasing 30-year mean T2M (4300 BC - 4000 BC) and for a period (P2) of increasing 30-year mean T2M (2100 BC - 1800 BC). The left panel shows the maximum during P1 and the right panel shows the relative change of the average number of disturbances from P1 to P2.

equals water output. Water input is composed by snow melt (*snowmelt*) and liquid precipitation (*rainfall*). The difference between water input and surface runoff is actually the water, which infiltrates into the soil. The number of disturbances caused by infiltration ($ndist_{infil}$) is computed as a function of the ratio between the anomaly from the monthly average infiltration ($infil - \mu_{infil}$) and the standard deviation (σ_{infil}). Infiltration is calculated for each month. Disturbances are derived from the sum over monthly values between May ($m1_{infil} = 5$) and August ($m2_{infil} = 8$).

$$infil = snowmelt + rainfall - surf \quad (3.27)$$

$$ndist_{infil} = \sum_{t=m1_{infil}}^{m2_{infil}} \max \left(0, a_{infil} * \frac{infil - \mu_{infil}}{\sigma_{infil}} \right)^b_{infil} \quad (3.28)$$

Coefficients a_{infil} and b_{infil} are factor and exponent of the relationship. For the first tests a_{infil} and b_{infil} have both been set to 1. The peak of infiltration disturbances should be settled at $1 \sigma_{infil}$, because flood events of any size can enhance erosion processes and trigger thermokarst. Furthermore, hydrological impacts are assumed to be the most important source for disturbances (G. Grosse, 2014, pers. comm.). Since infiltration disturbances are separately computed for each month of the period $m1_{infil}$ and $m2_{infil}$, their importance is enhanced in comparison to other types of disturbances. Initially during one time-step (1 year) $dist_{infil}$ is computed 4 times, while the others are compute only one time. During the time period P1, the largest number of infiltration disturbances occurred in northern and eastern Siberia, southern Alaska, and in the Canadian archipelago, see figure 3.9. The average number of disturbance is fairly the same in both time periods and has hardly changed by more than 5 % from period P1 to period P2.

Every disturbance triggers thermokarst and leads to formation of new ponds within the model. However, in reality some disturbances may not trigger thermokarst if they affect soils with a very little amount of excess-ice. Permafrost thaws as well, but not enough ice is melted to leave larger depressions which can be filled with water. Thus, permafrost and vegetation can recover again. It is not known where the disturbance occurs within one grid cell neither if a part with higher or lower ice content is affected. Therefore, a thermokarst triggering disturbance is assumed in any case, while disturbances are homogeneously distributed over the whole grid cell.

$$nlakes_{new} = (ndist_{stemp} + ndist_{wsnow} + ndist_{burn} + ndist_{infil}) * \frac{A_{box} * perm_{fract}}{10^9} \quad (3.29)$$

The number of new lakes is basically the sum of all disturbances caused by different climate extremes. To obtain the total number of new lakes within one grid cell ($nlakes_{new}$) the sum is projected with the area of available permafrost, which is $A_{box} * perm_{fract}$. This is important to ensure that the same disturbance impact leads to the same disturbance fraction (see Eq. 3.8), since the cell area decreases with increasing latitude. Furthermore, $nlakes_{new}$ is defined to develop per 1000 km² or per 10⁹ m². This number was chosen because lower and higher values lead to unrealistic large and small lake fractions, respectively.

3.3.2 Development of a talik below thermokarst lakes

After a disturbance, ponds form (Sect. 3.3.1) and progressively develop to large lakes due to expansion in size and depth. This section deals with thawing of soils below TKL and soil . Melting of excess-ice also influences the fraction of the disturbed area covered with water, as discussed in sect. 3.2.1. The lateral expansion will be discussed in sect. 3.3.3.

The development of a talik beneath TKL has been successfully modelled for single lakes in previous studies (West and Plug, 2008; Kessler et al., 2012; Yi et al., 2014).

Kessler et al. (2012) applied a 1D heat conduction model (e.g. Burn, 2000) and improved it with lateral heat flows. The rate of ice-melt at the phase change boundary was reduced by heat flows from the talik into the surrounding permafrost.

West and Plug (2008) initialized a single lake and talik model and simulated development over 5000 years. A two-dimensional finite difference model was applied to investigate the relationship between talik growth, ice-melt, and soil subsidence, lateral erosion at the margins, lake area, and lake depth. The set up is explained in detail here, because the results are used as a base for parametrisation of the talik growth within the TAPAS model. Lakes, which were developing on ice-rich soils, reached a depth of 20 m within 5000 years, while lakes on ice-poor environments only developed a depth of 3 m and were flat bottomed. Lakes with disequilibrium talik developed margins of more than 100 m width. If the annual mean air temperature of the lake bottom exceeded 0°C, then talik formed, which developed downward from the lake bottom and reached a maximum size of 73 m, as it had been measured by borehole drilling in the Mackenzie Delta (Johnston and Brown, 1961).

Precise information about relationships between climate and lake size, lake ice, and lake temperature were not available. For their simulations, West and Plug (2008) used a water temperature of 3°C to match the narrow range of available measurements. The annual mean ground temperature was set to -8°C. The goal was to investigate talik and bathymetry development for a lake with a

radius of 350 m and 2 m depth under different ground-ice depths and soil constitutions over 8000 years, table 3.2. Both scenarios were computed with an ice-content of 30 %, but one with an ice depth of 5 m and the other with an ice-depth of 300 m. The final lake depth directly depended on

Year	Lake	Talik	Lake	Talik
0	2.0	0.0	2.0	0.0
100	2.2	9.1	4.8	9.3
500	2.2	12.9	6.9	16.2
3000	2.2	32.3	14.1	40.3
8000	2.2	48.0	24.0	67.0

Table 3.2: Development of talik depth and lake depth over 8000 years. 2 simulations with ice-content of 30 % but with an ice depth of 5 m (left columns) and 30 m (right columns). The values are based on graphical output of figure 1 in (West and Plug, 2008)

the volumetric excess-ice content and on the thawed soil column. Within the deep ice scenario a soil depth of 67 m was thawed. This resulted in a thaw settlement of 22 m and a final talik thickness of 45 m, which agreed well with the expected volume loss due to the 30 % ice content. After 8000 years, talik has reached an equilibrium state in both scenarios. However, the shape of the lakes differed between both cases. In the deep ground-ice scenario continuous subsidence resulted in a deep lake with inclined margins. In the other scenario the lake remained shallow and flat. The flat ice scenario is physically more relevant because ice wedges can grow downwards to a maximum depth of 10 meters (Black, 1976). Since overburden pressure increases with depth and dampens freezing temperature, the cryosuction potential decreases (Konrad, 1990). Therefore, the results from the flat ice scenario are used for parametrizing talik growth within the TAPAS model.

The clustering of TKL in age classes of equal properties allows computing talik for each sample. However, energy processes are not included into the TAPAS model (Sect. 3.3.6), because only monthly data are available from the CLIMBA Holocene run. Short periods of freezing or melting are blurred out within the monthly mean as well as daily variations of the water table. Therefore, melting and freezing processes can not be directly simulated in this model version. Since the TAPAS model is executed once per year, only the maximum thawing depth is simulated. Talik depends on the average lake bottom temperature and develops if the maximum thawing depth exceeds the maximum freezing depth. Since driving data from CLIMBA and JSBACH are available down to a depth of 9.83 m, the maximum depth of the talik is 9.83 m within the TAPAS model. Actually, this depth is reached within 50 years (Kessler et al., 2012), what is fast in comparison to the lifetime of one TKL.

Following the flat-ice scenario in West and Plug (2008), talik growth is parametrized with the square root of time within the TAPAS model. The coefficients of equation 3.30 arise from filling in values from table 3.2. The talik of lakes is computed analogous to

$$h_{talik} = 0.30 * a * \sqrt[2]{b * t}, \quad (3.30)$$

with $a = 5.7$ and $b = 0.2$. The progression over time is shown in figure 3.10. The factor 0.30 represents the ice content of 30 % within the scenario. A clear connection between ice-content and talik development could not be found within the literature.

The actual lake depth (h_{lakes}) is primarily dependent on the ice content and the talik depth, which are known for each age class. The talik depth is calculated with the average age and is the same as the melting depth. Two points have to be considered while calculating the melted ice column. First, the soil column inherits excess-ice only until a depth of 10 m (Black, 1976) and second, driving data from JSBACH are only available down to a depth of 9.83 m as already mentioned above. Additionally, the uppermost soil layers are already thawed due to the annual freezing and thawing cycle. Therefore, the maximum talik thickness is the difference between ALD and the total soil thickness of 9.83 m. The ice content of the thawed soil column regulates the melted ice depth (h_{melt}). Regarding the density change during melting of frozen water, it is possible to compute the final lake depth (h_{lakes}).

$$h_{melt} = \min(9.83 - ALD, h_{talik}) \quad (3.31)$$

$$h_{lakes} = ice_{ave} * \frac{\rho_{water}}{\rho_{ice}} * h_{melt} \quad (3.32)$$

The lake depth is the prime result of modelling the talik thickness. It describes the amount of liquid water and enables a mass balance between frozen and melted water. For the volume of melted water (V_{lakes}) only the area covered by TKL of a certain depth is needed (A_{lakes}). The area can be determined easily, because all lakes of a certain age class (n_{lakes}) have the same depth and the average area (A_{ave}), as explained in sect. 3.1.2.

$$A_{lakes} = n_{lakes} * A_{ave} \quad (3.33)$$

$$V_{lakes} = A_{lakes} * h_{lakes} \quad (3.34)$$

3.3.3 Lake expansion rate

Modelling of changes within the lake area is important for future projections of the carbon budget within the Arctic and for predicting the potential release of carbon due to lake expansion, which is a form of surface permafrost degradation (Jones et al., 2011). The parametrisation of lake expansion is based on observations described in the paper referred to. Jones et al. (2011) investigated lake area changes on the Seward Peninsula in Alaska with satellite based images of three time slices within 57 years between 1950 and 2007. High spatial resolution multi-spectral IKONOS satellite imageries and historical aerial photography were used for an area of 700 km². The Digital Shoreline Analysis System (DSAS) extension for ArcGIS (Thieler et al., 2009) served as a method to derive detailed lake expansion rates. An error of 0.09 m/y can be expected from error estimation of linear expansion rate measurements (Jones et al., 2011). The expansion rate was investigated in more detail for four size classes between 0.1 ha and 400 ha. The most important result of the study is that the expansion rate increases with size. The largest rates were found for lakes of 40 - 400 ha with 0.59 m/y and 0.62 m/y, during the time periods 1950/51 - 1978 (TP1) and 1978 - 2006/07 respectively (TP2). The next lower size class (10 - 40 ha) shows significantly weaker rates of 0.35 m/y and 0.38 m/y, respectively. Generally lakes larger than 10 ha did not show a significant change of the expansion rates between the two time periods. But the expansion rate of lakes smaller than 1 ha increased from 0.10 m/y (TP1) to 0.22 m/y (TP2). A potential reason can be that smaller lakes expand due to thermal erosion while on larger lakes mechanical erosion predominates. The efficiency of wave action increases with open water

Parameterizations of the thermokarst model

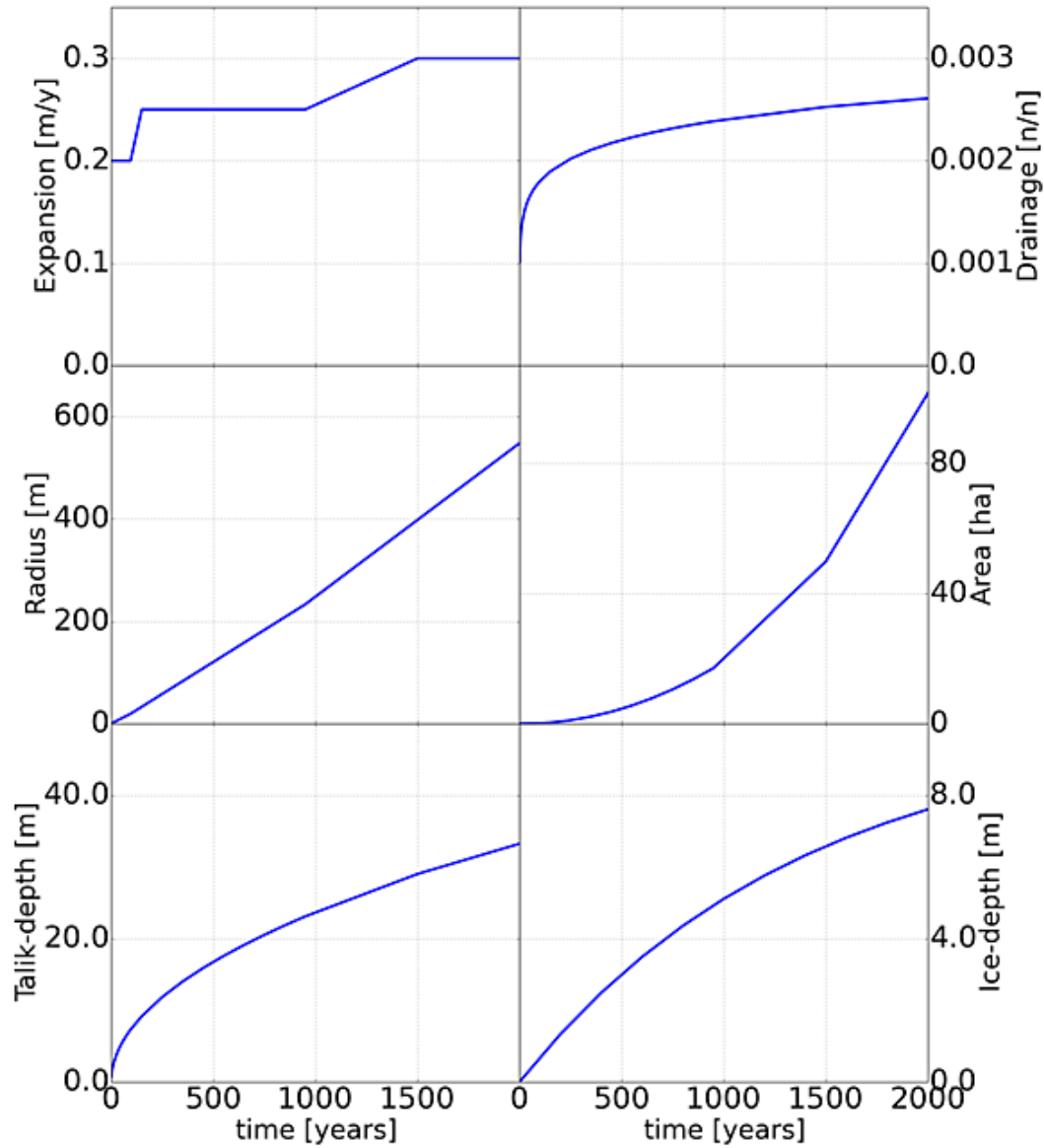


Figure 3.10: First setup of lakes properties as a function of time and age class. From top left to bottom right, the figure represents development of expansion rate, drainage probability, radius and area of thermokarst lakes, talik depth, and ice depth with time. The functions represent the prescribed development with time or age class and are explained in detail in chapter 3.3.

extension (Jones et al., 2011). The observed climate warming may have increased the water temperature and, therefore, also the thermal erosion. On average, thermokarst lake expansion rates did not change substantially between 0.35 m/y in TP1 and 0.39 m/y in TP2 (Jones et al., 2011).

There are three steps visible within the development of the expansion rate. Probably, some thresholds exist. The thermal state of one thermokarst lake changes severely, if lake depth increases. The thawing depth increases strongly if the lake depth increases from 1 m to 2 m. A further increase of the lake depth does not severely alter the thawing depth (Yi et al., 2014). Once a lake does not freeze up completely during winter, the temperature of the lake bottom is not dropping below freezing temperature and the soil below of the lake remains thawed. Water ice has higher heat conductivity than fluid water. Therefore, the soil layers freeze during winter or are isolated by the water body. At 2 m depth the water temperature drops to a minimum of 0°. At 6 m depth it drops to a minimum of 3 °C. Therefore, more heat can be stored within the soils and talik expands faster in depth and size.

Presumably, lakes smaller than 10 ha are growing due to thermal erosion, while larger lakes are primarily growing due to mechanical erosion (Jones et al., 2011). For the TAPAS model this means that a shift can be expected after 500 to 800 years, depending on the prescribed expansion rate. There is also a large difference within the expansion rate of lakes between 10 - 40 ha and 40 - 400 ha. This is because winds can transfer more kinetic energy towards lakes of larger surface area. In the beginning, mounds are circular and regular shaped, but waves increase lateral erosion on the lakes margin and increase expansion towards a wind favoured direction. In the Lena river delta for instance, lakes smaller 20 ha are primarily WNW orientated and lakes larger than 20 ha NNE orientated (Morgenstern et al., 2011). Obviously, there is a 90° shift in orientation. Reasons for the phenomenon are still under debate. One reason can be that the main summer wind direction change during earlier parts of the Holocene. Larger lakes may have formed under different wind conditions in earlier times. However, if the wind direction remains stable, the wind effect may change from wave-induced erosion (abrasion) in the wind direction to the establishment of wind-driven currents and wave activity perpendicular to the main wind direction (Morgenstern et al., 2011).

Overall, the expansion rate of one TKL increases from 0.1 m/y to 0.6 m/y, from small ponds to large lakes respectively. The expansion rate is highly dependent on the lake area and on temperature. Since no energy transfers are implemented within the TAPAS model, the expansion rate can only be prescribed as a function of the area of one lake. At least two shifts from thermal to mechanical regime are observed within the expansion rates. Following the observations, the expansion rates (*expand*) are modelled in three steps. After personal communication with G. Grosse (2014) the following initial magnitudes have been applied:

- Lakes smaller than 1 ha or age classes 01 - 20 expand by $expand1=0.20$ m/y
- Lakes of area 1 ha - 10 ha or age classes 21 - 25 expand by $expand2=0.25$ m/y
- Lakes of area 10 ha - 40 ha or age classes 26 - 27 expand by $expand3=0.25$ m/y
- Lakes larger than 40 ha or age classes 28 - 33 expand by $expand4=0.30$ m/y

$expand1$, $expand2$, $expand3$, and $expand4$ are 4 parameters of the TAPAS model. The rates are relatively conservative and heavily restricted to the growth of large lakes. In comparison to the observations described above, the expansion rate for lakes larger than 40 ha is only half of it. Nevertheless the expansion rates fall within the range of measured long term means of various regions in Alaska, Canada, and Siberia (Jones et al., 2011).

Within the TAPAS model, all lakes start as circular mounds with an area of 1 m^2 (A_0), which is the average area of lakes (A_{ave}) of the first age class. They expand homogeneously in all directions. In reality topographic heterogeneities lead to inhomogeneous expansion. The initial area corresponds to an initial circle radius of 0.56 m (r_{ave}). The expansion rate tells the growth for each year. If the number of years between two age classes ($age1$, $age2$) is known, then the final radius can be determined from adding the total expansion to the old lake radius. The average area of lakes within each age class follows from the average radius:

$$r_{ave}(age2) = r_{ave}(age1) + expand(age1) * (age2 - age1) \quad (3.35)$$

$$A_{ave}(age2) = r_{ave}(age2)^2 * \pi \quad (3.36)$$

3.3.4 Drainage probability of thermokarst lakes

The last step of the lifetime of one thermokarst lake is marked by partially to complete drainage of the water body. It is the transition from degrading permafrost to recovering permafrost and aggregation of excess-ice. The parametrization of lake drainage mainly follows observations discussed in Jones et al. (2011).

In regions with continuous permafrost (see table 2.1 and figure 2.2), drainage of thermokarst lakes can be triggered by expansion towards a lower levelled adjacent basin, fluvial "tapping" along ice-wedge systems, connection to river and drainage networks, stream meandering, or coastal erosion (Hinkel et al., 2007; French, 2007; Jones et al., 2011; Grosse et al., 2011). If talik penetrates the permafrost, as it is possible in discontinuous permafrost regions, also subterraneous drainage can happen (Yoshikawa and Hinzman, 2003). Appropriate knowledge about drainage mechanisms is important, since catastrophic lake drainage leaves large basins and increases surface erosion. A drainage event is defined as a reduction in lake surface area by more than 25 % (Jones et al., 2011; Hinkel et al., 2007). It marks the end of lake development. The former lake bottom is influenced by the seasonal cycle of Arctic temperatures again. The thermal regime of the soil changes severely and permafrost recovers. In the TAPAS model the concerned areas are handed over to the age class of drained basins. It is represented by age class 34 in table 3.1. It represents the start of the basin age classes. The ice content is usually zero in the beginning and accumulates over time until maximum ice-depth has been reached.

Besides expansion, Jones et al. (2011) also investigated drainage of thermokarst lakes in

Size Range	Lakes 1950	Lakes 1978	Events p1	Events p2	Prob p1	Prob p2
0.1ha-1ha	379	392	31	38	0.0029	0.0033
1ha-10ha	214	212	18	12	0.0030	0.0020
10ha-40ha	44	50	7	10	0.0057	0.0069
40ha-400ha	29	26	5	8	0.0063	0.0108

Table 3.3: This table lists the drainage probability of lakes within an area of 700 km² on Seward Peninsula. The numbers of lakes and events are gathered from figure 3 and table 1 in Jones et al. (2011). Listed are the number of lakes at the starting points of period 1 (1950/51 - 1978) and period 2 (1978 - 2006/07), number of drainage events, and the retrieved drainage probability.

Seward Peninsula. The resolution of satellite images allowed investigation of area changes of lakes and ponds of sizes larger than 0.1 ha. They were sorted in four size classes, as listed in table 3.3. Between 1950/51 and 1978 the total number of lakes increased from 666 to 680. Between 1978 and 2006/07 the number increased further to 737. There, 61 drainage events have been observed during the first time period and 68 during the second time period. The lake drainage probability has remained fairly stable over the last half century (Jones et al., 2011). This corresponds to 2.17 and 2.34 drained lakes per year. According to the observed number of lakes and drainage events, the overall drainage probability is 0.0033 during the first time period and 0.0035 during the second time period. Table 3.3 lists the equivalent numbers for each size class. The drainage probability depends on size of the water body and increases from small ponds to large lakes. A polynomial relationship can be assumed as suggested by observations. Actually, analysis of climate data over the 57 year study did not show a clear connection between climate and thermokarst lakes (Jones et al., 2011). As for the expansion rate, the drainage probability remained fairly constant, comparing the time periods TP1 and TP2. Little changes have been attributed to measurement uncertainty (Jones et al., 2011).

For understanding the full thermokarst lake dynamics, it is important to proceed with a combined analysis of lake surface area changes and lake abundance (Jones et al., 2011). Drainage is not affecting a lake in that way that it is draining completely. Large lakes tend to drain partly and leave several small lakes and ponds. During the observation period of 57 years, 71 additional lakes have developed, but a majority of 60 of them stem from partial drainage of larger thermokarst lakes and division into remnant water bodies (Jones et al., 2011). Therefore, the large increase in the number of small lakes in connection to decrease of large lakes may have resulted from partial drainage events.

The drainage probability increases with increasing area of TKL. Since the size of one lake usually is strongly connected to the age, the drainage probability can also be expressed as a function of time t . A simple polynomial function of higher order is used for parametrization (Eq.3.37) in the TAPAS model. The coefficients a and b of equation 3.37 can be retrieved with the prescribed drainage probability of lakes after 100 years $drain_{100}$ and of lakes after 1000 years $drain_{1000}$ (see Eq. 3.38 and 3.39). Drainage is zero at $t = 0$, therefore, $c = 0$. $drain_{100}$ and $drain_{1000}$ are

two parameters of the TAPAS model.

$$drain(t) = a * t^b + c \quad (3.37)$$

$$b = \frac{\log(drain_{1000}/drain_{100})}{\log(10)} \quad (3.38)$$

$$a = \left(\frac{drain_{1000}}{1000} \right)^b \quad (3.39)$$

For the first model runs the drainage probabilities were set to 0.0018 and 0.0024 after 100 years and 1000 years, respectively. It is set slightly lower than it was observed in northern Seward Peninsula, because it is likely that this region exhibits the highest thermokarst drainage probability found in the entire Arctic (Jones et al., 2011). The TAPAS model was tested with changing drainage probabilities until the modelled lake fraction was comparable with MODIS satellite observations of the ESA-DUE Permafrost Project (Bartsch et al., 2012) at two grid points with a large number of TKL. During the sensitivity study, different drainage probabilities will be tested (see chapter 4).

The drainage probability may also increase with decreasing PF. ALD becomes large and the permafrost layer thinner. It is more likely that the talik penetrates through the permafrost and that a lake drains due to infiltration in the interior. Furthermore the permafrost pattern consists of patches and it is more probable that a lake expands towards an edge of a permafrost area and connects to a drainage network. Based on the assumption of a dependency on PF, a second dimension was added to *drain* (Eq. 3.40). Drainage (*drain(pf, time)*) reaches the maximum of 100 % if PF is zero. By definition, TKL are only forming on permafrost areas. The smallest drainage probabilities are expected for regions with 100 % permafrost ($PF = 1$). The ideal case of equation 3.40 reduces to a polygonal function with coefficients a and b (see equation 3.37 with $c = 0$).

$$drain(pf, t) = (a * t^b)^{(PF)^p} \quad (3.40)$$

A new coefficient (p) is introduced, to enable predefinition of increased drainage probability with decreasing PF. If PF reduces from 100 % to 10 %, drainage is amplified by a certain factor ($drain_{ampl}$). For the first attempt, $drain_{ampl}$ was set to 2.0. This means, that drainage probability increases by 100 %. The amplification factor in combination with the coefficients a and b can be used to determine the coefficient p via transforming equation 3.41 with $drain_{1000} = a * 1000^b$ to equation 3.42.

$$(drain_{1000})^{(0.1)^p} = drain_{ampl} * (drain_{1000})^{(1.0)^p} \quad (3.41)$$

$$p = \frac{\log\left(\frac{\log(drain_{ampl} * drain_{1000})}{\log(drain_{1000})}\right)}{\log(0.1)} \quad (3.42)$$

Figure 3.10 shows the progression of drainage probability with time, computed with equation 3.40 for regions with 100 % permafrost ($PF=1$). The parameters have been set to $a = 0.0010125$, $b = 0.125$, and $p = 0.05$ (as derived above).

The drainage parameters $drain_{100}$, $drain_{1000}$, and $drain_{ampl}$ will be tuned to optimize the model performance during the sensitivity studies in section 4.3.

3.3.5 Accumulation of excess-ice

Here, the aim is to describe the ice formation scheme, which has been implemented into the TAPAS model. A reliable implementation of recovering permafrost in drained basins has to be modelled as well to complete the thermokarst process, since segregated excess-ice in permafrost soils is a precondition for landscape forming thermokarst. Different types of massive ice bodies are developing there and each of them causes frost heave of the surface. They can be differentiated in form and shape. An overview of the ice bodies and the processes behind them is given in section 2.4. Additionally, there are three limitation factors acting on formation of excess-ice. These are, as described here: pore-size of the soil, topographic slope, and the available volume of liquid water.

The growth of excess-ice has not been modelled on the global scale yet. The growth rate varies by several magnitudes between different features of excess-ice. The annual growth rate of ice wedges ranges between a fraction of a millimetre and several millimetres per year (Black, 1976). Pingos show fast growth rates in the beginning, which decreases from about 1 m/y in early stage to 2 - 3 cm/y after one millennium. Palsas grow gradually over time and persist for many decades (French, 2007).

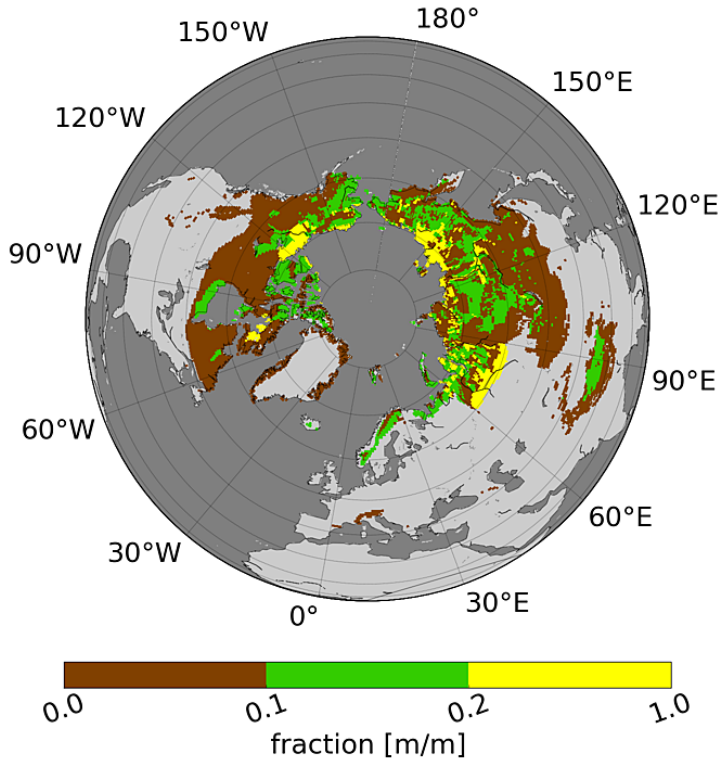
Actually, a 3-D numerical ice simulation scheme has been developed for a single lake (Kessler et al., 2012), which describes formation of ice wedge polygons. The growth rate was described as a function of decaying ice deficit towards a maximum excess-ice volume (Eq. 3.43). The change in volume of ice (ΔV) during a time period (Δt) depended on the excess-ice growth timescale (τ) and the difference between the maximum and the actual volume of ice (Kessler et al., 2012).

$$\Delta V_{ice} = \frac{\Delta t}{\tau} * (V_{ice}^{max} - V_{ice}) \quad (3.43)$$

The same methodology is applied within the TAPAS model. The volume is replaced by ice depth (z_{ice}) (Eq. 3.45), because ice growth is independent of surface area. Thus, the excess-ice depth (z_{ice}) is modelled by TAPAS as a decay of the ice deficit towards a maximum ice depth. The magnitude of ice depth increases by Δz and can be explained as a function of decreasing difference between the actual ice depth and the maximum ice depth (z_{ice}^{max}). From Eq. 3.44 it follows that the excess-ice depth increases logarithmically over time. An example is shown in figure 3.10. Then, the volume of new excess-ice is calculated with the area covered by one age class and the change in ice depth (Δz_{ice}) (Eq. 3.45). For the first model runs the time-scale (τ) is set to 1500 years and the maximum ice depth to 10 m. Kessler et al. (2012) used a shorter time-scale of $\tau = 1000$ y. However, too high ice content values have been received from first test runs. Therefore, τ is set to a larger value than used by Kessler et al. (2012).

To distinguish between the different mechanisms of ice formation, the pore-size ($pore_{size}$) was added to the TAPAS model. Pore-size drives cryosuction, which leads to formation of pingos and palsas in warm permafrost areas. It is less important for the development of polygons in cold permafrost areas, because polygons form due to cracking of upper soil layers. Therefore, thresholds of ice formation regimes have been introduced as described below. Furthermore, excess-ice primary forms in flat regions and is rare in mountainous regions. The slope limitation parameter f_{shape} is introduced here to regard the effect of slope (see equations 3.44 and 3.46).

Ice content distribution from NSIDC



Ice Content	Average
00 % - 10 %	05 %
10 % - 20 %	15 %
20 % - OE %	25 %

Table 3.4: The ice content classes are shown here which are provided by NSIDC (Brown et al., 1998). An artificial average is defined to evaluate the modelled ice contents and to derive the ice distribution functions, which are described in section 3.4.2.

Figure 3.11: This figure shows the average ice content as it is provided by NSIDC (Brown et al., 1998).

$$\Delta z_{ice} = \frac{\Delta t}{\tau} * (z_{ice}^{max} - z_{ice}) * f_{shape} \quad (3.44)$$

$$\Delta V_{ice} = \Delta z_{ice} * dist_{fract} * A_{land} \quad (3.45)$$

$$\Delta z_{ice} = \frac{\Delta t}{\tau} * (z_{ice}^{max} - z_{ice}) * pore_{size} * f_{shape} \quad (3.46)$$

The transition between different mechanisms of ice formation is not sharp, and excess-ice features may also develop beyond the margins. As shown in Washburn, 1980, polygons develop in regions with an annual mean air temperature of less than -4 °C and palsas in regions warmer than -8 °C. However, a transition exists from suction-dominated to gravitation-dominated formation. In cold regions not much fluid water is available within the soils. For these regions, Eq. 3.44 is applied to describe the growth of excess-ice, while for warmer regions the pore-size ($pore_{size}$) limits ice accumulation, since ice accumulation is a function of potential cryosuction (Eq. 3.46).

In the next step, thresholds needed to be found, which limit ice aggregation within a certain region. For this task, the observed ice contents from NSIDC (Brown et al., 1998) have been compared with long term mean annual air temperature between 1958 and 2000 (Weedon et al., 2011), as shown in figures 3.12 and 2.1, respectively. The distribution of excess-ice has been

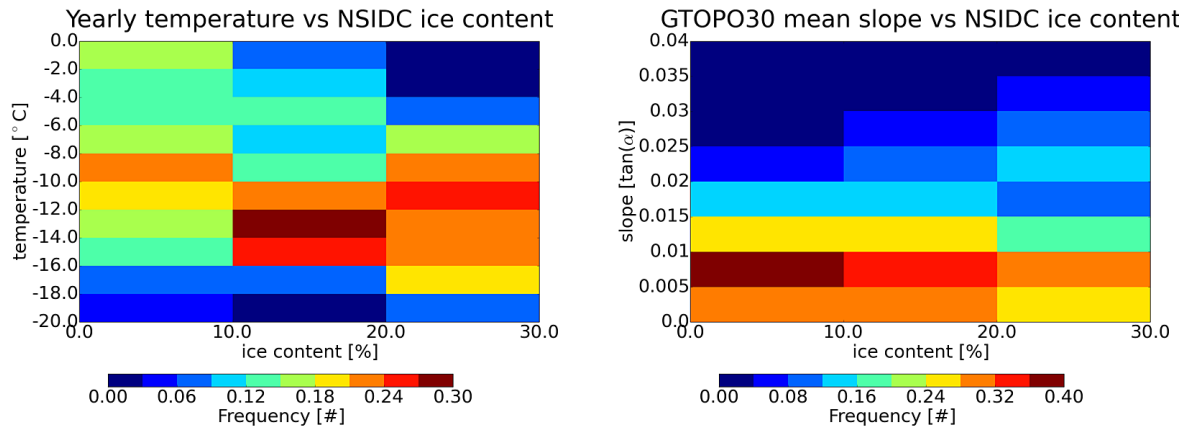


Figure 3.12: Threshold study of ice formation between NSIDC average ice values (Brown et al., 1998) and WFD annual mean temperature (Weedon et al., 2011) (left panel) and average subgrid slope (Stacke and Hagemann, 2012) (right panel).

remapped on 0.5° grid. Figure 3.12 shows the frequency of observed ice contents at different temperatures in 2°C intervals from 0°C to -20°C . For each ice content class, the sum of frequency is normalized to one. The ice content classes are listed in table 3.4. Obviously the ice content increases with decreasing temperature. The smallest ice contents develop within a temperature range of between 0°C and -12°C and the highest ones between -6°C and -18°C . The reason for the phenomenon can be that ice forms more efficiently in cracks rather than due to cryosuction. Furthermore, less water freezes at higher temperatures. To conclude the threshold study, there are probably three thresholds of ice formation. They are settled at 0°C ($thres_{ice1}$), -8°C ($thres_{ice2}$), and -18°C ($thres_{ice3}$) and will be evaluated during the sensitivity studies. However, based on literature (Washburn, 1980), different thresholds of ice formation are used as initial setting.

- upper threshold ($thres_{ice1}$): $T2M_{y\text{mean}} = -1^\circ\text{C}$
- medium threshold ($thres_{ice2}$): $T2M_{y\text{mean}} = -4^\circ\text{C}$
- lower threshold ($thres_{ice3}$): $T2M_{y\text{mean}} = -16^\circ\text{C}$

Excess-ice aggregates in regions with temperature of less than -1°C and ice wedge polygons develop already in regions with a temperature of less than -4°C (as described in section 2.4). Between the upper and the medium threshold, excess-ice grows due to cryosuction (Eq. 3.46) in form of ice lenses and between the medium and the lower threshold, excess-ice grows due to water infiltration in form of ice wedges (Eq. 3.44). In this sense, the medium threshold acts as a distinction between regions with different regimes of ice formation.

A second important limitation factor has been introduced to improve the excess-ice model in regard to slope. Field observations on Kurungnakh island suggested that the development of ice-wedge polygons was limited in areas with a slope of greater than 2° (Morgenstern et al., 2011). Actually, there is rare ice in the Brook's Range in Alaska, the southern and eastern Siberian mountains, and in the Rocky Mountains, compare figures 3.11 and 3.3. Therefore, the

slope must play an important role for ice formation. In regions with a higher slope, aggregation of excess-ice is limited due to a higher runoff. Excess-ice bodies may still develop but the ice content usually remains lower than in flat terrain.

Resulting from this, a second threshold study is performed. Contrary to the threshold study before, the ice contents from NSIDC are compared with the mean slope, derived from GTOPO30 data set (Stacke and Hagemann, 2012) on 0.5° grid. Again, for each ice content class the sum of frequency is normalized to one. As visible in figure 3.12, a sharp drop of the ice content exists beyond a slope of 0.015 m/m. The frequency of observed ice contents is determined at different slopes in 0.005 m/m intervals from 0.000 m/m to 0.100 m/m. Ice contents larger than 20 % can be observed up to a slope of 0.035 m/m or 2.0° , respectively. The shape of this behaviour can be quite well described by a cosine function. The maximum ice depth is the same for all regions, but the accumulated ice depth (Δz_{ice}) is reduced by the limitation factor of slope (f_{shape}) (Eq. 3.48)

$$\alpha_{slope} = \arctan(slope_{mean}) \quad (3.47)$$

$$f_{shape} = \cos(\min(\pi/2, \alpha_{slope} * 44.848)) \quad (3.48)$$

First, the slope is transformed from gradient [m/m] to angle [rad] (Eq. 3.47). Then, the cosine of the angle is calculated to receive the reduction of ice accumulation or f_{shape} (Eq. 3.48). From the threshold study it follows, that the ice growth drops to zero beyond an angle of 2.0° , i.e. $f_{shape}(\alpha_{slope} = 2.0) = 0.0$. Therefore, the shape parameter is adopted with the factor 44.848. Finally, the accumulation of excess-ice is limited by the amount of liquid water within the soil. During the melting season, a part of the water from precipitation and melting snow is infiltrating the soil and leaves it as drainage, if the field capacity is exceeded. This water is used for excess-ice formation within the TAPAS model. For formation of excess-ice, water is relevant, which would leave the system. Therefore, the annual drainage is applied for ice accumulation. If the amount of water is smaller than ΔV_{ice} , then the difference is assumed to be filled with sand or other material, leading to a reduction of ΔV_{ice} . Observations showed that cracks fill up with other material like sand and develop to sand- or soil-wedges, if too little water is available (Black, 1976).

3.3.6 Energy balance and lake ice formation

In principle, the energy balance of thermokarst lakes should be regarded. Phase changes at the surface of lakes and in the interior of the soil regulate the balance between water and ice. The temperature of the water body influences expansion rate and talik growth. Soil heat transfer models were successfully developed for single lakes during different studies (West and Plug, 2008); Kessler et al., 2012, Yi et al., 2014. Lake evolution severely depends on its depth because permafrost beneath lakes reacts highly sensitive, if the lake depth increases, for example, from 1 m to 2 m (Yi et al., 2014). A transition exists there from freezing up entirely during winter to remaining unfrozen in the lower part. Heat is transported downward from lake surface to lake bottom and into the permafrost. Ponds smaller than 1 meter are permanently mixed up due to convection. Temperature of the soil is approximately the same as the air temperature. Lakes deeper than 1 meter are only mixed down to a certain depth and are layered below. The mixing

depth depends on turbulent kinetic energy induced by wind, which works against gravity force of the mixing layer. The soil temperature is proportional to a damping rate. The second main reason is that lakes freeze up to a certain depth during winter. If lake depth is larger than lake-ice depth, then the soil surface temperature is settled at about 0° and the soil layer below does not freeze (M. Langer, 2014, pers. comm.). If a lake is freezing up entirely, then also soil layers beneath the lake freeze. The surface soil temperature is warmer than the air temperature, due to heat isolation. Additionally snow falls on the top of the ice and isolates the layers below.

Time series of radiation, air temperature, wind speed, and precipitation are needed on a daily basis to derive freezing and thawing degree days or to derive an analytical solution of the Stefan algorithm. This would enable simulation of freezing and thawing fronts within lake and soil throughout a year. More precise predictions of talik depth and lake growth could be made. Since the TAPAS model is executed once per year, the implementation of an energy balance needs considerable effort. Throughout one year, melting and freezing periods of different lengths alternate with each other. This results in daily changes of freezing and thawing depths, with large consequences for heat transfer and storage. The stored amount of energy needs to be accumulated throughout one year and dissipated throughout the succeeding year. The problem is, that accumulated heat is returned to the system with a time shift. Somehow, this long term change of the energy state in thermokarst affected areas has to be connected to the sub-daily energy fluxes between atmosphere, surface, and soil. The realization of interaction between components of different time-scales is a larger issue. Therefore, the energy balance was not implemented within the present study.

3.4 Initialisation of the thermokarst model

The initialisation of the TAPAS model starts with empty age classes, which need to be filled with information about ice content, slope, disturbance fraction, and lake fraction. The permafrost is virtually undisturbed, and contains initial distribution of ice masses, without any thermokarst lakes. From physical point of view, thermokarst lakes have always developed as a consequence of permafrost degradation and disturbance of the ground thermal regime. Under constant climate conditions an equilibrium state develops between formation of new lakes, expansion, and drainage resulting in a specific limnicity or lake fraction. The aim is to find an appropriate sample of initial conditions for each age class and grid cell. The entire variety of excess-ice and slope conditions of permafrost covered soils need to be embedded within one of the 42 classes. The inclusion of soil properties works via formation of new lakes. With each disturbance event a fraction of the grid cell is added to the first age class. The slope variability is described as a cumulative function from small to high slope. Every TKL is attributed with a fraction of the slope function, which extends from f_1 to f_2 . The size of the fraction ($dist_{fract} = f_2 - f_1$) is the so-called disturbance fraction and depends on the area of the lake and on grid cell area (Eq. 3.8). Continuously, a part of the distribution function is moved to the thermokarst cycle. With each year steeper terrains are entering the first age class. Therefore, the smallest slope can be found in the highest age classes during the spin-up period. All lakes are shifted from one age class to the following age class and keep their attributed slopes. Things are different for the attributed ice content, because ice is depleted until drainage of the lakes. For drained basins, the ice growth is

modelled with the ice aggregation scheme (Sect. 3.5).

The TAPAS model calculates disturbance fraction for each age class in reverse order from the highest to the lowest age class. Continuously permafrost covered parts of the cumulative distribution function are moved to the modelled thermokarst cycle. In this study, permafrost is assumed to extent more likely in steeper parts of the grid cell than in flatter parts, as explained in section 3.2.2. Therefore, permafrost extends from $1 - PF_{old}$ to 1. During the spin up period, the permafrost fraction is kept constant (PF_{old}). The position of the disturbance fraction of the new lake ($dist_{fract}(age = 1)$) with lower end $f1$ and upper end $f2$ is dependent on the sum of $dist_{fract}$ over all upper age classes and the PF (Eq. 3.49 and 3.50). The average slope and ice content can be computed after determination of the fraction parameters $f1$ and $f2$.

$$f1 = (1 - PF_{old}) + \sum_{age=2}^{42} dist_{fract}(age) \quad (3.49)$$

$$f2 = (1 - PF_{old}) + \sum_{age=2}^{42} dist_{fract}(age) + dist_{fract}(1) \quad (3.50)$$

If one lake is expanding, it occupies a new fraction of the grid cell ($dist_{exp}$). The fraction parameters are calculated similar to the disturbance fraction of new lakes. Here, the disturbed area extents from $f1$, which is the sum over all age classes, to $f2$, which is $f1$ plus the disturbance fraction due to lake expansion (Eq. 3.51 and 3.52). Continuously, upper parts of the cumulative functions are attributed to the age class, i.e. lakes are expanding into steeper terrain with less amount of excess-ice. Therefore, the slope within one age class becomes steeper until the end of the spin up period.

$$f1 = (1 - PF_{old}) + \sum_{age=1}^{42} dist_{fract}(age) \quad (3.51)$$

$$f2 = (1 - PF_{old}) + \sum_{age=1}^{42} dist_{fract}(age) + dist_{exp} \quad (3.52)$$

The occupation of new grid cell fractions continues until the entire permafrost area has been disturbed for at least one time. The ice depth is modelled for the whole permafrost area. From then on, new triggered lakes are attributed with slope and ice depth of the oldest basins. The distribution functions are obsolete, because the fractions of all age classes together span the entire permafrost area. Each age class could be associated with a specific slope and ice value. Only if permafrost is expanding, then the slope distribution function comes into play again. The slopes of the drained basin classes are a kind of weighted average over all lake classes due to drainage and keeping the information about slope. Only changing permafrost can add slopes beyond the average of the permafrost area into the system again. Whenever permafrost is expanding towards terrain with smaller slope, the average slope of the new permafrost area is calculated. The slope function is integrated from old PF ($f2 = 1 - PF_{old}$) to new PF ($f1 = 1 - PF_{new}$). The computing procedure mainly follows Eq. 3.55 - 3.56 in sect. 3.4.1.

3.4.1 Slope distribution

The surface of a permafrost grid cell can be very heterogeneous. Steep terrain with low ice content alternates with flat plains underlain with large masses of excess-ice. The variability can be described with distribution functions for slope and ice. As described in sections 3.3.4 and 3.2.1, slope is severely influencing the formation of lakes and excess-ice. Therefore, a part of the grid cells will not be sensitive to thermokarst. Basically, the slope ranges between "minimal" (s_{minmod}) and "maximal" (s_{max}) subgrid slope. A subgrid slope calculation function has been developed to estimate the average slope of a certain grid cell fraction in dependence of the slope distribution parameter b (Stacke and Hagemann, 2012). The driving parameters have been derived from the GTOPO30 data set with elevations on a regularly spaced grid of 30-arc seconds (about 1 km) (Gesch et al., 1999). The slope of one grid point was calculated from the elevations of the highest and the lowest neighbouring grid cell and the distance between them (Stacke and Hagemann, 2012). It is possible to describe the spatial variability of slope as a cumulative function of subgrid slope frequency. Stacke and Hagemann (2012) derived the slope distribution function based on a power law function used by Hagemann and Gates (2003) for the statistical distribution of soil water capacities within grid cells. The slope ($s(f)$) is a cumulative function of grid cell fraction f , where b is the shape parameter of the power law. Hagemann and Gates (2003) improved the original function with two additional parameters (Eq. 3.56) to support the precision of the cumulative distribution curve.

$$s(f) = (1 - (1 - f))^{1/b} * (s_{max} - s_{minmod}) + s_{minmod} \quad (3.53)$$

The slope can be larger than zero at any grid cell fraction and increases from the virtual minimum slope (s_{minmod}) up to the maximum slope (s_{max}) at $f = 1$. The function correctly explains slope distribution only for non-zero parts. Often, grid cells are completely flat to a certain part and contain a fraction with zero slope (f_{zero}). In these parts, the cumulative slope distribution function becomes negative. Therefore, the slope is computed with Eq. 3.53 only for fractions above f_{zero} . Below that threshold, the slope is set to zero.

$$slope_{ave} = \int_{f1}^{f2} s(f) df \quad (3.54)$$

$$f_{zero} = 1 - \left(\frac{s_{minmod}}{s_{max} - s_{minmod}} + 1 \right)^b \quad (3.55)$$

$$slope_{func} = s_{max} + \frac{(s_{max} - s_{minmod}) * b}{b + 1} * \frac{(1 - f2)^{\frac{b+1}{b}} - (1 - f1)^{\frac{b+1}{b}}}{f2 - f1} \quad (3.56)$$

$$s_{off} = s_{max} + \frac{(s_{max} - s_{minmod}) * b}{b + 1} * \frac{(1 - f_{zero})^{\frac{b+1}{b}} - (1 - f1)^{\frac{b+1}{b}}}{f_{zero} - f1} \quad (3.57)$$

$$slope_{ave} = slope_{func} - s_{off} \quad (3.58)$$

Each thermokarst affected area occupies a certain fraction of the grid box ($dist_{fract}$) and expands from a lower end ($f1$) to an upper end ($f2$) of the cumulative slope distribution function ($s(f)$). The preliminary average slope ($slope_{func}$) of $dist_{fract}$ can be derived via integrating the slope function from $f1$ to $f2$ (Eq. 3.54). But, the result probably contains a negative offset, if the

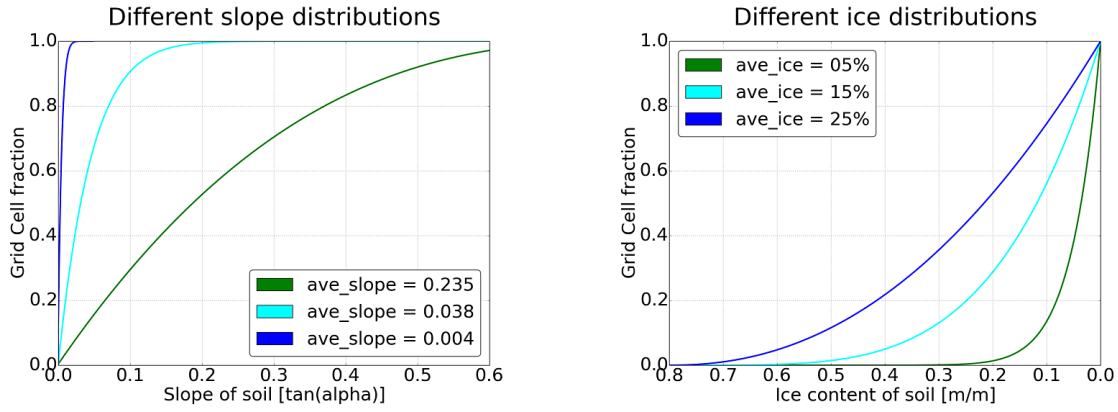


Figure 3.13: Distribution of slope is plotted for three different grid cells from flat to steep (Stacke and Hagemann, 2012) on the left panel. The right panel shows the ice content distribution functions for three average ice contents.

zero-slope fraction is settled within the disturbance fraction. The zero slope fraction can be calculated by transforming Eq. 3.53 to Eq. 3.55. The slope is zero below f_{zero} , because $s(f)$ becomes negative here. Thus, the offset is calculated via integrating $s(f)$ between the lower end of the disturbance fraction (f_1) and f_{zero} (Eq. 3.57). Then, the final average slope (s_{ave}) is determined via subtracting the offset from the preliminary average slope (Eq. 3.58).

The mechanisms will be examined via two examples to support understanding of the equations above. For instance, one grid cell (10.25E, 44.75N) with a mean slope of 0.0403 is completely undisturbed. Now an extraordinary number of new lakes are forming and together disrupting 20 % of the grid cell. In this case, f_1 and f_2 are 0.00 and 0.20, respectively. The zero slope fraction (f_{zero}) measures 0.1469 and is settled between the lower and upper end of the disturbance fraction. Now, the preliminary average slope is computed, for this part. Integrating from f_1 to f_2 results in $slope_{func}$ equal -0.0035 (Eq. 3.58). This value is too small and even negative because a large offset is embedded within the value. Thus, the offset (s_{off}) is calculated, via integrating equation 3.53 from the lower end of the disturbance fraction (f_1) to the zero slope fraction (f_{zero}) (Eq. 3.57). The resulting offset, which is -0.0055 in this case, is subtracted from $slope_{func}$ (Eq. 3.58) to gain the correct average slope ($slope_{ave}$), which is 0.0020 in this case.

Let us consider a second grid cell (152.25W, 61.25N) with a mean slope of 0.235. The cumulative slope distribution of this grid cell can be investigated in figure 3.13. For instance, 40 % of the grid cell is already affected by thermokarst and part of one of the 42 age classes. Now, further 20 % of it is disrupted by a huge disturbance event. There follows, that f_1 and f_2 are 0.4 and 0.6, respectively. The zero slope fraction of this grid cell measures 0.0036. Since this value is much smaller than the lower end of the disturbance fraction, the offset equals to zero. Therefore, s_{off} is zero and s_{func} equals s_{ave} . Integrating equation 3.53 from 0.4 to 0.6 (Eq. 3.54) gives an average slope for the disturbance fraction of 0.188, which can be validated in figure 3.13.

3.4.2 Excess-ice distribution

Contrary to the slope distribution function, which is used for the entire model run-time for changing PF, the use of the ice distribution function is limited on the spin-up time. Therefore, the precision is not the prime issue. Only a rough distribution will be estimated. Depending on texture, soils can store different amount of excess-ice. The ice content can locally range up to 80 % in flat peatlands with a thick organic layer (L. Kutzbach, 2013, pers. comm.). Continuous cryosuction leads to development of excess-ice. Frozen water attracts water and leads to formation of ice lenses. The amount of excess-ice is assumed to be exponentially distributed within one grid box. The highest subgrid ice contents are set at the lower end of the permafrost covered grid box ($f = 1 - PF$), which is also attributed to regions of smaller slope, as it is visible in figure 3.13. A high correlation exists between slope and ice content (Sect. 3.3.4). The maximum ice content (ice_{max}) is actually 0.80, which represents an ice-wedge of about 8 m depth. The ice content is defined as a function of grid cell fraction f ($ice(f)$) and decreases from ice_{max} at $f = 0.0$ to zero at $f = 1.0$, if PF is one (Eq. 3.59).

$$ice(f) = ice_{max} * (1 - f^b) \quad (3.59)$$

$$b = \frac{ice_{max}}{ice_{max} - ice_{ave}} - 1 \quad (3.60)$$

The coefficient b regulates the shape of the curve and depends on the average ice content of the grid box (ice_{ave}), as it is listed in table 3.4. Ice properties on global scale have been provided on a resolution of 0.25° by NSIDC (Brown et al., 1998). For model applications, the data were calculated on 0.5° grid as the median of data points, which are falling into one grid cell. The data information is very sparse and distinguishes only between ice-rich soils with segregated ice content of larger than 20 %, ice-poor sediments with less than 10 % ice and a medium state with an ice content of between 10 % and 20 % (see table 3.4 and figure 3.11). Since the data are provided in form of three classes with no discrete values, an artificial average has to be defined. These averages (ice_{ave}) have been used for determining the coefficient b (Eq. 3.60) via integration of eqn 3.59 over the total grid cell.

$$ice_{cont} = \int_{f1}^{f2} ice(f) df \quad (3.61)$$

$$ice_{cont} = ice_{max} * \frac{1 - \frac{1}{b+1} * (f2^{b+1} - f1^{b+1})}{f2 - f1} \quad (3.62)$$

Similar to the average slope, the average ice content is determined via integrating the ice distribution function from the lower end ($f1$) to the upper end ($f2$) of the disturbed area fraction (Eq. 3.61 - 3.62). New disturbed area fractions are usually attributed to the lowest undisturbed fraction of the grid cell. The fraction parameters are derived via summing over $dist_{fract}$ of all age classes (Eq. 3.49 - 3.50).

4 Tuning the dynamic thermokarst module

This chapter is used to describe the tuning process of model parameters and the sensitivity of the TAPAS model to different parameter settings. The parameters are divided in two categories: soil parameters related to soil processes and climate parameters to climate sensitivity. An initial collection of parameters is set as described in section 3.3. The parameter setting is improved until the model results provide the best fit to today's distribution of observed lake fraction (LF) from ESACCI and ice content (IC) from NSIDC (Brown et al., 1998). The sensitivity study consists of six steps. Each step provides a new sample of parameters, which is named 'Ref-#':

- In the first step, the model is evaluated against different initial area of new ponds, drainage amplification, and drainage probability values. Ref-1 parameter setting will be derived in section 4.1.2.
- In the second step, the model is evaluated with Ref-1 setting against different ice aggregation time-scales and ice formation thresholds. Then, different expansion rates are evaluated with the best ice formation parameters. Ref-2 parameter setting will be derived in sections 4.2.1 and 4.2.2.
- In the third step, the model is evaluated with Ref-2 setting against different drainage probabilities of lakes with an age of 100 years and 1000 years. Ref-3 parameter setting will be derived in section 4.2.3.
- In the fourth step, the model is evaluated with Ref-3 setting against different disturbance formation thresholds and sensitivities to fire disturbances. Ref-4 parameter setting will be derived in sections 4.3.1 - 4.3.4.
- In the fifth step, the model is evaluated with Ref-4 setting against different sensitivities to disturbance events. Additionally, the model sensitivity to climate change is increased. Finally, different drainage amplifications and pore-size influences are investigated again. Ref-5 parameter setting will be derived in sections 4.3.5 - 4.3.7 and 4.4.1.
- In the sixth step the model is evaluated with Ref-5 setting against different initial lake area, time aggregation time-scale, expansion rates, and drainage probabilities again. The final parameter setting will be derived in sections 4.4.2 and 4.4.3

Like in chapter 3, the TAPAS model is driven by data from the CLIMBA Holocene run from Bruecher et al. (2014) over a period of the past 7000 years. CLIMBA is a coupled climate-carbon model, which combines CLIMBER-2 with JSBACH (Bruecher et al., 2014). Further descriptions

can be found in section 6.2. It provides time-series of several climate variables on monthly time-scale and on a resolution of 3.75° (T31-grid). Soil temperature is important for determining active layer depth (ALD) and the maximum ice depth. 2-meter air temperature (T2M), snow-water-equivalent (SWE) depth, and accumulated burned area fraction are applied to compute temperature, snow, and fire disturbances, respectively. Precipitation, snow-melt, runoff, and drainage are used to determine infiltration disturbances. Additionally, 30-year running means and 30-year running standard deviations are determined by T2M, SWE depth, and infiltration. Temperature is again used to drive the permafrost fraction (PF).

Since slope and pore-size data are available on 0.5° grid, the TAPAS model can run at this scale, although the climate forcing data are provided on T31 grid. Slope and pore-size are used to limit formation of thermokarst lakes (TKL) and accumulation of excess-ice (as described in sections 3.2.1 and 3.3.5). The forcing data are remapped on 0.5° with the nearest neighbour method. This method was chosen for two reasons: first the standard deviation, which is needed to determine the number of disturbances, cannot be downscaled with, e.g., conservative or bilinear remapping. Second, preparation of all input data including computation of μ and σ for disturbance calculation on T31 grid takes two week of computational time. Therefore, preparation of all input data on 0.5° grid would need too many resources.

This study is focused on grid cells with $PF \geq 0.1$. Evaluation with observed LF becomes more difficult in regions with less permafrost, because non-permafrost lakes may dominate the observed LF in these grid cells. Note that the TAPAS model is limited by the permafrost extent, which is computed with long-term mean T2M from CLIMBA. Therefore, the boundaries of the model domain are defined by the same grid-scale as CLIMBA.

4.1 Reference thermokarst model run driven by CLIMBA

4.1.1 Overview of the model parameters and initial setting

The very first model run is carried out with the initial set of parameters, as described in section 3.3. The parameters are based on literature research and several test runs during the model development. This section is used to provide a short overview of the different model parameters. In total, there are 25 parameters available for evaluation. They are separated in 2 categories, which are soil parameters and climate parameters. The division relates to different climate and soil dependent processes.

The soil parameters consist of 12 parameters, which limit expansion rate, drainage probability, ice accumulation, and the initial size of new ponds. Thermokarst starts with the formation of new ponds with different shapes and areas. For the model, an initial global mean area is assumed for new ponds (A_0). They are circular shaped and expand due to thermal and mechanical effects (see sect. 3.3.3). The expansion rate increases in three steps from *expand1* to *expand4*. The expansion rate depends on the area of one lake and increases after different size thresholds are passed (as explained in Sect. 3.3.3). The drainage probability increases with the size of one lake as observed by Jones et al. (2011) and discussed in section 3.3.4. Since the area of one lake directly depends on its age, drainage probability is computed as a function of time (see Eq. 3.40).

The coefficients of the drainage probability function are computed with three parameters. These are drainage probabilities of 100-year old lakes ($drain_{100}$) and of 1000-year old lakes ($drain_{1000}$) and also the drainage amplification ($drain_{ampl}$) due to decreasing permafrost fraction. Drainage increases by $drain_{ampl}$ times if PF reduces from 100 % to 10 %. If PF decreases to 0 %, then drainage probability increases to 100 %. Excess-ice in drained basins accumulates as a function of ice deficit, which decreases exponentially with time-scale τ (see Eq. 3.44 - 3.45 in Sect. 3.3.5). The higher τ is set, the more time is needed to reach the maximum ice depth and the lower is the ice content after 1000 years. The TAPAS model can also distinguish between different forms of massive ice bodies the temperature thresholds are defined to distinguish between different processes of ice formation. Between the upper ($thres_{ice1}$) and medium ($thres_{ice2}$) threshold, excess-ice mainly aggregates in form of palsas, which develop due to cryosuction, which in turn is limited by the pore-size of the permafrost soil (Eq. 3.46). Between the medium and lower threshold ($thres_{ice3}$), excess-ice mainly aggregates in thermal contraction cracks, that are filled with melting water, which in turn freezes to ice wedges. Within $thres_{ice2}$ and $thres_{ice3}$, ice aggregation is not pore-size dependent (Eq. 3.44).

The climate parameters consist of 13 members, which regulate number of disturbance events and triggered TKL (as described in Sect. 3.3.1). The yearly number of triggered TKL is the sum of four different types of disturbances. The number of disturbances from summer T2M, winter SWE, infiltration, and burned area fraction is computed with equations 3.24, 3.26, 3.28, and 3.25, respectively; as described in section 3.3.1. The parameters for temperature and snow disturbances $a_{stemp|wsnow}$ and $b_{stemp|wsnow}$ have been set to 1 and 3, respectively. I assume, that the number of triggered thermokarst events is increasing exponentially with the number of standard deviations above the mean (see Sect. 3.3.1). For infiltration, which is used as a proxy for flood events, the parameters a_{infil} and b_{infil} are both set to 1, because flood events of any size can enhance erosion processes and trigger thermokarst. Floods can occur between May ($m1_{infil}$) and August ($m2_{infil}$), in the Arctic. Infiltration disturbances are separately computed for each month of the period $m1_{infil}$ and $m2_{infil}$ and accumulated to a yearly sum. The number of fire disturbances is computed as a linear function of annual burned area fraction with gradient k_{burn} . A linear response is assumed, because the effect of burnt vegetation on the soil heat balance is the same everywhere.

Four important thresholds have been introduced to exclude very cold regions and very arid regions. Infiltration disturbances are triggered monthly from May to August if monthly infiltration exceeds 10 mm ($thres_{infil}$). Summer temperature events are triggered, if the average temperature between June and August exceeds 0 °C ($thres_{stemp}$). Winter snow depth disturbances are triggered, if the average SWE depth between November and March exceeds 30 mm ($thres_{wsnow}$). The parameter $thres_{surf}$ regulates developments of lakes up to an age of 10 years.

The following list (Table 4.1), shows the model parameters and their assigned values before starting the tuning procedure (initial set-up) and after finishing the sensitivity studies (final set-up).

Parameter	Description	Initial	Final
a_{stemp} [-]	Factor of summer T2M disturbance (Eq. 3.24)	1.0	0.106
b_{stemp} [-]	Exponent of summer T2M disturbance (Eq. 3.24)	3.0	6.0
$thres_{stemp}$ [°C]	Threshold for $dist_{stemp}$ (Sect. 3.3.1)	0.0	0.0
a_{wsnow} [-]	Factor of winter SWE disturbance (Eq. 3.26)	1.0	0.212
b_{wsnow} [-]	Exponent of winter SWE disturbance (Eq. 3.26)	3.0	6.0
$thres_{wsnow}$ [mm]	Threshold for $dist_{wsnow}$ (Sect. 3.3.1)	30	100
a_{infil} [-]	Factor of infiltration disturbance (Eq. 3.28)	1.0	4.0
b_{infil} [-]	Exponent of infiltration disturbance (Eq. 3.28)	1.0	1.0
mon_{infil1}	First month with infiltration dist. (Sect. 3.3.1)	May	May
mon_{infil2}	Last month with infiltration dist. (Sect. 3.3.1)	Aug	May
$thres_{infil}$ [mm]	Threshold for $dist_{infil}$ (Sect. 3.3.1)	10	30
k_{burn} [(A/A) ⁻¹]	Factor of fire disturbance (Eq. 3.25)	20000	x
$thres_{surf}$ [-]	Surface-runoff blocking TKL (Sect. 3.3.1)	-2.0	x
A_0 [m ²]	Initial area of new ponds (Sect. 3.3.3)	1	100
$expand1$ [m/y]	Expansion rate of lakes < 1 ha (Sect. 3.3.3)	0.20	0.10
$expand2$ [m/y]	Expansion rate of lakes > 1 ha (Sect. 3.3.3)	0.25	0.20
$expand3$ [m/y]	Expansion rate of lakes > 10 ha (Sect. 3.3.3)	0.25	0.40
$expand4$ [m/y]	Expansion rate of lakes > 40 ha (Sect. 3.3.3)	0.30	0.60
$drain_{100}$ [n/n]	Drainage prob. after 100 years (Sect. 3.3.4)	0.0018	0.0031
$drain_{1000}$ [n/n]	Drainage prob. after 1000 years (Sect. 3.3.4)	0.0024	0.0023
$drain_{ampl}$ [-]	Amplification of drainage prob. (Sect. 3.3.4)	2.0	1.2
τ [y]	time-scale of ice accumulation (Eq. 3.44)	1500	2000
$thres_{ice1}$ [°C]	Upper threshold of ice formation (Sect. 3.3.5)	-1.0	-1.0
$thres_{ice2}$ [°C]	Threshold of pore-size limitation (Sect. 3.3.5)	-4.0	x
$thres_{ice3}$ [°C]	Lower threshold of ice formation (Sect. 3.3.5)	-16.0	x

Table 4.1: Parameter list of the TAPAS model showing variable, description, initial setting as described in chapter 3, and the final setting (from left to right, respectively). Final settings marked as 'x' indicate, that the parameter is obsolete and not used any more.

4.1.2 Improvement of initial parameter settings

Here, the initial setting of model parameters (Table 4.1) is discussed and improved. Four changes are carried out on the initial parameter setting for the first reference run (Ref-1). Parameter setting of Ref-1 is listed in table 4.2.

The first improvement relates to drainage amplification. It is observed that drainage probability increases if PF decreases (Smith et al., 2005). The parameter $drain_{ampl}$ is initially set to 2.0. This means, that drainage probability of lakes increases by 100,%, if PF reduces from 1.0 to 0.1. This value is too high, because LF becomes too small in sporadic permafrost regions. Too many lakes are draining. Therefore, this parameter is set to 1.5. Smaller values are not possible at this point, because LF becomes larger than PF in some regions with sporadic permafrost. $drain_{ampl}$ does not play a significant role on the pan-Arctic distributions of LF and IC because drainage is amplified exponentially, see equation 3.40 and most regions are underlain with continuous and discontinuous permafrost.

Parameter	Ref-1	Ref-2	Ref-3	Ref-4	Ref-5	Final
a_{temp} [-]	1.0	1.0	1.0	1.0	0.106	0.106
b_{temp} [-]	3.0	3.0	3.0	3.0	6.0	6.0
$thres_{temp}$ [°C]	0.0	0.0	0.0	0.0	0.0	0.0
a_{snow} [-]	1.0	1.0	1.0	1.0	0.212	0.212
b_{snow} [-]	3.0	3.0	3.0	3.0	6.0	6.0
$thres_{snow}$ [mm]	30	30	30	100	100	100
a_{infil} [-]	1.0	1.0	1.0	4.0	4.0	4.0
b_{infil} [-]	1.0	1.0	1.0	1.0	1.0	1.0
mon_{infil1}	May	May	May	May	May	May
mon_{infil2}	Aug	Aug	Aug	May	May	May
$thres_{infil}$ [mm]	10	10	10	30	30	30
k_{burn} [(A/A) ⁻¹]	20000	20000	20000	x	x	x
$thres_{surf}$ [-]	-2.0	-2.0	-2.0	x	x	x
A_0 [m ²]	100	100	100	100	100	100
$expand1$ [m/y]	0.20	0.10	0.10	0.10	0.10	0.10
$expand2$ [m/y]	0.25	0.20	0.20	0.20	0.20	0.20
$expand3$ [m/y]	0.25	0.40	0.40	0.40	0.40	0.40
$expand4$ [m/y]	0.30	0.60	0.60	0.60	0.60	0.60
$drain_{100}$ [n/n]	0.0024	0.0027	0.0039	0.0039	0.0039	0.0031
$drain_{1000}$ [n/n]	0.0028	0.0027	0.0022	0.0022	0.0022	0.0023
$drain_{ampl}$ [-]	1.5	1.5	1.5	1.5	1.2	1.2
τ [y]	1500	2000	2000	2000	2000	2000
$thres_{ice1}$ [°C]	-1.0	-1.0	-1.0	-1.0	-1.0	-1.0
$thres_{ice2}$ [°C]	-4.0	-6.0	-6.0	-6.0	x	x
$thres_{ice3}$ [°C]	-16.0	-16.0	-16.0	-16.0	x	x

Table 4.2: This table shows the parameters of the TAPAS model during different stages of the sensitivity study from left to right, respectively. Final settings marked as 'x' indicate, that the parameter is obsolete and not used any more.

The second improvement is related to initial area of new ponds. It is initially set to 1 m². A_0 is increased to 100 m², because the modelled LF shows a higher correlation to changes in summer temperature and winter snow depth. Moreover, water bodies with an area of 100 m² are more likely to become a landscape forming phenomenon than smaller ones, which is typical for thermokarst, because smaller ponds disappear easier than larger ones due to growing vegetation and evaporation (E-M. Pfeiffer, 2015, pers. comm.).

LF increases in order of 0.005 m²/m² if A_0 is changed from 1 m² to 100 m², because lakes of all age classes become larger then. If A_0 is set to 1 m², then it takes about 30 years to reach an area of 100 m². This means, that one triggered TKL occupies a certain fraction of the grid cell 30 years earlier, if A_0 is set to 100 m².

In reality some ponds start with 1 m², but they usually merge together with adjacent ponds to one large thermokarst lake. Therefore, several ponds can be counted together as a larger one. There was no effect of changing A_0 visible on lake and ice distribution up to an area of 10 m². Little improvements are visible for an initial area of 1000 m². The number of grid cells with an

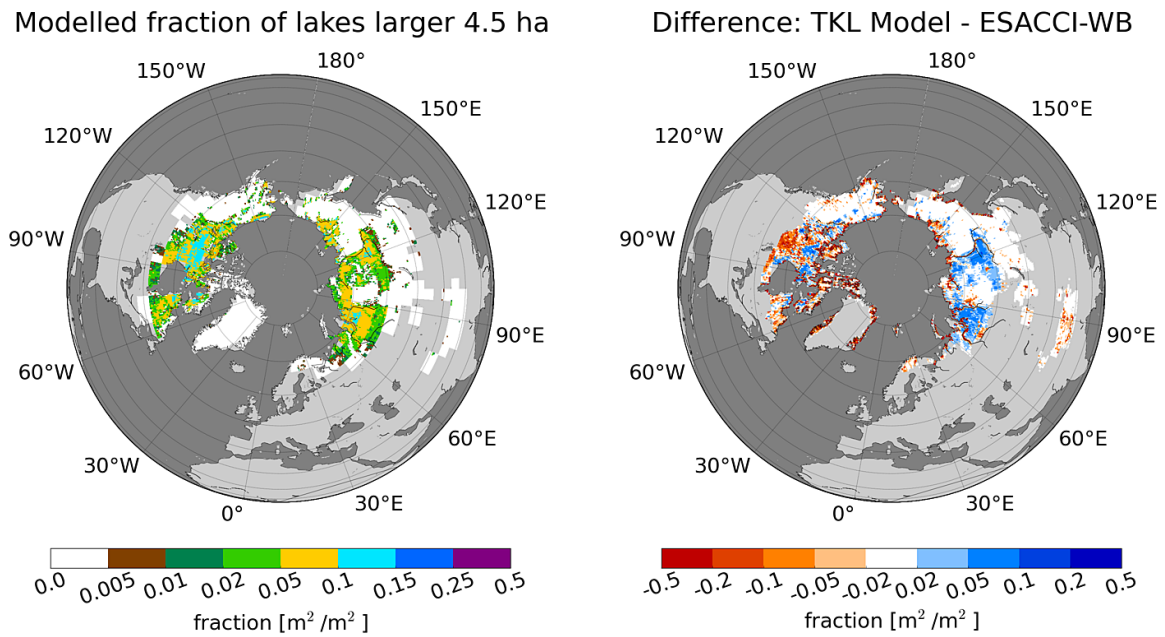


Figure 4.1: This figure shows the fraction of grid cell covered with TKL larger than 0.5 ha after the reference-1 model run. Left panel shows the absolute value and the right one the difference from ESACCI WB.

ice content of larger 20 % with unit m/m decreases.

The higher initial area leads to very high lake fraction in lowland regions, where a high number of lakes is evolving. This problem is solved by reducing the number of TKL, which can be done in two ways. Either less TKL are triggered or more lakes drain. The drainage probabilities after 100 and 1000 years, respectively, are set at lower values than suggested by observations from Jones et al. (2011) (see Table 3.3 in Sect. 3.3.4). For lakes with areas of up to 10 ha, drainage probability measures about 0.0030. For lakes with areas of larger 40 ha, it measures about 0.0060. With the initial parameter settings, the areas of 10 ha and of 40 ha are reached by TKL with an age 750 years and 1500 years, respectively. Lakes with an age of 1000 years cover an area of about 18 ha. Tests with $drain_{1000} = 0.0060$, resulted in a complete loss of very large lakes and too little LF. Maybe the field site study, as described in section 3.3.4, is not representative for all tundra regions. Therefore, the drainage probabilities of lakes with an age of 100 years and 1000 years, are set to 0.0024 and 0.0028, respectively. These values fit the drainage probability of lakes smaller than 10 ha (Table 3.3). The most lakes within the model are younger than 800 years.

4.1.3 Results from the Ref-1 model run

Altered initial area and drainage parameters are used for the Ref-1 model run. The main results of the Ref-1 model run are discussed here. Note, that all model runs are started with a restart file. The aim is to reduce the spin-up period of the TAPAS model. For the restart file, the

100 year period 6970 - 6870 BP from CLIMBA has been used. Forcing data of this period are cyclically repeated until an equilibrium state is reached. 30-year running means are applied for the derivation of disturbance events. As a result, the model is started at the 30th time-step.

The lake fraction (Fig. 4.1) reaches the highest values in Central Canada, around the Great Slave lake, at the Mackenzie river, North Slope of Alaska, Laptev Sea coast, southern Lena river, Lena Delta, and northern Siberian plains. The Seward Peninsula suffers from availability of input data and cannot be judged. In general, the western Siberian lowlands have a too high LF, as well as regions in Central Siberia west of Lena river, and in northern part of central Canada. On the other side the southern Central Canadian regions show too little lake fraction, which is also the case for southern Alaska, southern edge of the western Siberian plains, Tibet, and Laptev Sea Coast (Fig. 4.1).

Modelled average ice content, present

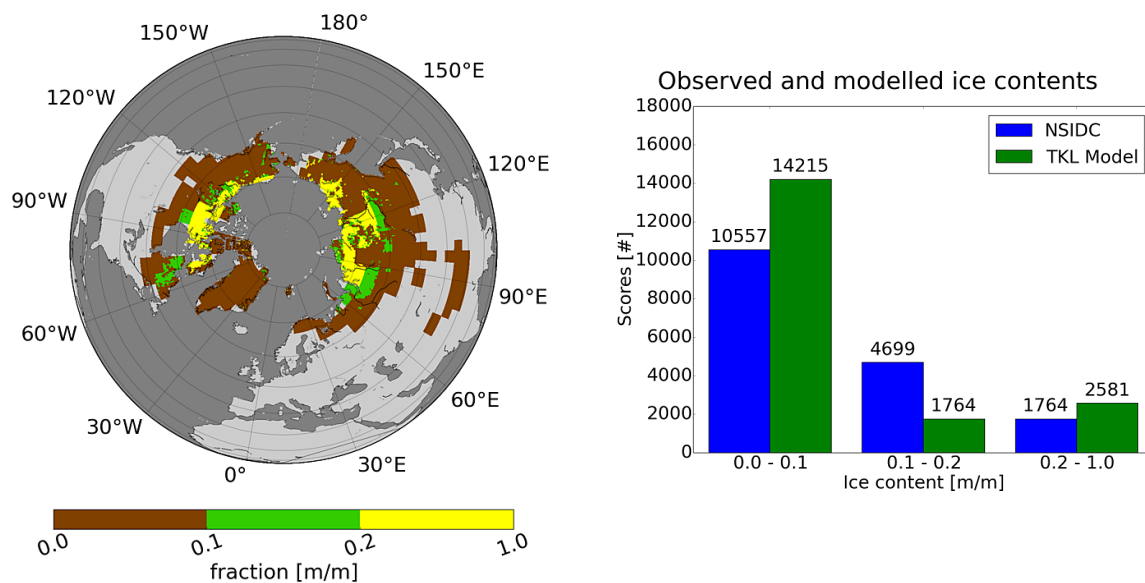


Figure 4.2: This figure shows the modelled ice contents according the NSIDC ice content classes (Brown et al., 1998) from low over middle to high (left panel) and a comparison of the absolute frequency of modelled and observed ice content (right panel).

The modelled IC values are distributed over a higher range of values than it is shown in figure 4.2. For evaluation, they are sorted analogous to the NSIDC ice content classes (Brown et al., 1998), which are listed in table 3.4. As it is visible in figure 4.2, the model overestimates the number of grid cells with high IC (> 20 % with unit m/m) by 56 %. This is due to the central Canadian lowlands. Especially west of the Hudson Bay, the soil mainly consists of barren ground, whereat NSIDC shows low IC (< 10 %). Also in central and northern Siberia, the model shows more regions with high IC. See figure 4.9 for comparing distributions of IC as modelled with Ref-1 and provided by NSIDC. The medium IC class is highly under-represented. The modelled frequency is by about 60 % smaller than the observed one. Especially in Eastern Siberia and in Tibet, large regions exist with medium IC, where the model cannot represent the ice content well. The TAPAS model runs at a 0.5° grid. Probably, this resolution is still too coarse to represent most valleys, which provide flat terrain for excess-ice accumulation. The sensitivity study is

focused on regions with PF of larger than 10 %. Satellite observations provide measurements of total lake fraction, which is a mixture of TKL and other forms of lakes. The signal becomes ambiguous in regions with PF of less than 10 %. Lakes are not homogeneously distributed over thawed and frozen areas, while permafrost areas provide a larger fraction of lakes, as described in section 2.3 and discussed by Grosse et al. (2013). Therefore, a simple multiplication of the observed LF with PF would not give the correct lake fraction of one grid cell.

Actually figure 4.2 shows low IC in Greenland. Large parts of the island are covered by glaciers. In the southernmost part, where no glaciers are present, the slope is too large for ice accumulation. In the glaciated parts infiltration is too small and no water is available for ice accumulation.

4.2 Sensitivity to soil parameters

In this section the TAPAS model is tuned and evaluated against observations from NSIDC (ice content, IC) and ESACCI WB (lake fraction, LF). The ice parameters ice aggregation time-scale and ice formation thresholds are altered in respect to Ref-1 parameter setting, to improve distribution and frequency of observed excess-ice contents. Then, different expansion rates are tested together with the improved ice formation parameters. Afterwards, a new reference parameter setting (Ref-2) is defined with improved ice parameters and expansion rates. Afterwards, the sensitivity to different drainage probability parameters is discussed. Ref-3 is the result of tuning soil parameters and includes improved drainages parameters, as listed in table 4.2.

For the soil parameters, I used two evaluation tools for evaluating modelled LF and IC with observations in periglacial environments. Firstly, a cumulative distribution function (CDF) of LF is established to compare relative frequencies of certain lake fractions. Grid cells with IC of less than 10 % or with PF of less than 10 % are masked out to increase the probability to compare thermokarst lakes only. Masks are set according to the NSIDC distributions of excess-ice and permafrost. LF is ordered in $0.01 \text{ m}^2/\text{m}^2$ intervals from low to high. ESACCI, shows that 25 % of all grid cells with medium or high IC show a LF of smaller than 0.01, 50 % smaller than 0.035, and 80 % smaller than 0.135, respectively. Note, that these numbers have to be considered carefully: ESACCI interpolates ENVISAT based observation data of water bodies with a resolution of 300 m on 0.5° grid (Santoro et al., submitted). Probably, some ocean areas are included within the provided LF data-set. A land-sea mask is applied, but nevertheless there are many grid cells at the coast lines and along rivers, which show a LF of up to 0.49 (see Fig. 2.5). It is possible, that still many areas with ocean water are inherited within the data. Thus, the modelled LF is compared with LF data, which consist of thermokarst lakes but also of glacier lakes, ocean water, and rivers.

Secondarily, modelled and observed IC are evaluated via histograms of the absolute number of grid cells with a certain IC. Three bins are defined, according to NSIDC definition of ice content classes, as listed in table 3.4. The classes are named low IC, medium IC, and high IC, which stands for regions with an ice content of less than 10 %, of between 10 % and 20 %, and of more than 20 %, respectively. About 10600 grid cells contribute to low IC, 4700 to medium IC, and 1800 to high IC. As visible in figure 3.11, regions with high IC can be found in eastern Siberian lowlands, Alaska north slope, Mackenzie delta, parts of western Siberian lowlands, and

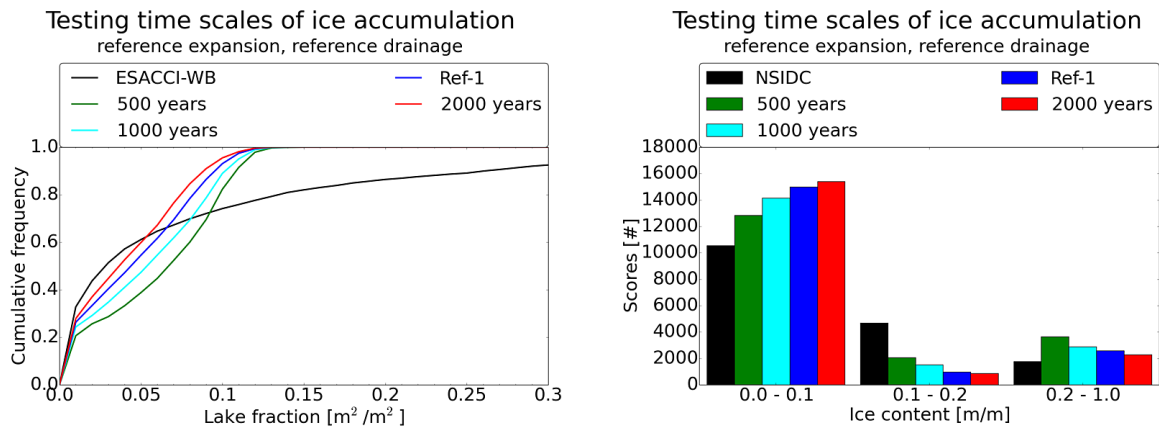


Figure 4.3: The sensitivity of the TAPAS model to different ice accumulation time-scales is tested here. Ref-1 relates to a time-scale of 1500 years. The left figure shows CDF of LF in comparison to observations from ESACCI-WB and the right figure shows absolute frequency of IC in comparison to observations from NSIDC.

around the river Lena. The aim is reach distribution and frequency of observed ice contents.

CDFs and histograms are used to evaluate formation of TKL and aggregation of excess-ice in general. Soil parameters drive accumulation of excess ice and evolution of TKL. The aim is to receive large LF in cold and flat areas and small LF in warm and mountainous areas. The sensitivity to different soil properties is not dependent on geographic location. Therefore, the soil parameters are evaluated against the frequency of LF and IC.

4.2.1 Excess-ice aggregation

Here, the sensitivity to different ice parameters is tested with Ref-1 parameter settings. First, different ice accumulation time-scales (τ) are evaluated. A larger time-scale means, that it takes more time for the model to reach the maximum excess-ice depth. A larger τ reduces the amount of aggregated ice within a certain time period and reduces the ice content. The ice accumulation time-scale τ is altered in 500 year steps from 500 years to 2000 years, while 1500 years is already covered by Ref-1. The aim is to reduce the number of grid cells with high IC and to increase number of grid cells with medium IC. If τ increases, then medium and high IC decrease while low IC increases (see Fig. 4.3). Excess-ice accumulates in drained basins until the surface is disturbed and TKL are triggered. In the TAPAS model, it takes about 1000 - 1400 years from formation of a drained basin until it is affected by thermokarst. If τ is increased, then the ice depth of a basin with an age of, e.g., 1000 years decreases. If τ is set to 500 years, many grid cells reach an ice content of more than 50 %. In reality, this value can be reached locally but not for an area of several 10000 km². $\tau = 2000$ shows the best confirmation with high IC, while medium and low decrease, which results in an overall smaller ice content. As visible in figure 4.3, LF decreases with increasing τ . The area covered by water is proportional to IC, as it is discussed in section 3.2.1. The improvement is larger for smaller LF than for higher LF. The Kolmogorov-Smirnov test shows that all modelled CDFs are significantly different from the

observed CDF. The reason is the high discrepancy of large LF. The modelled CDFs are not significantly different from each other on the 90 % level. A time-scale of 2000 years is chosen, because the number of grid cells with high IC fits best to observations and smaller LF fit better to observations.

Second, a smaller temperature threshold of ice formation is tested. The lower ice aggregation threshold ($thres_{ice3}$) is set to $-18\text{ }^{\circ}\text{C}$. Maybe some high north regions are disregarded by the model. However, the effect on the geographic distribution of IC is small and the CDF shifted towards higher LF. Number of grid cells with high IC increases from 2600 to 2800. The northward extension of regions with high IC better fits to observations with a lower $thres_{ice3}$ of $-16\text{ }^{\circ}\text{C}$ than with $-18\text{ }^{\circ}\text{C}$, respectively. Thus, the lower ice formation thresholds can also be modelled with $-16\text{ }^{\circ}\text{C}$.

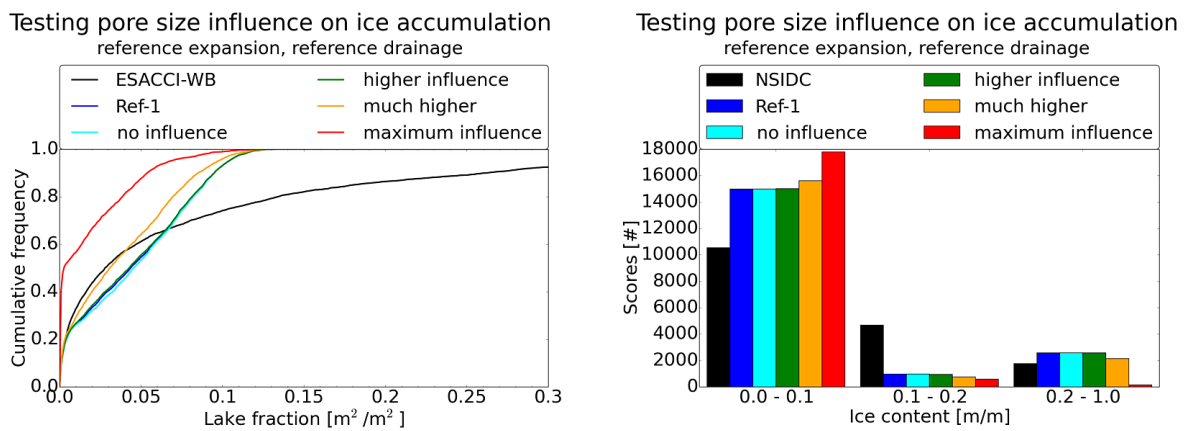


Figure 4.4: The sensitivity of the TAPAS model to different lower thresholds of pore-size influence is tested here. Thus lower and upper ice formation threshold are kept at Ref-1 setting and only the medium threshold is altered (see Table 4.3. The left figure shows CDF of LF in comparison to observations from ESACCI-WB and the right figure shows absolute frequency of IC in comparison to observations from NSIDC.

Scenario	Upper threshold	Medium threshold	Lower threshold
No influence	$-1\text{ }^{\circ}\text{C}$	$-1\text{ }^{\circ}\text{C}$	$-16\text{ }^{\circ}\text{C}$
Reference-1	$-1\text{ }^{\circ}\text{C}$	$-4\text{ }^{\circ}\text{C}$	$-16\text{ }^{\circ}\text{C}$
Higher influence	$-1\text{ }^{\circ}\text{C}$	$-6\text{ }^{\circ}\text{C}$	$-16\text{ }^{\circ}\text{C}$
Much higher influence	$-1\text{ }^{\circ}\text{C}$	$-8\text{ }^{\circ}\text{C}$	$-16\text{ }^{\circ}\text{C}$
Maximum influence	$-1\text{ }^{\circ}\text{C}$	$-16\text{ }^{\circ}\text{C}$	$-16\text{ }^{\circ}\text{C}$

Table 4.3: Following ice formation thresholds are set to test the sensitivity of the model to different pore-size influences. The scenario names in left panel are the same as the legend labels in figure 4.4.

Third, different medium thresholds of ice formation ($thres_{ice2}$) are evaluated against observed LF and IC. As explained in section 3.5, it distinguishes between warmer regions where mainly palsas form and colder regions where mainly ice-wedge polygons form. Palsas develop between

$thres_{ice1}$ and $thres_{ice2}$. Aggregation of excess-ice occurs via cryosuction which is limited by pore size. Polygons develop between $thres_{ice2}$ and $thres_{ice3}$. Ice-wedges form due to infiltration of cracks, which is modelled independent of pore-size.

Five scenarios are performed with different medium ice formation thresholds as listed in table 4.3). Figure 4.4 shows CDF and histogram of the different scenarios in comparison to observations. Almost no changes of LF and IC are visible for medium ice formation thresholds of between $-1\text{ }^{\circ}\text{C}$ and $-6\text{ }^{\circ}\text{C}$. The 2-sample Kolmogorov-Smirnov test suggests that the scenarios with $thres_{ice2}$ equal $-1\text{ }^{\circ}\text{C}$, $-4\text{ }^{\circ}\text{C}$, and $-6\text{ }^{\circ}\text{C}$, respectively, are from the same distribution with a probability of 100 %. There follows, that limiting ice formation via pore-size has no effect on modelled IC and LF in warm permafrost regions.

If the medium threshold is set to $-16\text{ }^{\circ}\text{C}$ as in the scenario 'maximum influence', then IC is computed via ice segregation everywhere (Eq. 3.46). The number of grid cells with an IC of larger 20 % decreases to almost zero while the number of grid cells with LF of smaller 10 % increases (Fig. 4.4).

With a medium threshold of $-8\text{ }^{\circ}\text{C}$ ('much higher influence') the modelled CDF fits to the observed CDF up to a LF of 0.05. IC larger than 20 % reduces slightly as it is desired after the Ref-1 run (see Fig. 4.2). The 2-sample Kolmogorov-Smirnov test shows that all modelled CDFs are significantly different from the observed CDF. For instance, the p-values are $1.1 \cdot 10^{-6}$ and $2.0 \cdot 10^{-9}$, for a medium ice formation threshold of $-6\text{ }^{\circ}\text{C}$ and $-8\text{ }^{\circ}\text{C}$, respectively. The CDFs of $thres_{ice2}$ equal $-1\text{ }^{\circ}\text{C}$, $-4\text{ }^{\circ}\text{C}$, and $-8\text{ }^{\circ}\text{C}$ are not significantly different from the ref-1 run on the 99 % level. The aim of the medium threshold is to distinguish between palsa and polygon formation. With $-8\text{ }^{\circ}\text{C}$, probably too many regions with polygons are modelled as palsas, since polygons develop already in regions colder than $-4\text{ }^{\circ}\text{C}$ (Washburn, 1980). Since a colder medium threshold suggests an improvement for small LF and high IC, a value of $-6\text{ }^{\circ}\text{C}$ is chosen at this step.

4.2.2 Expansion rate

Scenario	smaller 1 ha	smaller 10 ha	smaller 40 ha	larger 40 ha
Reference-1	0.20 m/y	0.25 m/y	0.25 m/y	0.30 m/y
Reference-1 expansion	0.20 m/y	0.25 m/y	0.25 m/y	0.30 m/y
Large lakes fast	0.20 m/y	0.25 m/y	0.30 m/y	0.40 m/y
Small slow and large fast	0.10 m/y	0.20 m/y	0.30 m/y	0.40 m/y
Small slow, large very fast	0.10 m/y	0.20 m/y	0.40 m/y	0.60 m/y

Table 4.4: Following expansion rates are tested during the sensitivity studies. Relative to Ref-1, the drainage probability is set to a constant value (0.0027), τ to 2000 years and the medium threshold to $-6\text{ }^{\circ}\text{C}$ (Ref-1 expansion). The scenario names in left panel are the same as the legend labels in figure 4.5.

Tuning of the expansion rate is carried out with Ref-1 parameter setting, but with improved ice formation parameters as follows: τ equal 2000 y, $thres_{ice1}$ equal $-1\text{ }^{\circ}\text{C}$, $thres_{ice2}$ equal $-6\text{ }^{\circ}\text{C}$, and $thres_{ice3}$ equal $-16\text{ }^{\circ}\text{C}$ (see Sect. 4.2.1). The drainage probability is set to 0.0027 for all lakes. This scenario is labelled as 'Ref-1 expansion' in figure 4.5. In comparison to Ref-1, younger

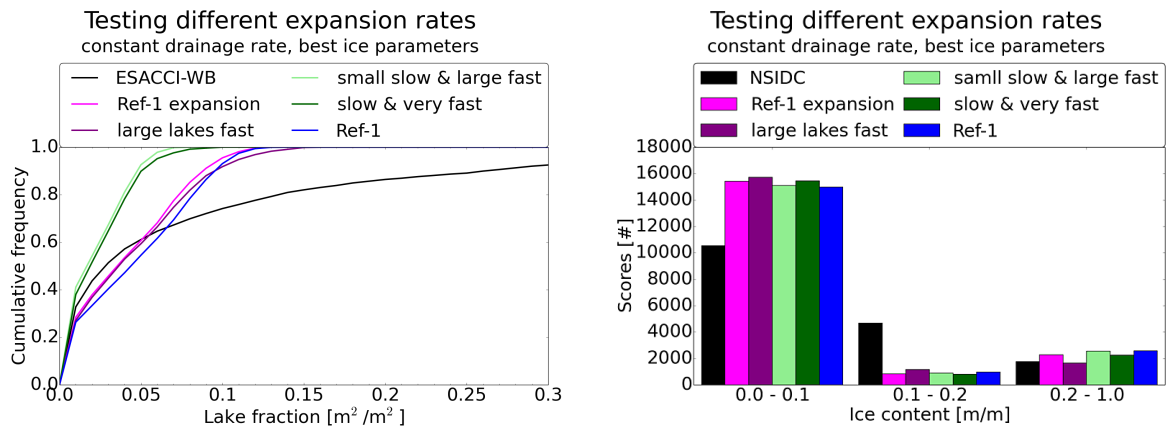


Figure 4.5: This figure shows the sensitivity of the TAPAS model to different expansion rates. 'Ref-1 expansion' is like 'Ref-1', but with improved ice parameters and a constant drainage probability of 0.0027 for all lakes. See table 4.4 for closer details. The left figure shows CDF of LF in comparison to observations from ESACCI-WB and the right figure shows histograms of IC in comparison to observations from NSIDC.

lakes are less stable and drain easier, while older lakes are more stable and, therefore, reach a larger area. Furthermore, the probability to disappear is the same for all lakes independent of size and age.

The effect of constant drainage probability can be followed from comparison between 'Ref-1 expansion' and 'Ref-1' in figure 4.5. Generally, LF becomes smaller due to the higher drainage of earlier lakes and reduces by $0.01 \text{ m}^2/\text{m}^2$. LF of largest lakes decreases by a smaller magnitude, because the drainage probability of large lakes has decreased in comparison to Ref-1.

Two main effects are visible for different expansion rates. If large lakes expand faster, then only the grid cells with larger LF (the upper 20 - 30 %) display higher LF. Those grid cells are located in lowlands with continuous permafrost. Other areas with smaller PF have a higher drainage probability due to $drain_{ampl}$. There, the lakes drain earlier and reach a smaller size. Therefore, LF is not severely influenced by a larger expansion rate of large lakes. Furthermore, lakes in regions with a higher slope expand less within the model. The area ratio (i.e. ratio between lake area and disturbed area as described in section 3.2.1) decreases with the inverse of the lakes diameter (Eq. 3.12). Therefore, the lake area does not increase with the same ratio as the disturbed or thawed area. Thus, lakes are smaller than in flat lowlands, and grid cells with a higher slope have a smaller lake fraction. The drainage probability is independent of slope within the model. The modelled CDF is slightly closer to the observed CDF, if the expansion rate of large lakes is set to higher values than in 'Ref-1 expansion'.

The expansion rate of small lakes has a larger influence on CDF than the expansion rate of large lakes. The shape of the CDF curve changes between the experiments 'Ref-1 expansion' and 'small lakes slow and large lakes fast'. As visible in figure 4.5 the modelled CDF of LF fits to observations for the lower 40 % and follows more or less the shape of the observed curve, but with smaller LF (see Fig. 4.5). The CDFs of the 'small slow and large fast' and 'small slow & large very fast' experiments show steep gradients for small LF, which flattens with higher LF similar to a logarithmic function. The curves of the other experiments are flatter for

small LF. The gradient increases with LF and finally flattens again. If the expansion rate of young lakes is set to slow, then this reduces the sizes of all larger lakes. The influence increases with LF. As described before, a raised expansion rate for large lakes decreases the discrepancy between model and observations for the largest lakes (see experiments 'small slow and large fast' and 'small slow & large very fast' in Fig. 4.5). Again, the Kolmogorov-Smirnov test shows a significant difference between modelled and observed CDF. Also the CDFs from the experiments are significantly different from the 'Ref-1 expansion'-run. Probably the shape of the CDF has improved because in regions with a small PF, lakes drain earlier and do not reach higher age and larger sizes. Therefore, expansion rate of large lakes has a smaller influence on LF, than in regions with high PF. The CDF does not change much for grid cells with smaller LF, if expansion rate of large lakes is increased.

Although the discrepancy between model and observations becomes larger than in the Ref-1 run, the experiment 'small slow & large very fast' is attributed as Ref-2 experiment. The main reason is the shape of the CDF, which follows better the logarithmic shape of the observed CDF of LF. Furthermore, the expansion rates fit better to observations from Jones et al. (2011), as described in section 3.3.

The effect on the IC is rather small. The number of grid-cells with high and medium IC decreases, while low IC increases. The reason is the increased expansion rate of large lakes, which occupy larger parts of the permafrost (Fig. 4.5).

4.2.3 Drainage probability

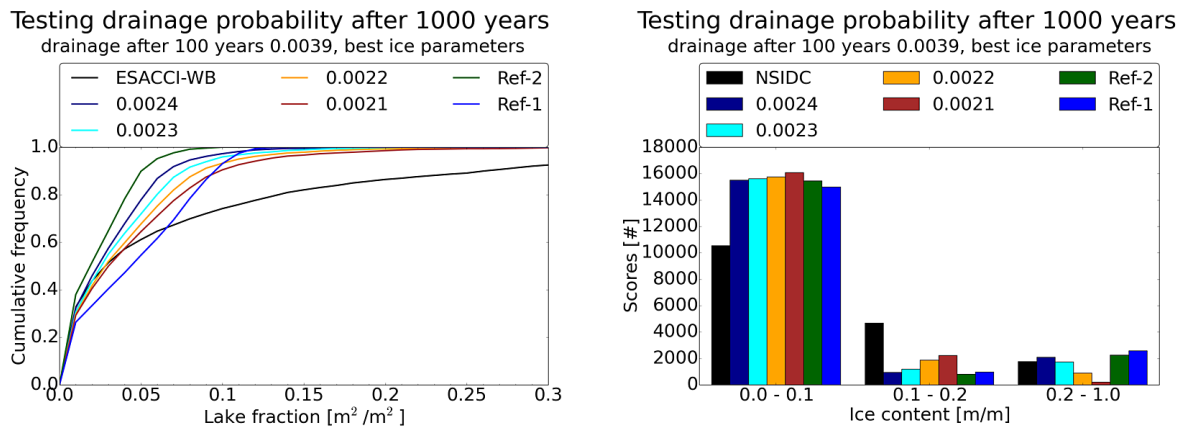


Figure 4.6: This figure shows the sensitivity of the TAPAS model to different drainage probabilities of lakes with an age of 1000 years ($drain_{1000}$). Relative to the Ref-2 experiment, $drain_{100}$ is set to 0.0039 for all experiments. The left figure shows CDF of LF in comparison to observations from ESACCI-WB and the right figure shows absolute frequency of IC in comparison to observations from NSIDC.

As discussed in the previous section 4.2.2, LF became too small after tuning the expansion rates, especially the large lakes. The expansion rate of large lakes cannot be further increased, because higher values exceed the observed range of expansion rates (see Sect. 3.3). Here, I aim to increase LF of large lakes without increasing LF of small lakes too much. The drainage

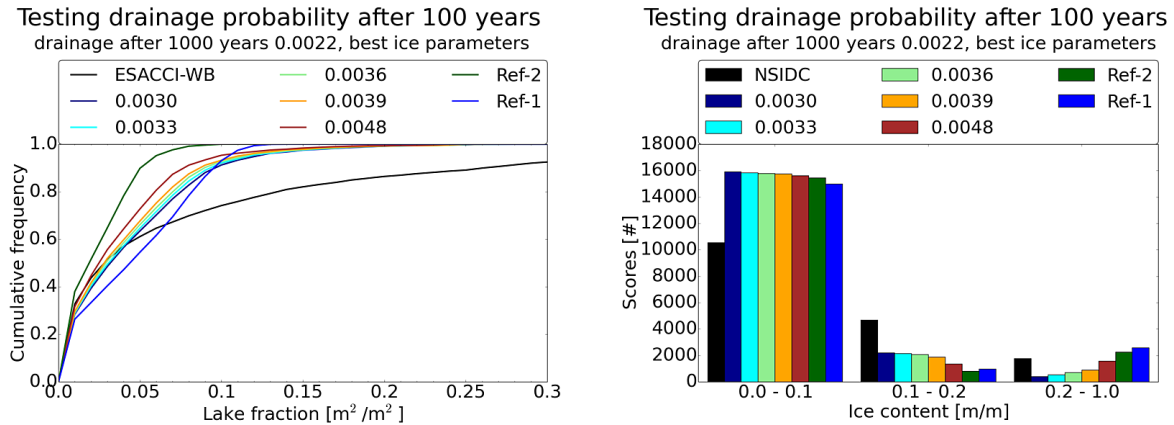


Figure 4.7: This figure shows the sensitivity of the TAPAS model to different drainage probabilities of lakes 100 years ($drain_{100}$). Relative to the Ref-2 experiment, $drain_{1000}$ is set to 0.0022 for all experiments. The left figure shows CDF of LF in comparison to observations from ESACCI-WB and the right figure shows absolute frequency of IC in comparison to observations from NSIDC.

probability of old lakes influences the lifetime of TKL. The longer lakes persist and expand, the larger LF can be reached. Is it possible to reduce the discrepancy between observed and modelled CDF of LF via decreasing the drainage probability of lakes? A large series of model runs is carried out with different sample of drainage probabilities after 100 years ($drain_{100}$) and after 1000 years ($drain_{1000}$). $drain_{1000}$ is continuously reduced from 0.0027 to 0.0018. Each $drain_{1000}$ is calculated with different $drain_{100}$ ranging from 0.0018 to 0.0060. The aim is to approach the CDF of LF as close as possible. The decisions are based on eye-sight views of the CDF of LF and the histograms of IC.

As visible in figure 4.6, large LF become much larger, if $drain_{1000}$ is reduced. The change grows with increasing LF, because large lakes remain longer and reach a larger size. The maximum LF increases with decreasing drainage probability of old lakes and is 0.25 for $drain_{1000} = 0.0022$ and 0.30 for $drain_{1000} = 0.0022$.

Drainage probability describes a logarithmic function of time (see Fig. 3.10). Therefore, drainage of young lakes decreases as well if drainage of old lakes is decreased. If $drain_{100}$ is set as in Ref-2, then the modelled LF becomes too high, because too many lakes reach large sizes. Therefore, the TAPAS model is tested with higher $drain_{100}$. Figure 4.7 shows the effect of different $drain_{100}$ on LF and IC. As expected, LF decreases with higher $drain_{100}$. For 0.0048 the CDF fits the observations up to a LF of 0.03, but then LF is largely too small because too few lakes develop large sizes. The best agreement with observed CDF is reached with $drain_{1000} = 0.0023$ and $drain_{1000} = 0.0022$ in combination with $drain_{100} = 0.0039$, because small LF are not too large and high IC is not too small. The Kolmogorov-Smirnov test shows that all modelled CDFs are significantly different from the observed CDF. Thereby, the highest p-values are reached with the scenarios $drain_{1000}$ equal 0.0021 and $drain_{1000}$ equal 0.0022. The p-value ranges in order of 10^{-9} to 10^{-6} throughout the scenarios. The CDFs of the experiments $drain_{1000}$ equal 0.0021, 0.0022, and 0.0023, respectively, are significantly different from Ref-2 on the 95 % level. The CDFs of the $drain_{100}$ experiments are significantly different from the ref-2 run on the 99 % level.

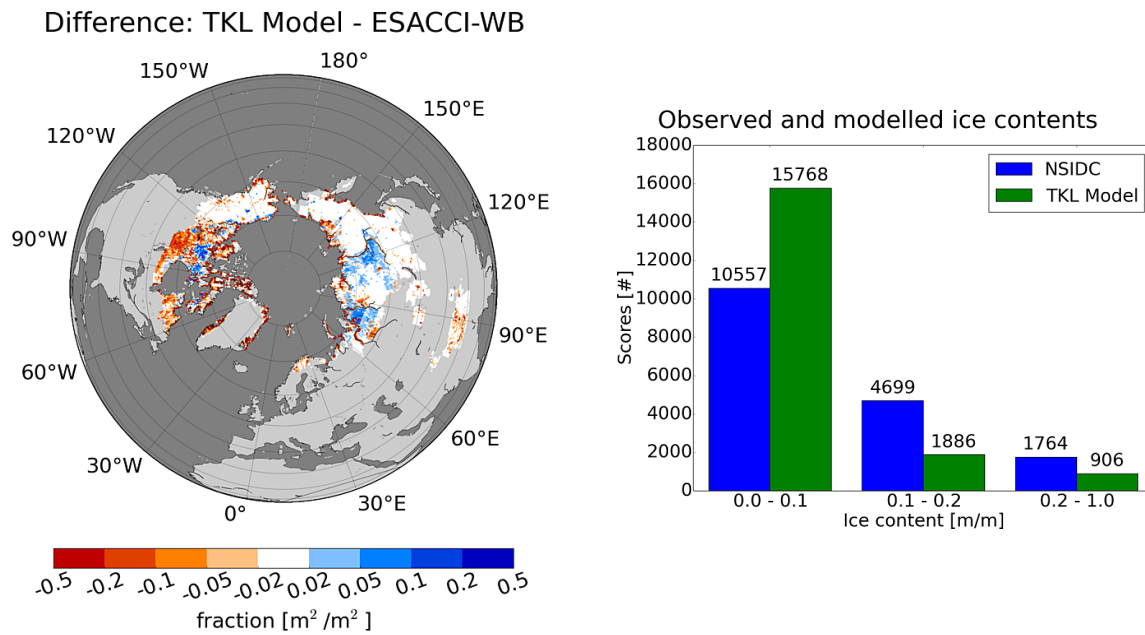


Figure 4.8: Left panel shows the difference between modelled LF with Ref-3 parameter settings and observed LF from ESACCI. Right panel shows modelled IC with Ref-3 parameter settings.

The number of grid cells with high IC decreases with decreasing $drain_{1000}$ and more grid cells with medium IC develop (see Fig. 4.6). Almost no grid cells with high IC are left for $drain_{1000} = 0.0021$, because too many large lakes melt too much ice. The effect on IC is very small for $drain_{1000} = 0.0024$, but increases for 0.0023 and to a larger amount for 0.0022. For 0.0022 the number of grid cells with high IC is smaller than observed. Medium IC duplicates in comparison to Ref-2 and Ref-1 runs. A drainage probability of 0.0022 is taken for lakes with an age of 1000 years, because the CDF of LF improves and more grid cells with medium IC are present.

The modelled IC is less sensitive to changes in $drain_{100}$ than to changes in $drain_{1000}$. The number of grid cells with high IC decreases if $drain_{100}$ is decreased from 0.0039 to 0.0030, while medium IC and low IC increase. Thus, more ice is melted, if a lake remains longer and reaches a larger size due to smaller $drain_{1000}$ than if more lakes remain due to smaller $drain_{100}$, which reach the same size.

At this stage, a new reference model run, Ref-3, is defined with parameter setting similar to Ref-2, but with different drainage probabilities after 100 years and 1000 years. The positive bias of LF relative to Ref-1 has decreased in central Siberia, western Siberian lowlands, and around the Mackenzie river in Canada (Fig. 4.1). Nevertheless, still too many lakes are present there in respect to observations from ESACCI (Fig. 4.8). Too few lakes are present in Quebec, eastern Siberian lowlands, and central Canada. Number of grid cells with high IC could be decreased via changing the ice aggregation time-scale. Although less grid cells with high IC are modelled than observed, the geographic distribution of IC fits much better to observations in Ref-3 than in Ref-1, as visible in the comparison figure 4.9. The ice content of regions around Mackenzie delta and large parts of western Siberian lowlands needs to be improved in the next steps.

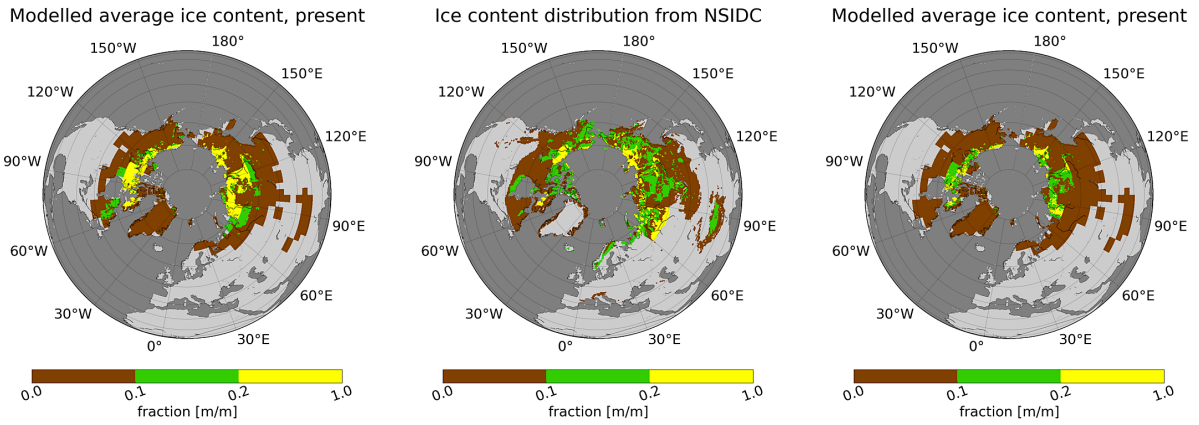


Figure 4.9: A comparison plot of modelled and observed ice content distribution from Ref-1 (left), NSIDC (middle), and Ref-3 (right).

4.3 Sensitivity to climate parameters

The main issue of this section is to test the sensitivity of the TAPAS model to changes within the climate parameters. As described in section 3.3.1, there are four different types of disturbances, which are regarded within the model. Does the model reach the observed distribution of lakes better, if thresholds for causing disturbance events are altered? Is it possible to improve the geographic distributions of LF and IC?

For the evaluation of climate parameters, CDF of LF and histograms of IC are not sufficient, because these methods are not sensitive to the geographic distribution of lakes and excess ice. Therefore, different methods are introduced in this section.

The least squared error method is applied to investigate the discrepancy between modelled fraction of TKL ($lake_{fract}$) and observed fraction of lakes from ESACCI ($lake_{esacci}$). It is calculated like the mean squared error, but without norming the sum of the squared differences with the number of grid cells (Eq. 4.1). Thus, the least summed squared error ($lsse$) reads as:

$$lsse = \sum (lake_{fract} - lake_{esacci})^2. \quad (4.1)$$

In the model, disturbances from temperature and snow are calculated with the third power of standard deviations above the mean (see Eq. 3.24 and 3.26). Infiltration disturbances are calculated with the first power, respectively (see Eq. 3.28). Here, the aim is to tune the sensitivity of the TAPAS model to climate extremes. Climate extremes like floods and hot summers inherit a high potential to disrupt the soil-heat balance and to trigger thermokarst in periglacial environments. Maybe, the peak of triggered TKL can be shifted towards climate extremes of larger magnitudes.

In some regions TKL mainly form after one type of disturbance events, while in other regions TKL mainly form after another type of disturbance events. Examples are shown in figures 3.6, 3.7, 3.8, and 3.9 for temperature, fire, snow, and infiltration disturbances for two time periods, respectively. Is it possible to reduce the discrepancy between observed and modelled LF in some regions via increasing the number of some type of disturbances? Here, the discrepancy is defined

as the absolute difference between observed and modelled LF. Δ_{diff} is the difference between the discrepancies of two model runs and is calculated as in the following equation 4.2.

$$\Delta_{diff} = |lake_{fract2} - lake_{esacci}| - |lake_{fract1} - lake_{esacci}| \quad (4.2)$$

4.3.1 Infiltration disturbances

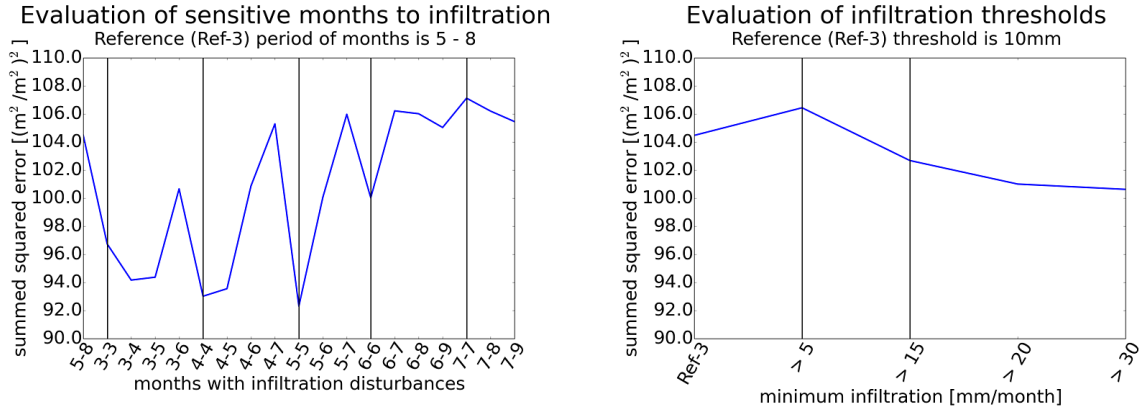


Figure 4.10: Left panel shows $lsse$ for different months, which are used for computing infiltration disturbances. The Ref-3 setting is labelled as '5-8'. Right panel shows $lsse$ for different infiltration disturbance thresholds. $thres_{infil}$ of Ref-3 is 10 mm

Here, the first step considers the different months, which are important for infiltration disturbances. Principally, the melting season extends from March to September in warm permafrost regions and to a shorter extension in colder regions. Is snow-melt or precipitation the main source of flood events? Snow melts at the beginning of the thawing season, while heavy rainfall is expected for the summer months. Therefore, $infil_{mon1}$ is altered from March to July and $infil_{mon2}$ from March to September. a_{infil} is adapted to the number of regarded months. In Ref-3, four months are regarded from May to August. If for instance, only one month is regarded, then a_{infil} is multiplied with 4 to ensure that the long-term mean number of disturbances is kept. As visible in figure 4.10, the smallest $lsse$ is reached, if only May is accounted for deriving infiltration disturbances. Generally, smaller $lsse$ is reached if the mid-latitudinal spring months March to May are used. These months are characterized by snow-melt in the Arctic. Melting water accumulates at the surface and cannot infiltrate into the soil, because it is still frozen. In summer precipitation can infiltrate the already thawed active layer and flood events need a larger amount of water.

The smallest $lsse$ is reached with May because the discrepancy improves in central Siberia and in northern parts of western Siberia. If April would be chosen, then the discrepancy worsens in northern Canada, at the Laptev sea coast, and in the Lena river delta. The reason is that snow-melt does not occur there in April. The time of snow-melt ranges from April in the sub-Arctic to June in high-Arctic regions like in the Canadian Archipelago and in the northernmost region of Siberia. May is used for computing infiltration disturbances in this thesis because it shows the smallest $lsse$.

The second step concerns the minimum monthly infiltration needed to develop floods at the surface and to trigger thermokarst. The minimum infiltration threshold is initially set to 10 mm and also used for Ref-3. To test the sensitivity, $thres_{infil}$ is altered between 5 mm, 15 mm, 20 mm, and 30 mm. The highest $lsse$ is reached for 5 mm and the lowest $lsse$ for 30 mm, while the rate of improvement decreases with increasing $thres_{infil}$ (see Fig. 4.10). The lower $lsse$ of higher thresholds shows, that the model is better excluding dry regions. With $thres_{infil} = 30$, Δ_{diff} decrease in central Siberia, north Siberia, and in northern parts of west Siberia. In those regions, too high LF is modelled with Ref-3 parameter setting (see Fig.4.8). Improvements are also visible in northern Canada. However, Δ_{diff} increases in Lena Delta and at the Laptev Sea coast. Too few lakes are triggered there, therefore, $thres_{infil}$ is not further increased. Following the findings of the sensitivity study in the section, following changes are performed in respect to Ref-3 parameter settings: $mon_{infil1} = May$, $mon_{infil2} = May$, $a_{infil} = 4$, and $thres_{infil} = 30$.

4.3.2 Temperature disturbance thresholds

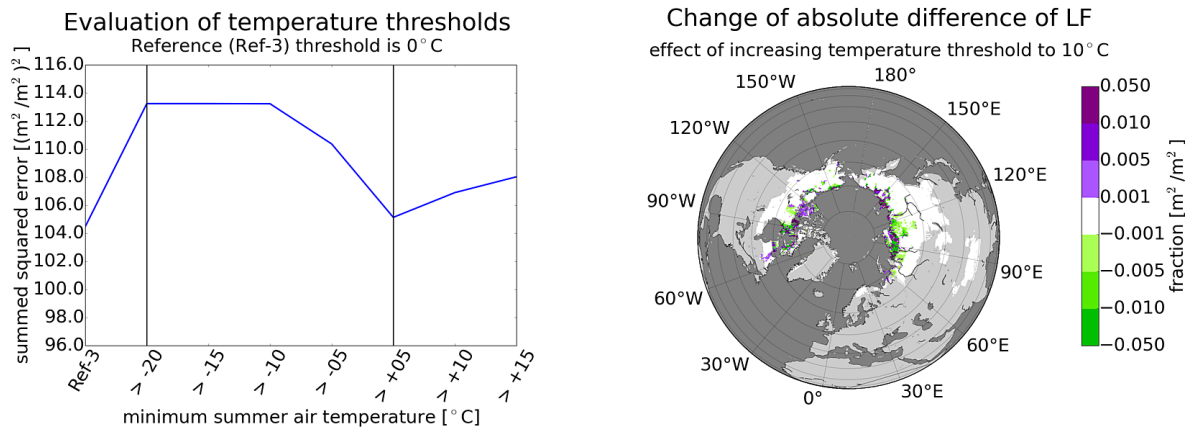


Figure 4.11: Left panel shows $lsse$ for different temperature disturbance thresholds. $thres_{temp}$ of Ref-3 is 0 °C. Right panel shows Δ_{diff} of increasing $thres_{temp}$ from 0 °C to 10 °C.

Here, different temperature thresholds are evaluated against the Ref-3 parameter setting. Several model runs are performed with $thres_{temp}$ of between -20 °C and 10 °C, while 0 °C agrees with Ref-3. $lsse$ increases if the temperature threshold is increased, and it increases as well if the threshold is decreased (see Fig. 4.11). Thus, disturbances can trigger thermokarst, as soon as the summer temperature exceeds the freezing point. Thus, ALD increases and excess-ice melts. Figure 4.11 shows an example, what happens, if the temperature threshold is set to 10 °C. Δ_{diff} shows a pattern of improvement and worsening north of about 67°N. The improvements are all related to areas with too high LF, while the worsening is visible in regions with a LF deficit. Concluding the sensitivity study here, $thres_{temp}$ is kept as it is set in Ref-3 with 0 °C.

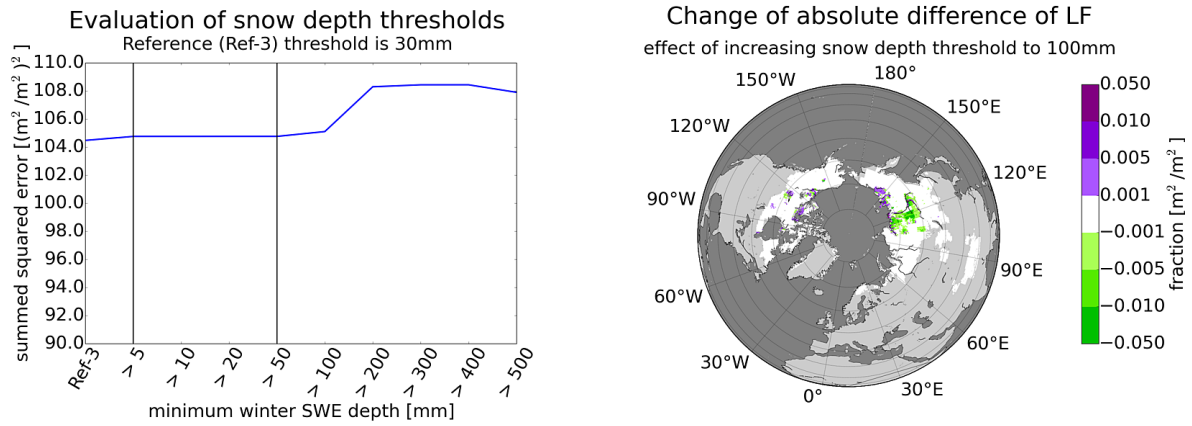


Figure 4.12: Left panel shows $lsse$ for different snow disturbance thresholds. $thres_{snow}$ of Ref-3 is 30 mm. Right panel shows Δ_{diff} if $thres_{snow}$ is increased from 30 mm to 100 mm.

4.3.3 Snow disturbance thresholds

Here, different snow disturbance thresholds are evaluated. Snow isolates the soil from atmospheric impacts during winter. A thick snow layer reduces freezing of soil during winter. Therefore, less energy is needed to thaw the active layer during summer, deeper soil layers are thawed more easily. The active layer depth increases and excess-ice melts. Above a certain snow layer thickness, isolation of snow is large enough to disturb the soils thermal heat balance and to trigger thermokarst. Several model runs are performed with $thres_{snow}$ of 5 mm, 10 mm, 20 mm, 50 mm, 100 mm, 200 mm, 300 mm, 400 mm and 500 mm, respectively. Ref-3 uses a threshold of 30 mm. Figure 4.12 shows $lsse$ for different thresholds, which does not vary for $thres_{snow}$ between 5 mm and 50 mm. It is slightly higher for 100 mm and much higher, if $thres_{snow}$ is set to 200 mm or higher. With a threshold of 100 mm Δ_{diff} improves around the river Lena and west of it (Fig. 4.12). Actually, this regions is located east of the central Siberian areas, where a higher $thres_{infil}$ improves Δ_{diff} (see Sect. 4.3.1). Unfortunately, LF reduces again at Laptev Sea coast and in eastern Siberian lowlands. Therefore, Δ_{diff} increases there, if $thres_{snow}$ is set to 100 mm. Less than 200 mm of snow falls in central and in eastern Siberia during one year (see Fig. 2.1). Therefore, a higher threshold influences these regions and not areas with a higher amount of snow like, e.g., western Siberian lowlands.

$thres_{snow}$ is set to 100 mm, because LF decreases around the Lena river and in central Siberia east of about 100°E.

4.3.4 Fire disturbances and surface runoff

k_{burn} regulates the number of disturbances caused by wildfires. The number of fire disturbances increases linearly with the yearly accumulated burnt area fraction (Eq. 3.25). Initially and in Ref-3, k_{burn} is set to 20000. This means, that one TKL is triggered, if a grid-cell fraction of $1 \cdot 10^{-5} m^2/m^2$ burns down throughout one year. Several model runs are performed with no, less, and more fire disturbances. k_{burn} is set to 0, 10000, and 30000, respectively. Higher values lead to LF larger than PF in warm permafrost regions, which is not realistic, because then the complete

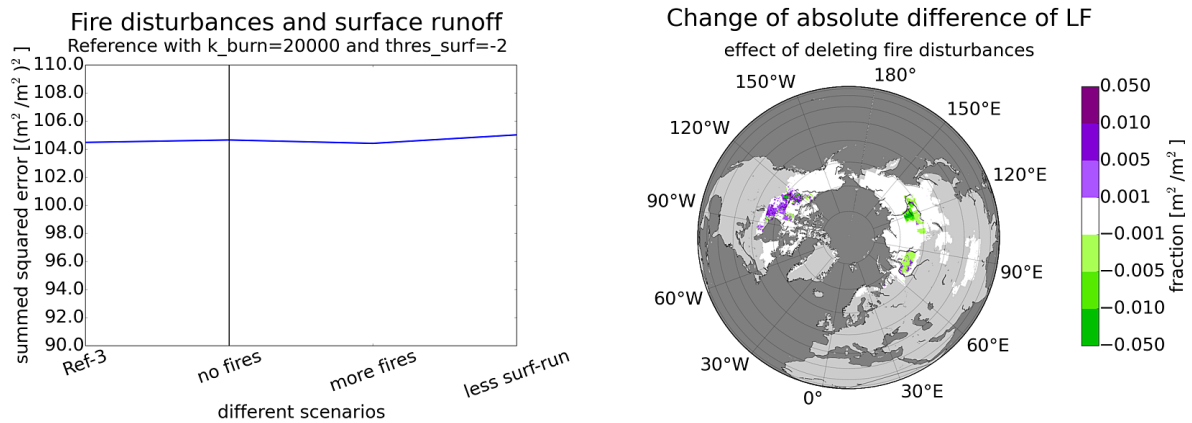


Figure 4.13: Sensitivity to fire disturbances is evaluation here. Left panel shows $lsse$ for different k_{burn} , which is 20000 in Ref-3. Additionally the effect of an extremely low threshold of surface runoff is shown. Right panel shows Δ_{diff} if no fire disturbances are initiated.

permafrost would be thawed and all lakes would drain. Following figure 4.13, $lsse$ remains the same for all scenarios. Δ_{diff} improves in the southern parts of the river Lena, western Siberian lowlands, and also in a small region southeaster of the Great-Slave Lake. However, in large parts of southern central Canada, the discrepancy increases. Δ_{diff} decreases, where LF is too high by more than $0.05 m^2/m^2$, as it is visible in figure 4.8. Thus, enough lakes develop without fire disturbances. Therefore, fire disturbances are excluded from future model runs.

The surface runoff limits development of lakes younger than 10 years. If the surface runoff is smaller than 2σ below the annual mean ($thres_{surf} = -2$), then an extreme dry year is assumed. Ponds may evaporate and stop their expansion. Within the model, they stop expanding for one time-step (i.e. one year). Ponds leave little hollows, which fill up with melting water in the following year, and the thermokarst process continues. If $thres_{surf}$ is set to -10, no stops occur, $lsse$ is almost the same (see Fig. 4.13) and the discrepancy does not change at all in comparison to Ref-3. A TKL evolves over centuries until it reaches a large size. The effect, that one lake develops some years slower does not matter. $thres_{surf}$ was introduced to regard dry years. Obviously, they are sufficiently regarded with $thres_{infil}$ and $thres_{snow}$. Therefore, surface runoff is not regarded in future model runs.

At this stage of the sensitivity studies, a new reference parameter setting (Ref-4) is defined. It differs from Ref-3 in $thres_{snow}$, $thres_{infil}$, $thres_{surf}$, and k_{burn} , as it is listed in table 4.2.

4.3.5 Climate sensitivity

Here, the aim is to enhance the sensitivity to extremes of summer temperature, winter snow depth, and infiltration, because the number of triggered TKL rarely varies with climate change within the model up to now. An investigation of the real sensitivity of lake formation to climate extreme events is technically difficult because not enough data are available. I suppose, that positive extreme events become more frequent during periods of warming than during periods of

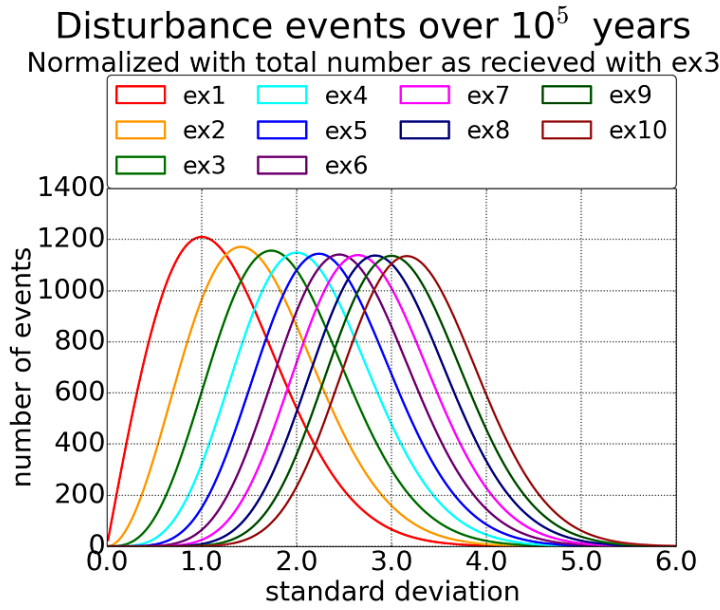


Figure 4.14: This figure shows the effect of computing disturbances with different exponents as in equation 3.24. The number of disturbances is normalized to the total number of disturbances as received with $b_{step} = 3$, what is labelled as ex3 here.

a_{step}	b_{step}	n_{dist}
2.0000	1	79795
1.5958	2	79795
1.0000	3	79795
0.5319	4	79795
0.2500	5	79795
0.1064	6	79795
0.0417	7	79795
0.0152	8	79795
0.0052	9	79795
0.0017	10	79795

Table 4.5: Factor a_{step} of equation 3.24 for different exponents b_{step} . The number of disturbances is normalized with the total number of disturbances, which is received with $a_{step} = 1$ and $b_{step} = 3$ over 10^5 'years'.

cooling. As described in section 3.3.1, the number of temperature disturbances, as computed with equation 3.24, reaches the maximum at $1.8 \sigma_{step}$ above μ_{step} . This property results due to the exponent b_{step} , which is set to 3. If the climate system is in equilibrium, then temperature events of single years are distributed normally around the climatological mean. The frequency of climate extremes of different magnitudes decreases exponentially with σ_{step} above μ_{step} . The number of triggered TKL follows a bell-shaped function with σ_{step} . The peak of the function depends on b_{step} and can be moved towards larger σ_{step} if b_{step} increases (see Fig. 4.14). The amplitude of the function depends on the factor a_{step} . Several model runs are performed with different exponents. The frequency of temperature extremes is computed analogous to a normal distribution between μ and 8σ in 0.025σ intervals. The frequency of certain events is multiplied with a very large number to ensure that also very large extreme events occur as well. Then, the number of disturbances is computed with different b_{step} as in equation 3.24. As expected, the maximum of the bell-shaped curve shifts towards higher σ_{step} , if the exponent is set to higher values (see Fig. 4.14). Note, that the total number of disturbances increases with larger b_{step} , because the amplitude of the peak increases. Therefore, larger b_{step} is combined with smaller a_{step} to keep the number of disturbances events at the same level, as listed in table 4.5. The events are normalized to the total number of disturbances, such as reached with $a_{step} = 1$ and $b_{step} = 3$.

Figure 4.15 shows the effect of different b_{step} and a_{step} on the chronological evolution of total area ('ar') and total number ('nr') of TKL. b_{step} is set to 3 in the 'Ref-4_2dw' run. It is set to 2, 4, 5, and 6 in the experiments 'T2', 'T4', 'T5', and 'T6', respectively. The model runs are

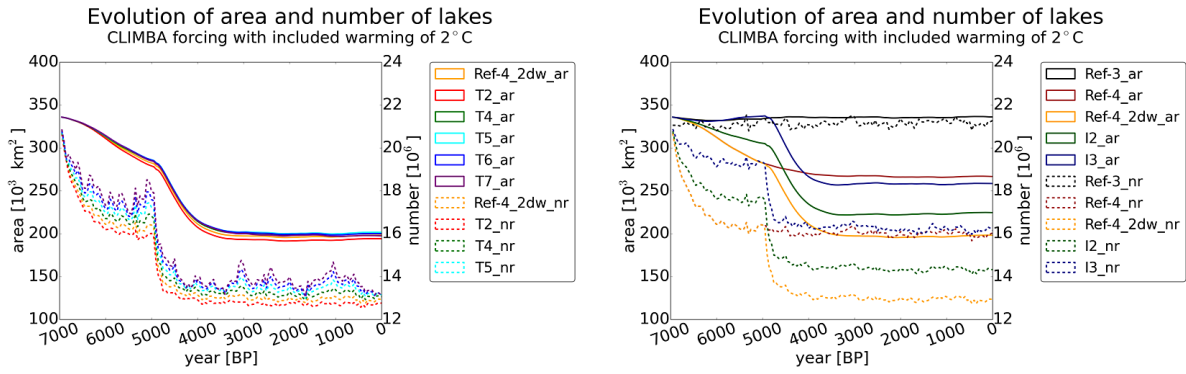


Figure 4.15: Left panel shows the temporal evolution of total lake area and total number of lakes for different a_{stemp} and b_{stemp} . Right panel shows the same for different b_{infil} . Here, an artificial climate warming is added to the CLIMBA forcing.

carried out with Ref-4 parameter setting. The total lake area decreases in the first 2000 years with Ref-4 parameter setting, because altered disturbance thresholds prevent formation of TKL in some regions.

A warming of 2 °C is added to the CLIMBA forcing for a period of 100 years between 5000 BP and 4900 BP. A large climate signal is introduced for better tuning the climate sensitivity of the TAPAS model. Several model runs are carried out with different b_{stemp} ranging from 1 to 10. Exponents of larger than 6 did not work, because LF became too large in some regions with small PF. For instance, if b_{stemp} is set to 6 ('T6_nr'), then 434 TKL are triggered on an area of 1000 km², if the summer temperature exceeds μ_{stemp} by 4 σ_{stemp} . Figure 4.15 shows, that the number of lakes varies the more the higher b_{stemp} is set. The reference scenario with b_{stemp} equal 3 shows weak response to climate changes, while the other scenarios show larger variabilities. The reason is, that temperature events of 1 σ_{stemp} above μ_{stemp} are very frequent and strongly contribute to disturbance formation if b_{stemp} is set to 3. If b_{stemp} is set to 6, their contribution to disturbance events decreases to a minimum (see Fig. 4.14). The total area of lakes increases slightly by less than 5 %, which can be tolerated for the benefit of higher climate sensitivity. The 2-sample Kolmogorov-Smirnov test shows a significant difference between the b_{stemp} equal 3 scenario and the other scenarios.

Similarly, b_{infil} is increased as well. b_{infil} is set to 1 in the experiments 'Ref-4' and 'Ref-4_2dw'. It is switched to 2 and 3 in the experiments 'I2' and 'I3', respectively. This method does not work well for infiltration (see Fig. 4.15). The total lake area is strongly increasing, if b_{infil} is raised from 1 to 3. a_{infil} is reduced from 4 to 2, respectively. Maybe, infiltration events are not normally distributed around μ_{infil} . If the frequency of infiltration events decreases analogous to a normal distribution with σ_{infil} , then the total number of disturbance would remain the same. The increase in total area indicates that a_{infil} is too high. Otherwise the total lakes area would be the same in all scenarios. The probability density function of infiltrations events maybe has a large positive skewness. Furthermore, no improvements are visible with the evolution of the total number of TKL. Therefore, the infiltration event parameters are not further investigated.

Following the positive effect on climate sensitivity to increased b_{stemp} , b_{wsnow} is set to higher values as well. The total lake area is conserved and the sensitivity is slightly increased.

In conclusion, b_{stemp} and b_{wsnow} are both set to 6, while a_{stemp} and a_{wsnow} are decreased to 0.106. The infiltration disturbance parameters a_{infil} and b_{infil} are kept as in Ref-4 parameter setting.

4.3.6 Absolute number of disturbances

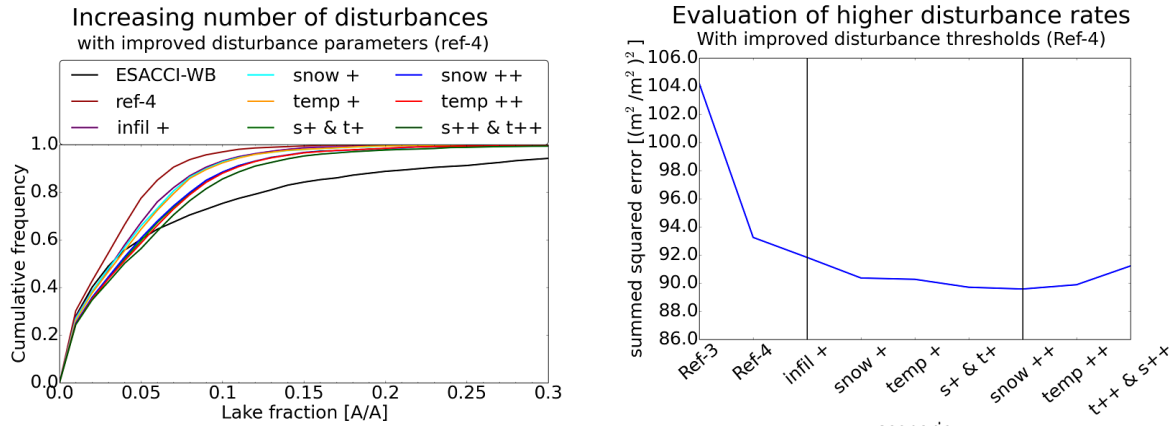


Figure 4.16: Effects of increasing the total number of different types of disturbance events is tested. Left panel shows CDF of LF and right panel shows the $lsse$. The labels correspond to different changes in a_{infil} , a_{wsnow} , and a_{stemp} , as listed in table 4.6. The b -parameters are left unchanged.

Scenario	a_{stemp}	b_{stemp}	a_{wsnow}	b_{wsnow}	a_{infil}	b_{infil}
Ref-4	1.000	3	1.000	3	4	1
infil +	0.106	6	0.106	6	8	1
snow +	0.106	6	0.212	6	4	1
temp +	0.212	6	0.106	6	4	1
s+ & t+	0.212	6	0.212	6	4	1
snow ++	0.106	6	0.318	6	4	1
temp ++	0.318	6	0.106	6	4	1
s++ & t++	0.318	6	0.318	6	4	1

Table 4.6: Following changes of a_{infil} , a_{wsnow} , and a_{stemp} are performed to test the sensitivity to changes in number of disturbance events in comparison to Ref-4. The scenario names in left panel are the same as the legend labels in figure 4.16.

Here, the aim is to improve the regional distribution of TKL via increasing the total number of different types of disturbance events. This study is carried out with Ref-4 parameter setting and the improved disturbance equation parameters as described in the previous section above. Several model runs are carried out with different a_{infil} , a_{wsnow} , and a_{stemp} to investigate effects on LF and IC (see Table 4.6). As shown in figure 4.16, the least summed squared error decreases if the number of disturbances is increased and reaches the minimum for the configured 'snow ++' closely followed by 'temp ++' and 's+ & t+'. Doubling infiltration disturbances improves

the least summed squared error to a smaller magnitude than doubling temperature or snow disturbances. The CDF of LF fits best to observed CDF, if snow disturbances or temperature disturbances are doubled, i.e. 'snow +' and 'temp +' (see Fig. 4.16). Small LF become too large, for 'temp ++', 'snow ++', 's+ & t+', and 's++ & t++'. For most scenarios, a higher number of grid cells with medium IC is visible. Too many lakes are triggered in these scenarios, which thaw permafrost and melt excess-ice.

The best combination of improvements in respect to modelled distributions of LF and IC is reached by the scenarios 'snow +' and 'temp +'. The least summed squared error decreases in both scenarios. Δ_{diff} improves in both scenarios in eastern Siberian lowlands, Quebec, and in large parts of central Canada due to higher LF. Worsening occur in western Siberian lowlands, in central Siberia, and around the river Lena. In central Siberia, Δ_{diff} worsens by a higher magnitude with 'temp +' than with 'snow +'. The annual snowfall measures less than 100 mm there (see Fig. 2.1). Since this value is smaller than $thres_{wsnow}$, TKL are not triggered by snow disturbances and 'snow +' influences LF less than 'temp +'. Therefore, the number of snow disturbances is increased in future model runs and not the number of temperature disturbances. Thus, a_{wsnow} is set to 0.212 in future model runs.

4.4 Retuning model parameters

4.4.1 pore-size and drainage amplification

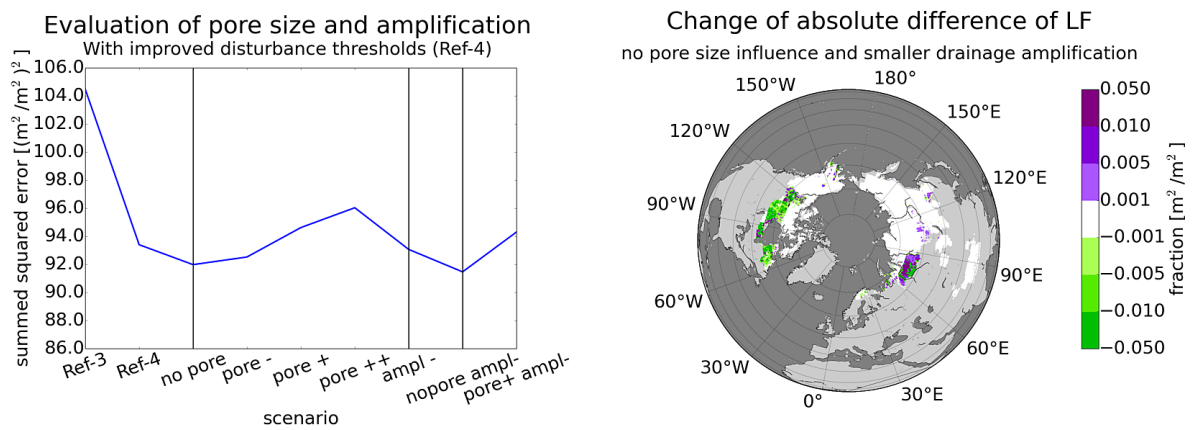


Figure 4.17: Left panel shows $lsse$ of different drainage amplification and pore-size influence scenarios. Right panel shows Δ_{diff} between the scenario with decreases $drain_{ampl}$ and deleted pore-size influence and Ref-4

Here, the sensitivity to different pore-size influences and drainage amplification is investigated again. Several model runs are performed with Ref-4 parameter setting, but with altered $drain_{ampl}$ and $thres_{ice2}$. The drainage amplification is reduced to 1.2, which is labelled as 'ampl -' in figure 4.17. Smaller values results in too high LF in lowland regions with small PF. LF increases in southern parts of central Canada and of western Siberian lowlands and in Quebec. Therefore,

$lsse$ decreases (see Fig. 4.17). The reduced drainage amplification neither influences the CDF of LF nor the histogram of IC.

To investigate the sensitivity of pore-size influence, several model runs are performed with Ref-4 setting, but with different $thres_{ice2}$, which alternated between -1 °C, -4 °C, -8 °C, and -10 °C. These model runs are labelled as 'no pore', 'less pore', 'more pore', and 'much pore', respectively, in figure 4.17. The smallest $lsse$ is visible, if pore-size is not regarded as a limiting factor of ice formation. $lsse$ decreases more, if 'ampl -' combines with 'no pore'. CDF of LF improves slightly towards higher lake fractions in the 'no pore' scenario. Actually, the maximum LF of Ref-3 is reached neither by Ref-4 nor by any other scenario in this section. The histograms of IC suggest a marginal change with decreasing $drain_{ampl}$ and different $thres_{ice2}$. These parameters affect warm permafrost regions more than cold regions. Warm permafrost regions hardly reach high or medium IC in these simulations.

With the 'no pore and ampl -' scenario, Δ_{diff} shows large improvements in Quebec and southern parts of central Canada. However, in southern parts of the western Siberian lowlands, there is a mixture of improvement and worsening. This scenario shows the largest improvement relative to Ref-4. Therefore, $drain_{ampl}$ is set to 1.2 in future model runs. The pore-size influence is not regarded in the TAPAS model from now on. Calculations with pore-size are obsolete and $thres_{ice2}$ is deleted. Also, the lower ice aggregation threshold ($thres_{ice3}$) is deleted. In very cold regions, the amount of liquid water is small and not enough water is available for aggregation of excess-ice.

A new reference parameter setting (Ref-5) is set up. As listed in table 4.2, Ref-5 differs from Ref-4 by following parameters: a_{stemp} , b_{stemp} , a_{wsnow} , b_{wsnow} , $drain_{ampl}$, $thres_{ice2}$, and $thres_{ice3}$. The CDF of lakes improves relative to Ref-4 and reaches more or less the CDF of Ref-3. The maximum LF of Ref-5 exceeds the maximum of Ref-3. The least summed squared error reduces from Ref-4 to Ref-5, as it can be seen in figure 4.18.

4.4.2 Area of new ponds and ice aggregation time-scale

Here, different initial areas of new ponds and ice aggregation time-scales are evaluated against the model run with Ref-5 parameter setting. Several model runs are carried out with different A_0 and τ . A_0 alternates between 1 m², 10 m², and 1000 m², while τ switches between 1500, 1000, and 500 years. The CDF of LF moves towards higher LF for shorter τ , while it rarely changes with different A_0 . The high sensitivity of LF to shorter ice aggregation time-sales relates to a higher ice content of the soil. Due to higher ice depth, depressions become deeper and are filled with more melting water. Figure 4.18 shows histograms of IC. The number of grid cells with high IC increases with decreasing A_0 , because the lakes melt a smaller area of the permafrost. Medium IC remains the same for all A_0 scenarios. As expected, the sensitivity of IC to τ is much larger than to A_0 . The number of grid cells with high IC increases with shorter time-scale, while number of grid cells with low IC reduces. Actually, medium IC shows very small variations between the different scenarios.

$lsse$ reduces slightly for A_0 equal 1000 m² and τ equal 1500 y. However, the reduction is small in comparison to the improvement from Ref-3 to Ref-5 (Fig. 4.18). LF becomes larger for

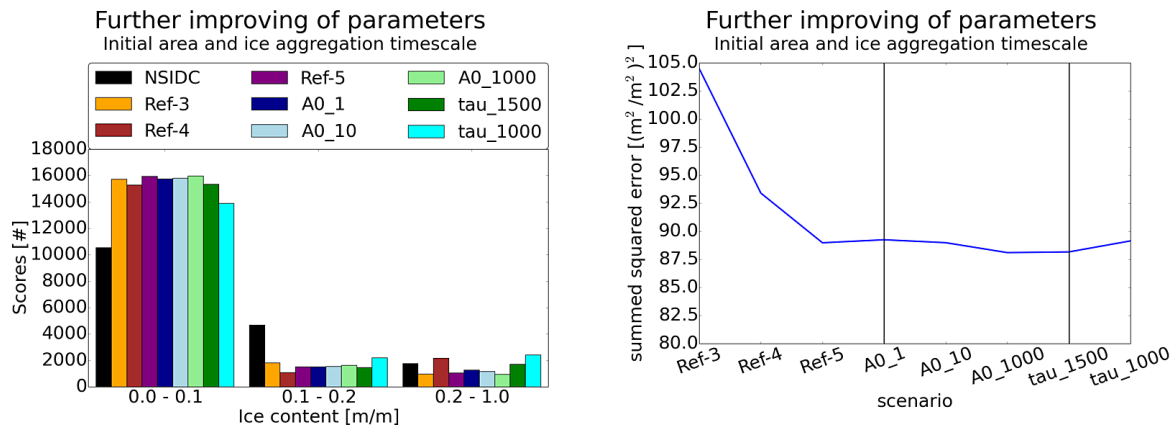


Figure 4.18: Evaluation of sensitivity to different initial areas of new ponds and ice aggregation time-scales relative to Ref-5. Left panel shows histograms of IC and right panel $lsse$ between observed and modelled LF.

shorter ice aggregation time-scales. More excess-ice accumulates in areas with drained basins until they are affected by thermokarst again. Therefore, evolving TKL are supplied with more water and cover a larger area of the surface. Therefore, Δ_{diff} worsens in large regions of western and central Siberia, Alaska, and in northern Canada. LF improves in southern central Canada and in the eastern Siberian lowlands. Thereby, Δ_{diff} often changes by more than $0.01 \text{ m}^2/\text{m}^2$. A higher initial area results in a similar shape of worsening and improvement of Δ_{diff} , but the magnitude is much smaller for A_0 equal 1000 m^2 than for τ equal 1500 y .

Overall, worsening exceeds the improvements, if the ice aggregation time-scale is decreased because of too high LF. Little changes are observed for different initial areas, while larger A_0 tends to lead too higher LF. Therefore, A_0 and τ are kept as they are set in Ref-5.

4.4.3 Expansion rate and drainage probability

Scenario	smaller 1 ha	smaller 10 ha	smaller 40 ha	larger 40 ha
Ref-5	0.10 m/y	0.20 m/y	0.40 m/y	0.60 m/y
exp 0-	0.10 m/y	0.20 m/y	0.30 m/y	0.40 m/y
exp 0-	0.10 m/y	0.20 m/y	0.25 m/y	0.30 m/y
exp +-	0.20 m/y	0.25 m/y	0.30 m/y	0.40 m/y
exp +-	0.20 m/y	0.25 m/y	0.25 m/y	0.30 m/y

Table 4.7: Following expansion rates are evaluated against the Ref-5 run. The scenarios are named as they are labelled in figure 4.19.

Here, the sensitivity of the model to different expansion rates is tested again. Four different combinations of expansion rates are evaluated against those of Ref-5, as listed in table 4.7. Also the drainage probability of large lakes is tuned. Parameter $drain_{1000}$ is alternated between 0.0021 and 0.0023 with the aim to increase larger LF and to increase the number of grid-cells with high

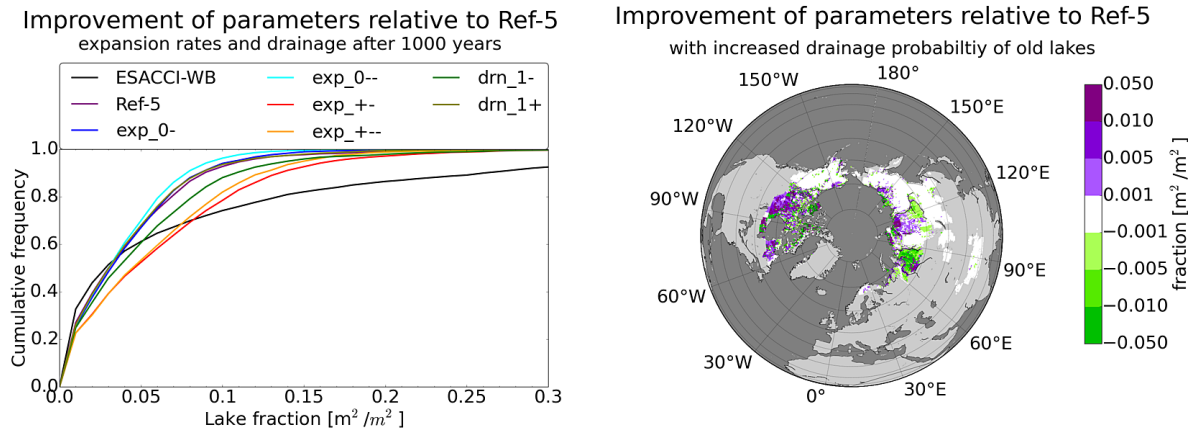


Figure 4.19: Evaluation of sensitivity to different expansion rates and to different drainage probabilities after 1000 years in comparison to Ref-5. Left panel shows CDF of LF and right panel Δ_{diff} for a reduced expansion rate of large lakes ('exp 0-'). The expansion rates to the labels are listed in table 4.7.

IC. These scenarios are labelled as 'drn 1-' and 'drn 1+', respectively (see Fig. 4.19). Higher drainage probabilities have been tested as well, but these scenarios result in too small LF. Smaller drainage probabilities result in too small IC, because TKL persist longer and reach larger sizes. A larger expansion rate of young lakes, i.e. 'exp ++' and 'exp +-', results in a larger LF of smaller lakes (see Fig. 4.19). As expected, a smaller drainage probability of large lakes ('drn 1-') results in higher LF. The least summed squared error slightly decreases for 'exp ++' and 'drn 1-', and it slightly increases for 'exp 0-' and 'exp +-'. However, $lsse$ shows no large sensitivity to the different scenarios.

As visible in figure 4.19, the CDF of LF is almost the same for the scenarios Ref-5, 'exp 0-', and 'drn 1+'. Therefore, a higher drainage probability of old lakes has a similar effect on LF as a smaller expansion rate of large lakes. This means, that in both cases the lake fraction of large lakes decreases by the same magnitude. The number of grid cells with high IC increases in both scenarios 'exp 0-', and 'drn 1+' and exceeds the observations from NSIDC (not shown here). Thereby, the number of observed grid cells with high, medium, and low IC is better reached with 'drn 1+' than with 'exp 0-'.

Δ_{diff} improves in western Siberian lowlands, around the river Lena, and at the Laptev Sea coast. Worsening occurs due to smaller LF in northern Siberia, Quebec, and in central Canada. Improvements occur on larger areas in scenario 'drn 1+' than in 'exp 0-'.

Following the findings of this sensitivity study, the expansion rates are kept as they are set in Ref-5. A higher drainage probability of old lakes improves the modelled ice content and reduces Δ_{diff} in many regions. Therefore, $drain_{1000}$ is finally set to 0.0023, as listed in table 4.2.

The last step of the sensitivity studies concerns with the drainage probability of young lakes. The aim is to increase the LF and to reduce the number of grid cells with high IC and to reach the observed values for high IC. Thereby, $drain_{100}$ is reduced and alternately set to 0.0037, 0.0035, 0.0033, and 0.0031.

Figure 4.20 shows, that the CDF moves towards higher LF, if $drain_{prob}$ is reduced. As expected, number of grid cells with high IC decreases and approaches the observations. The $lsse$ decreases

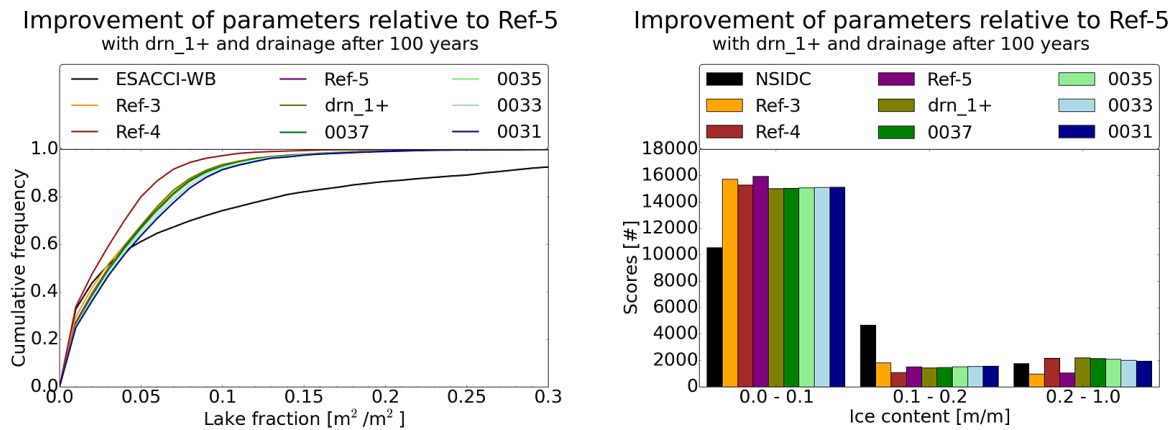


Figure 4.20: Evaluation of sensitivity to different drainage probabilities after 100 years in comparison to the 'drn 1+' scenario. Left panel shows CDF of LF and right panel the histogram of IC.

to 88.14, which is a slight improvement in comparison to the Ref-5 run (see Fig.4.18). Δ_{diff} shows improvements in Eastern Siberian lowlands and parts of central Canada. However, worsening occurs in northern part of western Siberian lowlands and around the Lena river.

Concluding this sensitivity study, a final set of parameters is defined with altered $drain_{100}$ and $drain_{1000}$ in comparison to the Ref-5 parameter setting (see Table 4.2). LF is most sensitive to the expansion rates and drainage probability parameters. Drainage governs the average life-time of TKL and, therefore, the areas which can be reached by them. Thereby, $drain_{100}$ influences the CDF of LF more than $drain_{1000}$. The TAPAS model is also sensitive to the excess-ice aggregation time scale. A smaller time-scale leads to larger ice-depth and, therefore, to a larger LF. TAPAS is less sensitive to the initial area of new ponds than to e.g. to the expansion rates of TKL, because evolution of lakes is simulated over centuries and a smaller area is quickly compensated by a larger expansion rate. Other parameters are less important for the TAPAS model. A different threshold of pore-size limitation does not largely change the modelled LF. A lower ice-formation threshold is not considered from now on because it is not physical. Short melting periods occur in all periglacial environments. Also the surface-runoff parameter is not important. Lakes develop over centuries and a delay of some years does not play a role.

It is not known how lake formation correlates to climate extreme events like high summer temperature, high winter snow depth, flood events, and wildfires. However, the disturbance parameters are tuned to increase the climate sensitivity of the TAPAS model, which is successfully improved by increasing the disturbance parameters b_{stemp} (for summer temperature) and b_{wsnow} (for winter snow depth). Also the regional distribution of TKL is improved in comparison to observations by tuning the disturbance formation threshold parameters.

The final setting is used for the following model runs in the next chapters.

5 Response of thermokarst lakes to potential climate change

This chapter concerns the response of the TAPAS model to climate change. A strong high-latitude warming is projected for the next 100 years. Which impacts can be expected on distribution of TKL, if the climate changes by several degrees? How many lakes are triggered and which equilibrium state will be reached after several millennia? What is the time scale for reaching the new equilibrium? During the Holocene, different periods of warming and cooling are derived from proxy data. How has climate cooling affected thermokarst in comparison to climate warming?

Since thermokarst lakes (TKL) evolve over many centuries, impacts of climate warming may extend over centuries to millennia. The TAPAS model is driven with CLIMBA forcing. CLIMBA shows a smaller climate signal over the past 6000 years than suggested by observations. To investigate effects of large climate impacts, I designed several scenarios of prescribed climate change, which are discussed in this chapter and evaluated against the control run. The control run (Table 5.2) is driven by CLIMBA forcing data without additional changes. It is carried out with the final parameter setting, as it is obtained from the sensitivity studies in chapter 4. The TAPAS model runs once with constant permafrost area (cntrlCPF) and again with variable permafrost area (cntrlVPF).

This chapter consists of in three parts:

- First, the differences between the two model settings and the climate change scenarios are described in detail (Sect. 5.1). They include additional warming and cooling of several degrees during the 100-year period 5000 - 4900 BP (sustained until pre-industrial times).
- Second, temporal evolutions of the total area of lakes (TAL) and the total number of lakes (TNL) are investigated (Sect. 5.2). TAL and TNL comprise all TKL counted over the Arctic. The permafrost fraction (PF) is kept constant in order to investigate the effects of climate scenarios on the thermokarst processes. How does the TAPAS model respond to climate change in respect to formation of new lakes and accumulation of excess ice? The aim is to investigate the time-scale of reaching new equilibrium states of TAL and TNL.
- Third, again temporal evolutions of TNL and TAL are investigated, but with variable PF (Sect. 5.3). The full TAPAS model is applied, including all permafrost processes, to investigate the response to different climate signals. Here, the aim is to evaluate changes of the pan-Arctic distribution of lake fraction (LF) and ice content (IC) in comparison to the control run (cntrlVPF).

5.1 Overview of the climate scenarios

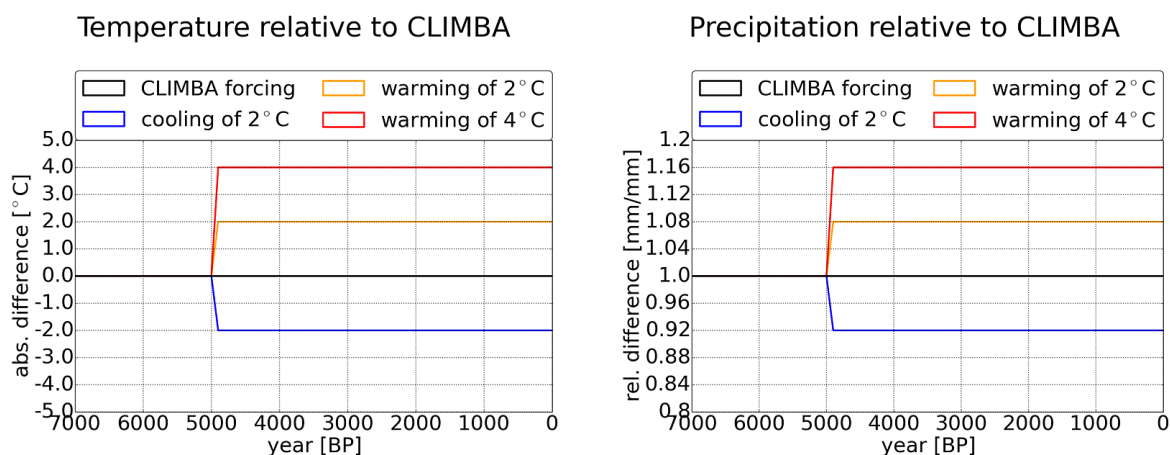


Figure 5.1: This figure shows the temperature change (left panel) and precipitation change (right panel), which are added to the CLIMBA forcing data for different climate scenarios.

This section provides an overview of the different climate scenarios. A time period of 1000 years is used as spin up period for the TAPAS model. A restart file was created with data from a 500 year period extending from 6970 BP to 6470 BP. The input data for this period is cyclically used by the TAPAS model until an equilibrium state is reached in TAL and TNL. The model starts with the same restart file in each scenario at 6000 BP. A spin-up period of 1000 years (6000 - 5000 BP) is used to ensure that the model has levelled out completely. The following 100 year period (i.e. 5000 - 4999 BP) is attributed to a period with a strong climate change. Depending on the scenario, temperature increases or decreases by several degrees. Since precipitation is linked to temperature due to the water holding capacity of the atmosphere, rainfall is changed as well. After 100 years, precipitation and temperature reach a new plateau, where they remain for the remaining 4900 years of the modelled time period (see Fig. 5.1).

Region	Temperature [°C]	Precipitation [%]
Arctic lands	3.9 ± 0.8	17 ± 3.5
Arctic oceans	4.9 ± 1.4	21 ± 5.0
North Asia	3.2 ± 0.7	12 ± 2.5
Northern Europe	2.7 ± 0.7	8 ± 2.5
Canada, Greenland, Iceland	3.2 ± 0.8	11 ± 2.0
Alaska and northwester Canada	3.5 ± 0.9	14 ± 3.0

Table 5.1: This table lists the predicted climate change between period 1986 - 2005 and 2081 - 2100, as generated with the RCP-4.5 scenario. The numbers give median and interquartile range of a sample of 42 models (IPCC, 2014).

Following the RCP-4.5 scenario, a warming of about 3.9 ± 0.8 °C is predicted for Arctic land areas by the end of the 21st century. Thereby, precipitation may increase by 17 ± 3.5 % (IPCC, 2014). Table 5.1 lists projected change of temperature and precipitation for different Arctic

regions between the 20-year time periods 1986 - 2005 and 2081 - 2100. These results are median and inter-quartile-range of 42 different model runs. A strong climate warming is predicted for the periglacial Arctic environments. Therefore, investigations of potential consequences on thermokarst formation are of great interest.

Following the climate scenarios, temperature and precipitation changes are defined for the model runs, as shown in figure 5.1 and listed in table 5.2. The offset is simply added to the CLIMBA forcing data. Additionally, a control run is carried out with no artificial climate change between 5000 BP and 4900 BP.

Temperature change influences the number of disturbance events due to summer temperature,

Scenario	Temperature	Precipitation	Permafrost
cntrlCPF	no change	no change	constant PF
2dwCPF	+2 °C	+08 %	constant PF
4dwCPF	+4 °C	+16 %	constant PF
2dcCPF	-2 °C	-08 %	constant PF
cntrlVPF	no change	no change	variable PF
2dwVPF	+2 °C	+08 %	variable PF
4dwVPF	+4 °C	+16 %	variable PF
2dcVPF	-2 °C	-08 %	variable PF

Table 5.2: This table gives an overview of modelled climate change scenarios during this study. From left to right, it lists abbreviation, temperature change, and if permafrost is constant or not.

while precipitation is important for infiltration disturbances. Therefore, a large signal is expected on the number of triggered TKL and it is expected that TNL increases with increasing temperature. New ponds are small and do not contribute much to the surface area covered by lakes. However, their contribution increases over time as they expand. After several centuries, the signal should be visible in TAL as well.

Note, that PF is computed as a function of long-term mean annual air temperature. Therefore, it decreases strongly, if for instance temperature increases by 2 °C. As explained in section 3.3.4, *drain_{ampl}* increases the drainage probability and the number of lakes reduces. This results in decreasing TNL even though more lakes are triggered. Thus, variations in PF overcompensate the climate signal on TNL by a significant amount. An example is given in figure 4.15 for a warming of 2 °C. As visible on the figure, the total number of lakes strongly decreases during the first centuries after the climate changes.

Therefore, all scenarios are carried out two times: one time with constant PF and another time with variable PF, where PF is interactively calculated based on temperature. For the model runs with constant PF, PF is set to values as they are provided by NSIDC (Brown et al., 1998). The aim of this study is to investigate how climate signals are affecting evolution and formation of thermokarst lakes within the model.

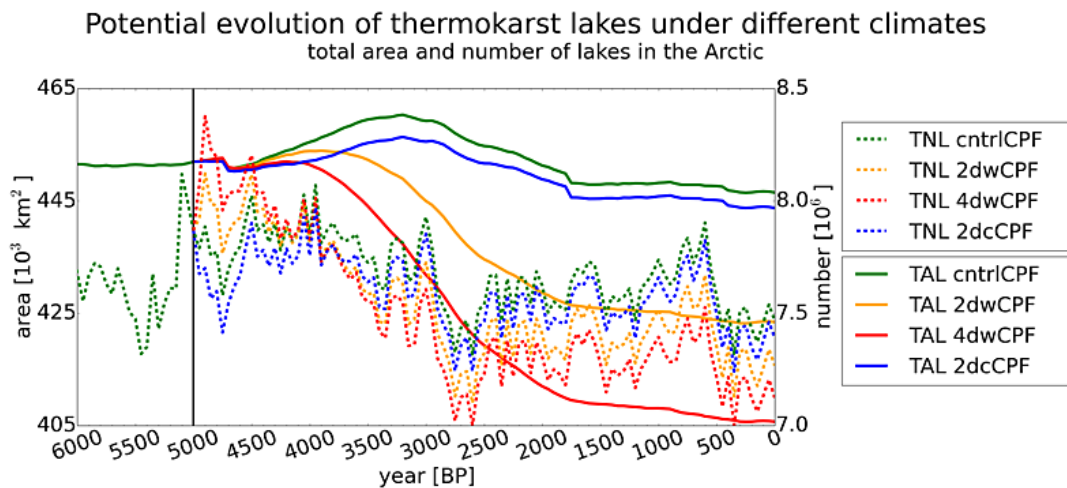


Figure 5.2: This figure shows time series of total number and total area of lakes in the Arctic for the past 6000 years. PF is constantly set to values as observed by NSIDC (Brown et al., 1998). The control run is driven by CLIMBA forcing data, while the scenarios include different magnitudes of climate change between 5000 BP and 4900 BP.

5.2 Influence of climate change on thermokarst without permafrost changes

This section is concerned with the response of thermokarst to different magnitudes of climate change. It is assumed, that a higher number of new lakes is triggered in periods of climate warming. The higher number of lakes is shifted from one age class to the other until it has drained. As explained in section 5.1, three climate scenarios are defined with different magnitudes of climate change during the 100-year period 5000 BP and 4900 BP (see Fig. 5.1). The analysis of the temporal evolution of thermokarst is performed in two steps. The total number of lakes (TNL) is discussed in the first part and the total area of lakes (TAL) is discussed in the second part.

For the first part of this study, all permafrost related changes have been removed from the TAPAS model, because a variable PF superposes the climate signal on the temporal evolution of thermokarst lakes.

5.2.1 Temporal evolution until pre-industrial times

The following questions will be investigated: How long are climate signals visible within the temporal evolution of thermokarst? How does the TAPAS model respond to different forms of climate change? Which equilibrium states are reached at pre-industrial times, 5000 years after climate change? Regions may respond differently to climate change. Where are large changes of lake area and number of lakes visible?

Measure	Year	cntrlCPF [%]	2dwCPF [%]	4dwCPF [%]	2dcCPF [%]
<i>TNL</i>	4900 BP	0.22	3.23	6.46	-2.13
<i>TNL</i>	pre-industrial	-5.08	-7.63	-9.45	-6.06
<i>TAL</i>	4900 BP	0.04	0.05	0.06	0.03
<i>TAL</i>	pre-industrial	-1.21	-6.31	-10.23	-1.82

Table 5.3: This table lists the relative change of TNL and TAL from time-step 5000 BP to 4900 BP and from 5000 BP to pre-industrial times. PF is constantly set to values as observed by NSIDC (Brown et al., 1998). The control run is driven by CLIMBA forcing data only, while the other model runs are driven by CLIMBA and different scenarios of climate change between 5000 BP and 4900 BP.

Figure 5.2 shows the temporal evolutions of TNL and TAL. As expected, TNL reacts differently for different climate scenarios. TNL initially increases in the scenarios of climate warming, while it decreases in the cooling scenario. The cntrlCPF run shows decreasing TNL as well, but this relates to internal climate variability. TNL increases in the centuries before 4000 BP and decreases again afterwards. Similar variations are also visible in the time periods around 3000 BP and around 500 BP, respectively (see Fig. 5.2). Due to increasing temperature, extreme events become more probable. Therefore, more lakes are triggered. Also larger extremes are reached. The difference of TNL between the scenarios is largest between 4900 BP and 4850 BP. Table 5.3 lists the relative change of TNL in comparison to TNL at 5000 BP for each climate scenario. Between 5000 BP and 4900 BP, TNL increases by 3.23 % and 6.46 % in the warming scenarios and decreases in the cooling scenario. However, TNL decreases again during the following centuries. For instance, TNL of the 4dwCPF scenario exceeds TNL of the 2dwCPF scenario by 0.686 million lakes in 4900 BC. This difference decreases to -0.221 million lakes during the following 1700 years. Less TKL are present in the warming scenario than in the cooling scenario. After 3200 BP, the difference fluctuates by several 10^4 lakes until pre-industrial times. Due to the large temperature trend between 5000 BP and 4900 BP, a very high number of new ponds is triggered in the warming scenarios (see Fig. 5.3). These lakes are ageing and expanding in the following centuries. After complete drainage of the peak of new lakes, TNL could be the same again, because climate variability is the same in all scenarios after 4900 BP. Actually, a crossing point is visible in 4100 BC, when TNL is the same in both warming scenarios and in the cntrlCPF run. The absolute differences between the scenarios increases again after 4100 BP until 3100 BP.

The number of new lakes is determined as a function of anomaly above mean and standard deviation (see Sect. 3.3.1). Since climate variability is the same in all scenarios after 4900 BP the same number of new lakes is triggered, if the thresholds of disturbance formation are passed. Due to prescribed temperature and infiltration thresholds, the regional distribution of triggered lakes changes throughout the model runs. The number of lakes decreases in some regions as well if no excess-ice forms due to too high temperatures. In this case permafrost disappears, but PF is kept constant. Therefore, the previously accumulated ice remains until it is melted by evolving TKL. The average ice content of all permafrost areas decreases in the warming scenarios until 3100 BP. In the cooling scenarios it increases until 3100 BP (not shown here). The climate signal in formation of TKL is visible for 900 years and the effect of decreased ice formation is visible for 1900 years. After 3100 BP, the difference between TNL of various scenarios remains constant

until pre-industrial times.

In the TAPAS model, the regional distribution of TKL is primarily governed by thresholds of disturbance formation and the accumulated depth of excess ice. Since PF is kept constant here, drainage amplification does not vary as would be expected from changing permafrost. As visible in figure 5.3 for pre-industrial times, the number of lakes decreases largely in southern central Canada in the warming scenarios because of the total loss of excess ice. The number of lakes increases in some regions of Alaska, Canada, and Siberia because more lakes develop. The climate scenarios also include changes in precipitation (as listed in Table 5.2 and shown in Fig. 5.1). In these areas, infiltration is less than 30 mm during May and below the threshold of infiltration disturbances. Due to larger precipitation infiltration increases above the threshold and more lakes are triggered. In the Canadian archipelago, the summer air temperature rises above 0 °C, which is the threshold for temperature disturbances. In the cooling scenario, the number of lakes increases in very warm permafrost regions, because ice can aggregate there. In other regions the number of lakes decreases, because the climate becomes too dry for infiltration disturbances. However, in some areas of the Canadian archipelago and the Laptev sea coast some areas become too cold for temperature disturbances.

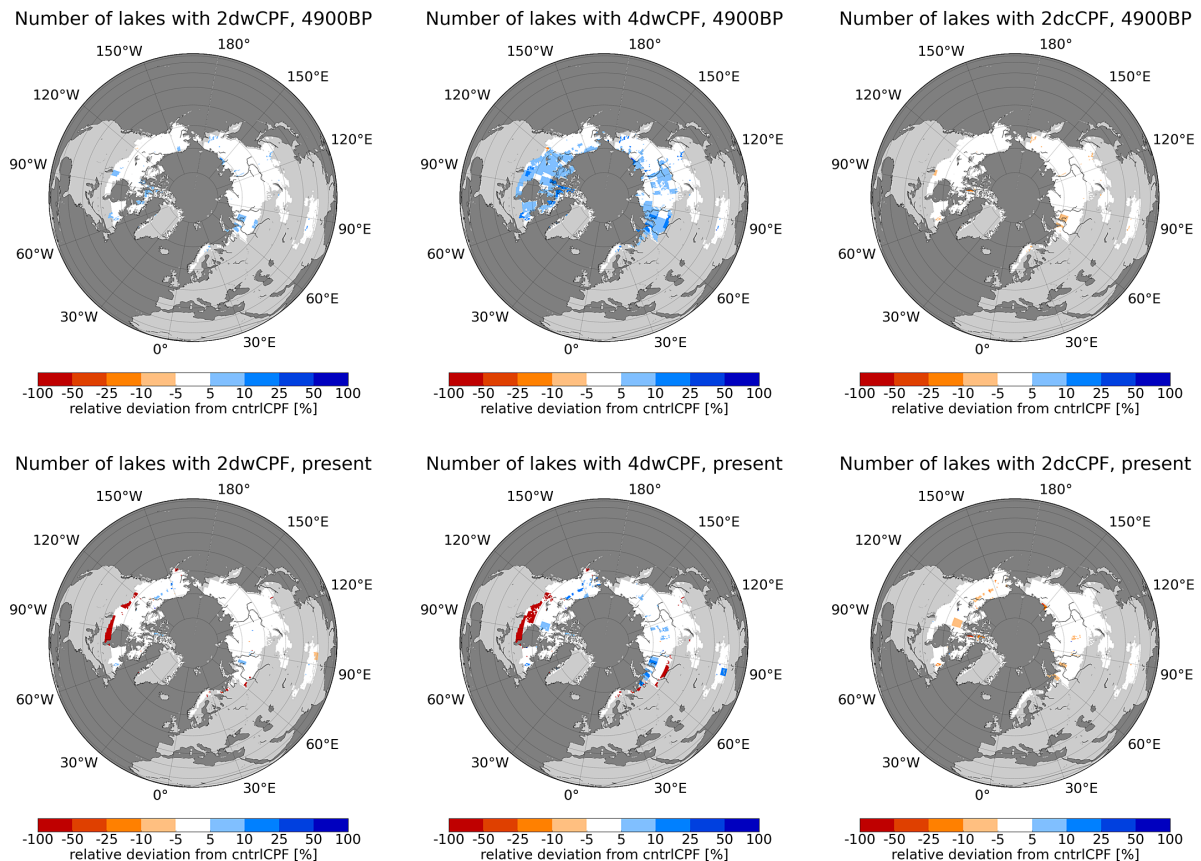


Figure 5.3: Relative change in number of lakes is respect to the cntrlCPF run at two time-steps: 4900 BP (upper panel) and pre-industrial times (lower panel). Three climate scenarios are investigated here: 2dwCPF (left), 4dwCPF (middle), and 2dcCPF (right).

TAL is similar in all scenarios for the first 500 years, i.e. 5000 - 4500 BP (see Fig. 5.2). Within

this period TAL decreases slightly. This reduction relates to a regional phenomenon. Between 4750 BC and 4700 BC in the Hudson Bay lowlands, an exceptionally large number of lakes drains resulting in a reduction of the water covered area. A peak of new lakes forms there some centuries before 5000 BP during the spin-up period of the TAPAS model. Thus, this change within TAL relates to uncertainties due to spin-up.

TAL develops differently from TNL in the climate scenarios after 4500 BP. In the *cntrlCPF* run and in the cooling scenario, it increases until 3200 BP and decreases again afterwards. However, these changes are very small. TAL decreases by 1 % between 5000 BP and pre-industrial times and no correlation exists between temperature and TAL probably due to the small variability. A larger decline of TAL is observed in the warming scenarios. Between 5000 BP and pre-industrial times, TAL decreases by 6.2 % and 10.3 %, respectively (as listed in Table 5.3). The decline relates to loss of excess-ice in warm permafrost regions. Ice accumulates if the annual mean air temperature drops below -1 °C. Due to climate warming, the southern boundary of ice formation shifts northward. As it is visible for the scenario *2dwCPF* in figure 5.2, TAL increases in the first 800 - 1100 years after the climate change due to expansion of the peak of new lakes and decreases in the period afterwards. In these model runs old excess ice from the period before the warming remains. Firstly, TKL develop in regions with the largest ice depth. These lakes can reach a larger area, than lakes of later generations because less excess-ice is available for them. Therefore, more water area is lost due to drainage of TKL than gained by new lakes. TAL decreases strongly until 1800 BP, in both warming scenarios. Then, TAL develops equally in all scenarios until pre-industrial times. This means, that the difference of TAL between the two scenarios remains constant.

Figure 5.4 shows the differences in water covered area between scenarios and the *cntrlCPF* run at pre-industrial times. In the *2dcCPF* scenario, TAL is 1.8 % smaller than in the *cntrlCPF* run at pre-industrial times, because temperature and precipitation are decreasing. Therefore, in some regions, summer temperature and infiltration during May fall below the thresholds for disturbance events. Some areas of the Canadian archipelago and of the Laptev Sea coast become too cold for temperature disturbances, while the other regions with decreasing lake area become too dry for infiltration disturbances. In some regions TAL increases, because the region of ice accumulation moves southward in America and Asia and westward in western Siberia. However, this effect is not fully visible in figures 5.3 and 5.4, because PF does not increase. For *2dwCPF*, lake area decreases in southern parts of central Canada and western Siberia, because no ice accumulates. In other parts, it increases slightly due to higher infiltration. For *4dwCPF*, lake area changes over larger areas. It increases around the Lena river, northern parts of western Siberia, northern central Canada, and in Alaska.

These assumptions are based on long term means of infiltration and temperature records as derived from CLIMBA (Bruecher et al., 2014). Higher precipitation leads to larger infiltration. The disturbance threshold is set to 30 mm. I assume that this threshold is passed in regions with slightly less infiltration. Therefore, more lakes are triggered by a higher number of disturbances.

Overall, TNL develop equally in all scenarios after 3100 BP and TAL after 1800 BP. The peak in the enhanced number of triggered TKL due to warming is visible for about 900 years. The number of lakes reduces due to drainage, which controls the life-time of individual lakes. It also reduces if no new ice accumulates and all regions with old excess-ice are thawed. The climate signal is visible on changes in excess-ice formation for 1900 years (not shown here). Lake area changes are more complex to explain than lake number changes. With constant PF, lake area

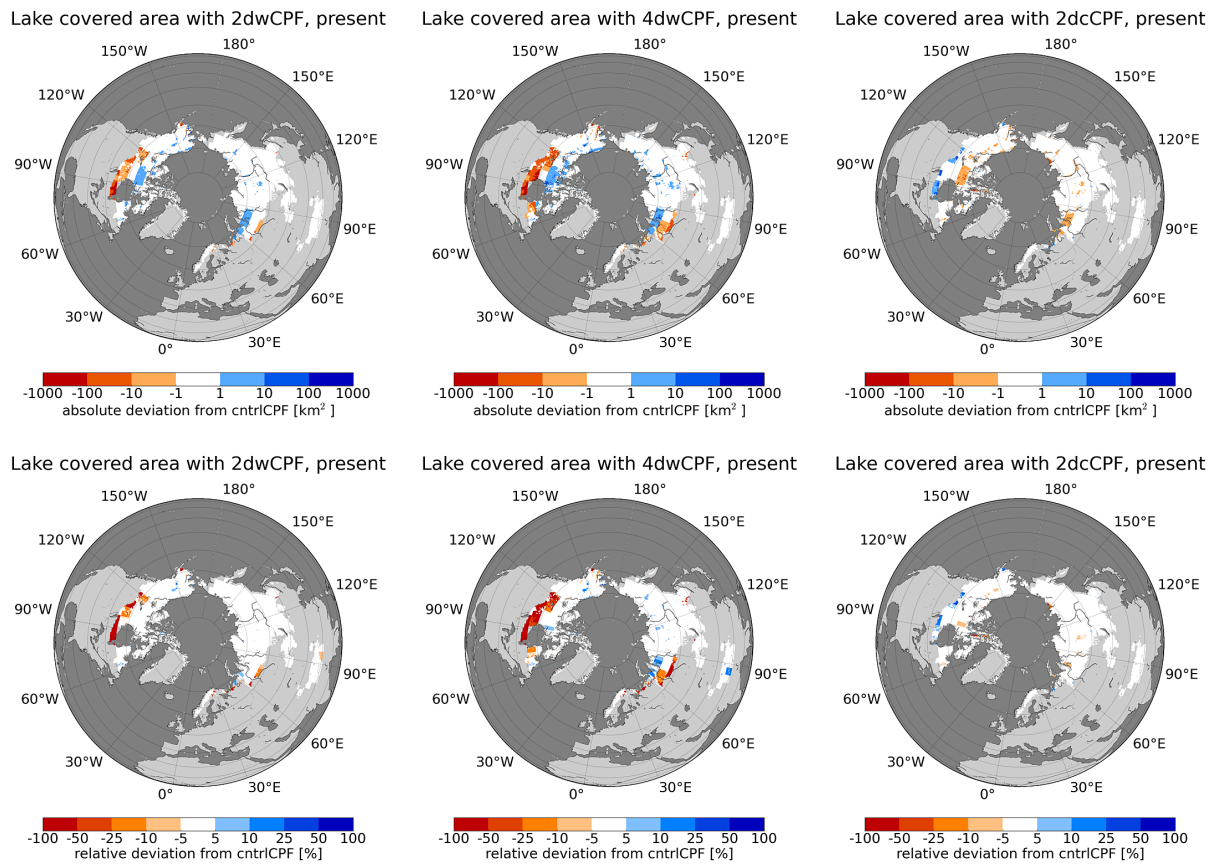


Figure 5.4: Area covered with lakes in comparison to the cntrlCPF run for different climate scenarios: 2dwCPF (left), 4dwCPF (middle), and 2dcCPF (right). Upper panel shows absolute difference and lower panel relative difference.

depends on the depth of accumulated excess-ice in the soil and on the number of triggered TKL. A different ice aggregation rate influences the lake area for 3200 years. This time is a result of two processes interacting with each other. All soils either with lakes or basins at the top need to adjust to the new equilibrium ice depth. First, ice is removed from all basins due to formation and expansion of TKL. The time-scale of this process depends on the number of expanding lakes and on the total area of drained basins. The expansion rate increases with the age of individual lakes, but is constant over time for lakes of the same age. Second, all lakes on soils with the old ice-depth have to drain. The time until drainage depends on drainage probability and is about 900 years. In the drained basins, ice aggregates towards the new equilibrium ice-depth until they are affected by thermokarst again. The average ice content changes until 3100 BP. Lakes which are triggered at that time reach a different size than older lakes. Therefore, TAL decreases further until 1800 BP.

Is the difference statistically significant from zero? To test this, the one sample t-test is applied to test the null-hypothesis. The probability to falsely reject the null-hypothesis is smaller than 10^{-23} for TNL and TAL in each climate scenario. This proves, that the chronology of the difference between the scenarios and the cntrlCPF run is significantly different from zero.

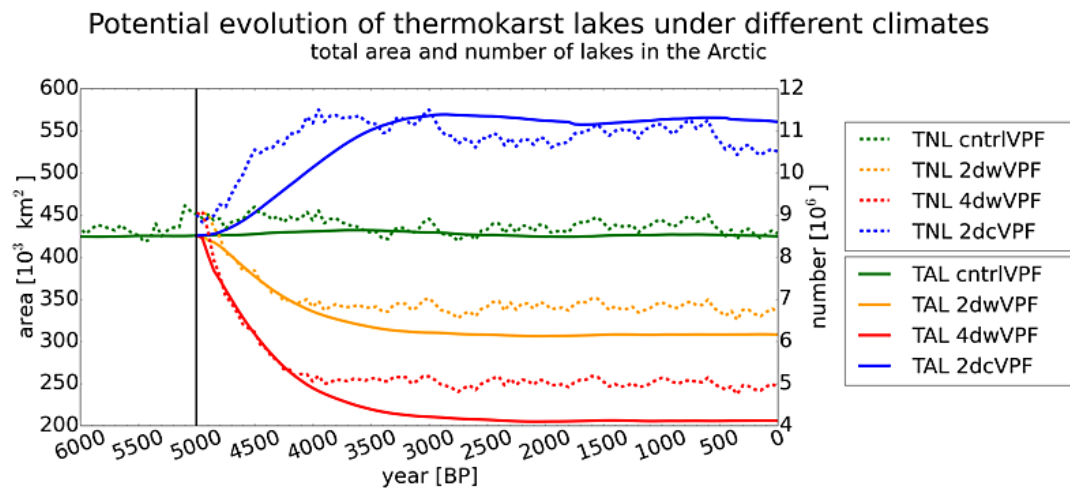


Figure 5.5: This figure shows time series of total number and total area of lakes in the Arctic including PF changes for the past 6000 years. The control run (cntrlVPF) is driven by CLIMBA forcing data, while the scenarios include different magnitudes of climate change between 5000 BP and 4900 BP applied to the CLIMBA data.

5.3 Thermokarst distribution under different climates with interactive permafrost

Measure	Year	cntrlVPF [%]	2dwVPF [%]	4dwVPF [%]	2dcVPF [%]
TNL	4950 BP	-0.89	0.32	0.86	-2.01
TNL	4900 BP	0.00	0.20	-4.33	-0.87
TNL	pre-industrial	-4.95	-25.55	-45.41	16.57
TAL	4950 BP	0.02	-0.01	-0.66	0.04
TAL	4900 BP	0.07	-1.33	-5.43	0.20
TAL	pre-industrial	-0.20	-27.60	-51.64	31.75

Table 5.4: This table lists changes of TNL and TAL relative to time-step 5000 BP at three different time steps: 4950 BP, 4900 BP, and pre-industrial times. The control run (cntrlVPF) is driven by CLIMBA forcing data, while the scenarios include different magnitudes of climate change between 5000 BP and 4900 BP applied to the CLIMBA data.

This section focuses on changes in distribution of TKL after different magnitudes of climate change. The same scenarios are applied as in section 5.2, but changes in PF are included into the TAPAS model. Here, permafrost responds to climate change. Therefore, the drainage probability of lakes changes over time. If PF decreases then one stabilizing factor is lost and, therefore, drainage of lakes increases. Furthermore, new landscapes can be affected by thermokarst if permafrost expands.

How do TAL and TNL evolve over time after different magnitudes of climate change? Which long-term changes can be expected within the distribution of TKL in the Arctic? As explained in section 5.1, three climate scenarios are defined with different magnitudes of climate change

during the 100-year period 5000 BP and 4900 BP (see Fig. 5.1). Which equilibrium states are reached within the distribution of LF and IC at pre-industrial times?

As expected, TAL and TNL decrease within the warming scenarios and increase in the cooling scenario (see Fig. 5.5). Warming leads to decreasing PF, which increases the drainage probability of lakes (Smith et al., 2005). One stabilizing factor is lost and, therefore, drainage of lakes increases. Some lakes may continue to exist if permafrost disappears, but then they evolve differently than TKL and probably turn into wetlands. In some regions permafrost disappears completely and all excess-ice is melted. In this case, the TAPAS model simulates a complete drainage of TKL. Therefore, TAL and TNL decrease if PF decreases. In the cooling scenario, PF increases and new regions are underlain with permafrost. Excess-ice aggregates there and a higher number of lakes develops.

Actually, TNL is higher in the cntrlVPF run than cntrlCPF run, while TAL is smaller (compare figures 5.2 and 5.5). If changes in PF are included into the TAPAS model, TAL decreases from 435000 km² (cntrlCPF) to 425000 km² (cntrlVPF), while TNL increases from 8.2*10⁶ to 8.6*10⁶. The TAPAS model simulates a larger permafrost area, than is observed by NSIDC. PF is computed as a function of the annual mean air temperature only. In reality, snow reduces PF, because it isolates the soil from air during winter (as discussed in Sect. 3.2.2). The isolation effect of snow is not considered, because its implementation worsened the modelled PF in large parts of central and eastern Siberia (see Sect. 2.2.1). However, more lakes can develop, because PF is too high. Furthermore, variations within PF alter the drainage probability of lakes. Decreasing PF leads to instabilities within the ground and more lakes are drained. Variations within PF lead to temporally larger drainage probability during periods of warming. Temporarily, more lakes drain and less likely reach larger areas. Therefore, TAL is smaller in the cntrlVPF run than in the cntrlCPF run.

In the warming scenarios TNL increases until about 4950 BP. Then, TNL quickly drops below TNL of the cntrlVPF run even though more lakes are triggered. The gradient is steeper in the 4dwVPF scenario than in the 2dwVPF scenario. PF decreases and enhances drainage of lakes. Additionally, large areas do not contain permafrost any more after the first century. All lakes are drained there. This explains the steep decreases during the first centuries after climate change. After 3900 BP, TNL varies equally in all scenarios but with different magnitudes (see Fig. 5.5). Thus, in all scenarios, a time period of about 900 years is needed to adjust to a new equilibrium state between formation and drainage of lakes. This is the same time-scale as that of the drainage of newly triggered lakes in the scenarios with constant PF (see Sect.5.2). Contrary to the scenarios with constant PF, basins with aggregated ice from the time period before warming are thawed, if the annual mean air temperature increases. If temperature rises above -1 °C, PF decreases below 10 %. A lower PF threshold of 10 % is implemented into the TAPAS model. If PF decreases below this threshold then the model does not simulate thermokarst.

Variations within PF slightly increase the temporal variability of TNL. For example, in the cntrlCPF run, TNL varies between 8.1 and 7.6 million during the period 4000 BP and 3000 BP. Whereas, in the cntrlVPF run, TNL varies between 9.1 and 8.4 million. This relates to variations within the drainage of lakes.

TAL adjusts to the new climate state over a longer time period than TNL. In the cooling scenario TAL increases, because larger areas are underlain with permafrost, which can be affected

by thermokarst. In the model, ice aggregates in drained basins over up to 1600 years as a function of ice deficit relative to a maximum ice depth. The maximum ice depth changes with ALD which depends on temperature.

In the warming scenarios less excess-ice aggregates in new drained basins than in older basins. TKL develop there, after all older basins have been affected by thermokarst. These lakes reach a smaller size because less excess-ice is available. The effect of altered excess-ice conditions on the area covered with lakes is small, but increases over time. It takes about 900 years until all older lakes have drained. Therefore, TAL decreases over a longer time period than TNL.

In the warming scenarios PF reduces and fewer areas are available for thermokarst. Therefore, more lakes drain and less ice aggregates. TAL is smaller in the 4dwVPF scenario than in the 2dwVPF scenario. The difference of modelled TAL between the climate scenarios and cntrlVPF increases until 2800 BP and remains constant until pre-industrial times (see Fig. 5.5).

To conclude, it takes 2200 years for the model to adjust to the new climate state. This is a shorter time period than it is obtained from the model runs with constant PF. The reason is explained on the basis of the results of the 2dwVPF scenario. Permafrost disappears from larger areas within the first century of warming. PF decreases and basins with a high amount of excess-ice are already thawed and melted. In the version with constant PF (2dwCPF), these basins thaw after they are affected by thermokarst. Reduction in PF is a faster process of thawing than expansion and formation of TKL. Therefore, the lakes area reaches equilibrium faster in the climate scenarios with variable PF than in the scenarios with constant PF.

5.3.1 Lake fraction under different climates at pre-industrial times

The last part of this section focuses on distribution of modelled lake fraction (LF) and ice content (IC) at pre-industrial times. What changes can be expected from different magnitudes of climate changes after 5000 years? Are changes in modelled LF significantly different between the climate scenarios?

Large LF is modelled in northern part of Quebec, central Canada, Alaska north slope, eastern Siberian lowlands, Lena river delta, northern Siberia, and in eastern parts of western Siberian lowlands (see Fig. 5.6). Most regions with high fraction of TKL are located between 65°N and 75°N, which is confirmed by various field studies (Grosse et al., 2013). In these regions, large changes can be expected as a result of climate change. Figure 5.6 shows lake fraction as modelled under different climates scenarios at pre-industrial times. Note, that all regions with PF of less than 10 % are masked.

LF decreases in the 2dwVPF scenario in comparison to the cntrlVPF in large regions of the periglacial Arctic. This is mainly due to reduced PF, which leads to thawing of ice-rich basins and increasing drainage of lakes. ALD increases and excess-ice reaches a smaller depth and TKL reach a smaller surface area. In other regions LF is the same as in the cntrlVPF run. There, all soils are underlain with permafrost. Since the peak of triggered lakes has already drained until pre-industrial times, TAL and TNL develop similar because lakes are only triggered by anomalous events with respect to the past 30-year running mean.

As expected, the response to the 4dwVPF scenario is larger than to a warming of 2 °C, because PF reduces to a larger magnitude. LF does not change in northern Siberia, in eastern Siberian

lowlands west of 150°E, and in the Canadian archipelago. A higher LF was expected for the Canadian archipelago, Greenland, and in Svalbard, because the summer temperature increases above 0 °C. Higher temperature and larger precipitation increase summer temperature and infiltration, respectively. Therefore, some arid and cold regions can be affected by thermokarst, because thresholds for disturbances are passed. However, LF does not increase, because the slope is too high for aggregation of excess ice there. It measures $0.04 \tan \alpha$ or 2.29° (see Fig. 3.3 and 6.6) and excess-ice accumulates in areas with a slope of up to 2° . Infiltration thresholds are passed in eastern Siberian lowlands, in central Alaska, and in parts of central Canada. However, LF reduces because PF decreases.

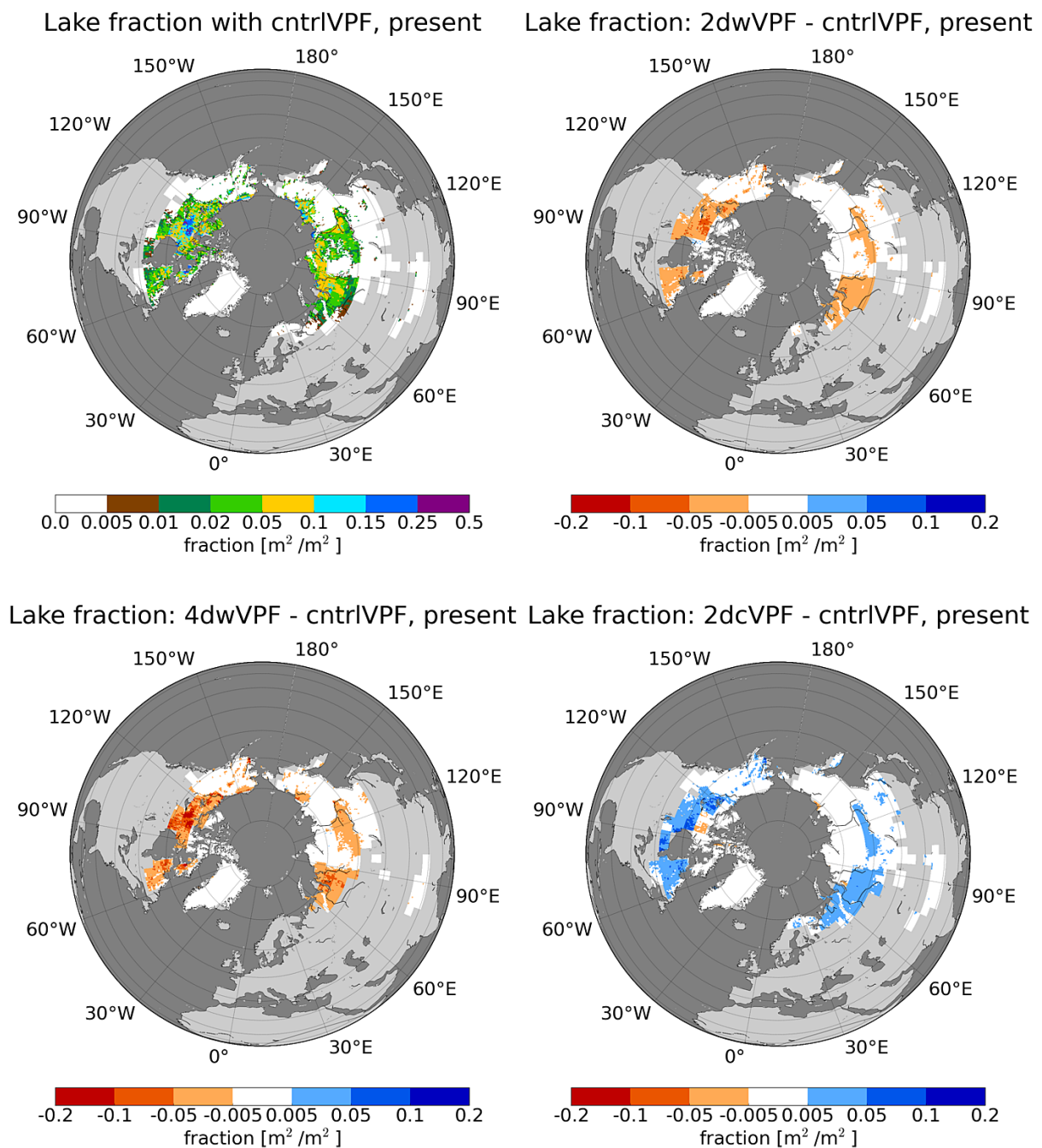


Figure 5.6: This figure shows the modelled lake fraction with cntrlVPF (upper left) in comparison to different climate scenarios: 2dwVPF scenario (upper right), 4dwVPF (lower left), and 2dcVPF (lower right). The results show lake fraction and absolute differences at pre-industrial times.

In the cooling scenario, many Arctic regions show higher LF than the cntrlVPF run. PF increases and permafrost expands southward in Russia and Canada and also develops in Scandinavia. Excess-ice accumulates on larger areas and allows formation of more TKL (see Fig 5.6). The ice content increases, because ALD grows and excess-ice features reach a larger size. Lakes developing on soils with higher IC reach larger areas. LF decreases at the Laptev sea coast at 150°E and in northern parts of central Canada including some areas of the Canadian archipelago. The long term averages of summer temperature and infiltration measured are settled around the thresholds for temperature and infiltration disturbances. In the cooling scenario, these regions become too cold or too dry for thermokarst.

Is the TAPAS model sensitive to climate change? The one sample t-test is applied to the time series of TAL and TNL. The climate scenarios are compared with the cntrlVPF run. The modelled variables TAL and TNL are different, if the differences are significantly larger than zero. 6 difference plots can be made, three for TNL and three for TAL. As it is obvious in figure 5.5, the modelled TNLs and TALs are significantly different from each other on the 99.99999999 % level.

Did the distributions of LF and IC significantly change on long time scale? Are the equilibrium states of the climate scenarios significant different from the cntrlVPF run? This significance is tested with the two-sample Kolmogorov–Smirnov test. The modelled LF of each model run is clustered in 0.01 m²/m² intervals. A CDF is performed for the 2dwVPF, 4dwVPF, and 2dcVPF scenarios and for the cntrlVPF run. The CDFs of almost all scenarios are significantly different from each other on the 99 % level. One exception exists for the CDFs of the CLIMBA run and the 2dcVPF scenario. They are significantly different on the 95 % level.

The same method is applied to the distributions of IC. The IC of each scenario is clustered in 0.01 m/m intervals and sorted to a cumulative distribution function. The CDF of each scenario is compared to the CDF of another scenario. The cntrlVPF modelled IC is significantly different from the 4dwVPF scenario on the 99 % level, while it is not significantly different from the other scenarios. The CDFs of the 2dwVPF and the 2dcVPF scenario are different from that of the cntrlVPF scenario, but the influence on the CDFs is quite small. Within the 4dwVPF scenario, IC is significantly different from all other scenarios at the 99 % level. Evaluation of modelled IC against observed IC from NSIDC is difficult because the data is not available in sequential form but only in categorized form.

6 Uncertainty of thermokarst evolution during the Holocene to different forcing

In this chapter I investigate the sensitivity of the TAPAS model to different forcing and estimates potential evolution of thermokarst during the past 6000 years. Two different model runs are available, which simulate natural climate variability during the last 6000 years of the Holocene. These are CLIMBA (Bruecher et al., 2014) and ECHAM5/JSBACH/MPIOM (Fischer and Jungclaus, 2010), which are alternately used as forcing of the TAPAS model. Here, ECHAM5/JSBACH/MPIOM forcing is simply referred to as the ECHAM5 forcing.

Climate models can not represent the full physics of reality. Each model provides a general sketch of reality and simulates physical processes differently. As an example, CLIMBA regards the carbon-cycle and simulates changes in atmospheric CO₂ concentration, while ECHAM5 computes with a fixed CO₂ concentration. Therefore, warming and cooling periods of the last 6000 years are probably differently sketched by ECHAM5 and CLIMBA. Also different climate states are reached at pre-industrial times. Therefore, a different equilibrium state between modelled lake fraction (LF) and ice content (IC) can be expected, if a different forcing is applied. Are the differences significantly different from each other? What is the quality of modelled lake fraction (LF) and ice content (IC) in comparison to observations from ESACCI and NSIDC, respectively?

This chapter consists of four parts. First, the models ECHAM5 and CLIMBA are described. What is the set-up of the models and which processes are included? An overview is given, of which forcing data are used and how they are prepared for the application within the TAPAS model. Second, the natural climate variability of the past 6000 years is described in detail. Which differences are visible within modelled periods of warming and cooling? Third, the temporal evolutions of the total area of lakes (TAL) and of the total number of lakes (TNL) are discussed. Which differences are visible due to differences in modelled climate variability? How has thermokarst potentially developed during the Holocene? Fourth, the distribution of modelled TKL is investigated. Regions with large discrepancies between modelled and observed TKL are investigated. Which processes are responsible for the discrepancies?

6.1 Forcing of the TAPAS model

The TAPAS model is driven once by the CLIMBA forcing and a second time by the ECHAM5 forcing. Both forcing datasets are provided on a Gaussian grid with a resolution of 3.75° longitude and 3.75° latitude (T31-grid). CLIMBA provides monthly mean data between 8000 BP and pre-industrial times. ECHAM5 provides daily and monthly means between 6000 BP and pre-industrial times. The TAPAS model runs on a yearly time-step and applies monthly mean data to determine number of disturbances (Sect. 3.1), excess-ice depth (3.5), and permafrost fraction (Sect. 3.2).

A short overview is given here, which forcing variables are applied for which processes. ECHAM5 and CLIMBA both provide temperature, snow, precipitation, snow-melt, runoff, drainage. These data are used to determine the number of disturbances and triggered TKL due to summer temperature, winter snow depth, and infiltration. Temperature is applied to estimate PF and as a threshold for excess-ice aggregation. Soil temperature and burned area fraction are solely provided by CLIMBA. ECHAM5 does not simulate wildfires and the burned area fraction. Therefore, the number of disturbances due to wildfires is not computed in this study. ECHAM5 also does not provide soil temperature. Soil temperature is crucial for simulating excess-ice formation. The active layer depth (ALD), which is the maximum thaw depth, defines the maximum excess-ice depth. Excess-ice accumulation is limited by the available liquid water within the soil, which is a function of soil temperature and soil moisture. Therefore, soil-temperature needs to be estimated for ECHAM5. It is derived from air temperature based on a simple study of the average deviation of soil temperature from air temperature in CLIMBA. A 1000-year monthly mean difference between air-temperature and soil temperature is computed for each month, grid-cell, and soil layer. Then, the climatological mean differences are applied on ECHAM5 forcing for each month of the modelled time period.

The climate forcing data are provided on a T31-grid and remapped on a 0.5° longitude and 0.5° latitude grid with the nearest neighbour method (as explained in Sect. 4.0). The TAPAS model can run at that grid scale, because slope data is available on 0.5° grid. Slope is applied to limit formation of TKL and accumulation of excess-ice.

The simulation of thermokarst spans a period of 6000 years starting in the mid-Holocene at 6000 BP. Two restart files are generated as initial condition for the TAPAS model: one for the CLIMBA-run and one for the ECHAM5-run. The TAPAS model is run with the data for the first 500 years of the simulation time period. Application of the corresponding forcing data is repeated until an equilibrium state is reached between lake formation, drainage, and excess-ice accumulation.

ECHAM5/JSBACH/MPIOM is a coupled atmosphere - ocean - sea-ice - biosphere general circulation model. The model consists of the spectral atmosphere model ECHAM5 (Roeckner et al., 2003) run on a horizontal resolution of $3.75^\circ \times 3.75^\circ$ with 19 vertical hybrid sigma pressure levels. ECHAM5 is combined with the land surface model JSBACH, which includes a dynamic vegetation module (Raddatz et al., 2007; Brovkin et al., 2009). ECHAM5 is coupled to the general circulation ocean model MPI-OM ((Marsland et al., 2003), which includes a thermodynamic sea-ice model. The coupling time-step between atmosphere and ocean model is 24 hours. In the experiment from Fischer and Jungclaus (2010) the greenhouse gas concentrations are set to pre-industrial values (e.g. $\text{CO}_2=280$ ppm). ECHAM5 is only forced by changes in

insulation due to changes in orbital parameters, which are applied to estimate regional effects of changes within the orbital forcing on atmosphere and ocean circulation and heat transports during the last 6000 years of the Holocene. Changes in insulation influence the climate indirectly through feedback mechanisms, which alter atmosphere and ocean dynamics and meridional heat and moisture transfers (Fischer and Jungclaus, 2010).

CLIMBA is a coupled climate-carbon cycle model. In contrary to ECHAM5, CLIMBA also includes an interactive carbon cycle (Bruecher et al., 2014). It combines JSBACH, the land component of the Earth system model MPI-ESM (Reick et al., 2013; Brovkin et al., 2009; Raddatz et al., 2007), with the intermediate complexity Earth System model CLIMBER-2 (Petoukhov et al., 2000; Ganopolski et al., 2001). JSBACH runs offline for one model-year and simulates daily variations of the land carbon stocks. This includes a dynamic vegetation scheme and disturbances of the vegetation by natural fire occurrence. Changes in the land carbon stocks are addressed to CLIMBER-2 as carbon flux into the atmosphere. CLIMBER-2 estimates changes in temperature, precipitation, radiation balance, and atmospheric CO₂ concentration. These variables are then passed to JSBACH to compute the following simulation year. The coupling scheme closes the carbon cycle and allows accounting for bio-geophysical feedbacks of burned area fraction (Bruecher et al., 2014; Brovkin et al., 2002).

However, CLIMBER-2 simulates land and atmosphere processes at a very coarse resolution of 51° longitude by 10° latitude. JSBACH runs on a higher spatial resolution of 3.75° × 3.75° and provides better resolved daily dynamics of land processes. A base climate is applied to downscale climate anomalies simulated with CLIMBER-2 to JSBACH's resolution. Daily values of the 50-year period 1850 - 1899 are used as a base climate, these were derived from the MPI-ESM CMIP5 simulation. Climate anomalies of this period are related to anomalies computed with CLIMBER-2 during the same time-period. Thus, the climate of the Holocene is computed as anomalies from the 50-year period.

6.2 Climate of the past 6000 years

This section is focused on the climate variability of the last 6000 years of the Holocene. First, the climate is described as modelled in Fischer and Jungclaus (2010). Then, a short summary shows the main differences between CLIMBA and ECHAM5 within the permafrost regions. Generally, the high latitudes were warmer during mid-Holocene than at pre-industrial times, while the tropics and northern subtropics were cooler. Changes in orbital parameters alter the insulation distribution. The seasonal cycle is enhanced because the obliquity was higher and summer solstice was closer to perihelion.

The northern high latitudes received higher insulation during summer. Therefore, the temperature decreased in the Arctic from mid-Holocene until pre-industrial times. For instance, the Barents Sea and the east coast of Greenland have cooled by 3 °C. Large areas of Eurasian land areas north of 60°N cooled by about 1 °C (see Fig. 6.1). In comparison to Eurasia, the North American Arctic cooled by a smaller magnitude, except in the Canadian Archipelago and the North slope of Alaska.

The ocean-surface temperature decreased by about 2 °C over the past 6000 years. This relates to increasing sea-ice cover in the Arctic and changes in atmospheric and oceanic circulations

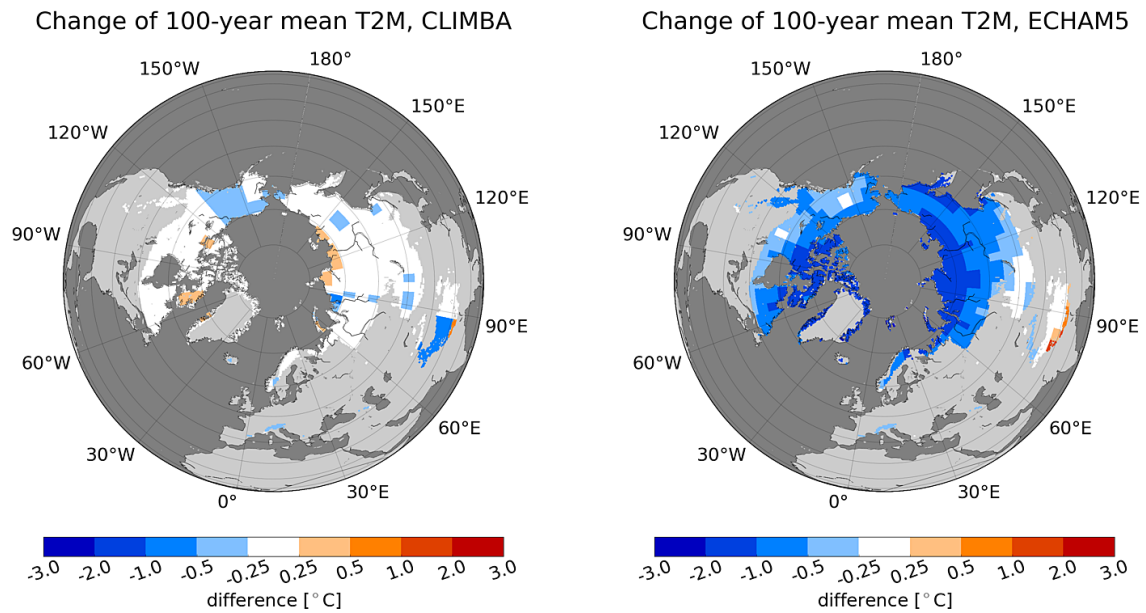


Figure 6.1: This figure shows the difference of annual mean temperature between the last 100 years and the mid-Holocene period 6000 - 5900 BP. Averages of 100-year periods are determined for CLIMBA (left panel) and ECHAM5 (right panel). The results are masked with NSIDC permafrost areas (Brown et al., 1998).

and heat transports. Therefore, the albedo increased over the Arctic ocean, especially over the Barents Shelf and on the east coast of Greenland. Also the Arctic lands experienced an increase of the surface albedo. The boreal tree line moved southward and the albedo increased in most parts of northern Siberia, Scandinavia, and northern north America.

As visible in figure 6.1, ECHAM5 shows colder temperature at pre-industrial times than at 6000 BP over Siberia, and north America and warmer temperatures over Tibet (ECHAM5). However, this relationship is less well pronounced in CLIMBA forcing and some regions like large parts of central Canada and western Tibet show differences in the opposite direction. During the Holocene, the Laptev Sea coast and northern Siberia have cooled by more than 1 °C in ECHAM5, while no cooling has been modelled by CLIMBA (Fig. 6.1).

While the CO₂ concentration remains constant in ECHAM5, it increases from 260 ppm to 272 ppm in CLIMBA (Bruecher et al., 2014), which probably counteracts the cooling effect due to changes in orbital parameters. Sharp boundaries are visible within the regional temperature differences. This may be related to the coarse grid ($51^\circ \times 10^\circ$) of CLIMBER-2 anomalies driving JSBACH (Bruecher et al., 2014). The grid spacing of CLIMBER-2 is well described in Petoukhov et al. (2000). Since the annual mean temperature governs the fraction of surface underlain permafrost, differences can be expected within modelled PF. This in turn may result in a different distribution of thermokarst lakes.

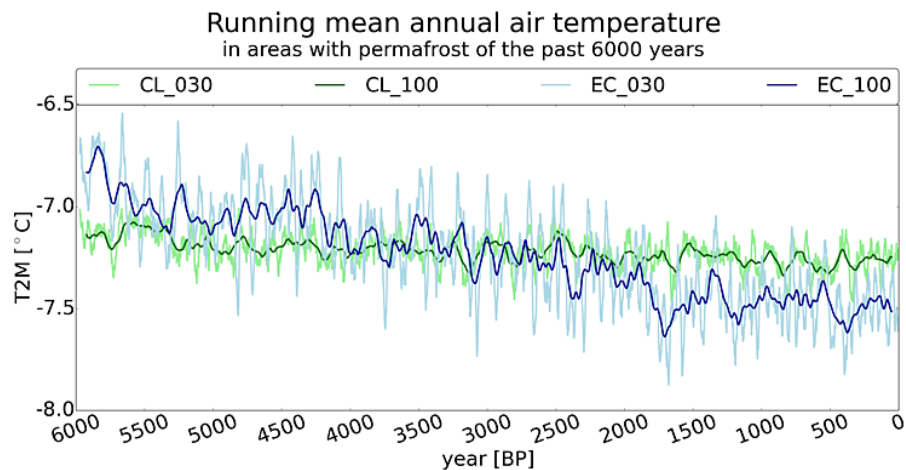


Figure 6.2: This figure shows time-series of annual mean temperature of all NSIDC permafrost regions (Brown et al., 1998) as it is modelled by ECHAM5 (here EC) and CLIMBA (here CL). 30-year and 100-year running means are shown here.

6.3 Potential thermokarst development of the past 6000 years

This section considers the temporal evolution of TAL and TNL. The modelled time-series of annual mean air temperature are discussed as well as the evolution of the different disturbance parameters: summer air temperature, winter snow depth, and infiltration.

The initial CO_2 at 6000 BP is larger in ECHAM5 than in CLIMBA. Therefore, the annual mean temperature of NSIDC permafrost areas is higher in ECHAM5 than in CLIMBA at the beginning of the time-series. Until pre-industrial times, the annual mean temperature decreased by 0.8°C in ECHAM5 and by 0.2°C in CLIMBA (see Fig. 6.1). Evolution of annual mean air temperature is modelled by ECHAM5 as following: Between 6000 BP and 5500 BP it decreased to -7°C and remained at that level until 4200 BP. Then until 1800, it decreases to -7.5°C (see Fig. 6.2). Temperature remained at that level until pre-industrial times. Thus, two periods of cooling are followed by two periods of rather stable climate. CLIMBA shows a smaller variability of the annual mean air temperature than ECHAM5 (see Fig. 6.2), but also shows cooling between 6000 BP and 4800 BP.

With ECHAM5 forcing, TAL increases from 5000 BP until 2800 BP. TAL starts to increase several centuries after the end of the first cooling period (see Fig. 6.3). About 2700 years are needed to adjust to a new equilibrium state. This is a longer time period than determined from the cooling scenario in section 5.3, where 2200 years are needed to adjust to a new equilibrium state (see Fig. 5.1). Short periods of warming and cooling may delay the time period for reaching a new equilibrium. Permafrost grows in areas due to cooling and expands southward. PF increases while ALD decreases. Therefore, more areas are available for accumulation of excess-ice and formation of TKL. Due to a smaller ALD excess-ice reaches a larger size. New lakes expand over larger areas because more ice is available for depletion. TAL increases again from 1800 BP

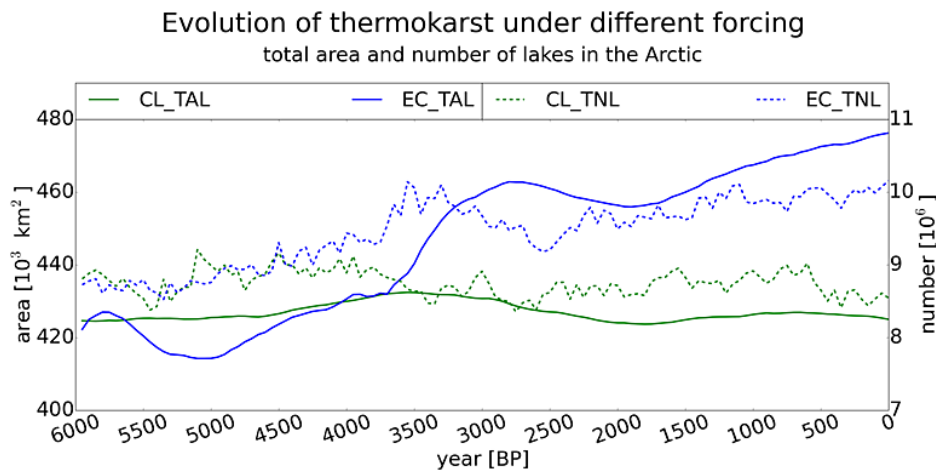


Figure 6.3: This figure shows the total number of thermokarst lakes and the total area covered by lakes for the model run with CLIMBA forcing in comparison to the model run with ECHAM5 forcing.

until pre-industrial times. From 6000 BP until pre-industrial times TAL increases by 12.8 % with the ECHAM5 forcing. With CLIMBA the forcing, TAL increases only by 0.1 %, because of the small cooling trend throughout the Holocene. A temporal maximum of TAL is visible at 3500 BP. This relates to the slight cooling in the beginning of the model time period.

TNL develops similarly with both forcing (CLIMBA and ECHAM5) until 3800 BP. Between 3800 BP and 3500 BP, TNL increases in the ECHAM5-run, while it decreases in the CLIMBA-run. The annual mean temperature increases by 0.4 °C, but there are several other time periods with a similar warming but without a large increase of TNL (see Fig. 6.2 and 6.3). Also the other climate parameters, which are applied for computing the number of disturbance events, do not show a significant signal. However, a peak of new lakes is triggered during this period. It drains in the following 900 years until 2600 BP (see Fig. 6.3). Between 2600 BP and pre-industrial times TNL develops similarly in both model runs, but TNL is larger in the ECHAM5-run than in the CLIMBA-run. ECHAM5 simulates a lower temperature than CLIMBA from 2500 BP until pre-industrial times (see Fig. 6.2). Therefore, PF is larger and more regions are underlain with permafrost. Excess-ice aggregates in more regions and a higher number of TKL develop. TAL increases as well in the ECHAM5-run and reaches a peak 800 years after the peak of TNL. It decreases again afterwards because many lakes are drained. Some centuries later, TAL increases again due to decreasing air temperature and increasing PF. In general, TNL increases by 16 % in the TAPAS model run with the ECHAM5 forcing and decreases by 3 % with the CLIMBA forcing.

To conclude, TAL and TNL increase with decreasing temperature and a large negative correlation exists for the model run with the ECHAM5 forcing. The Spearman rank correlation between TAL and temperature is -72 %, and between TNL and temperature -64 %. Contrary to ECHAM5, which simulates a cooling over the past 6000 years, CLIMBA simulates a much smaller temperature change. Therefore it is probably that, no significant correlation exists between temperature and TAL and between temperature and TNL in the model run with CLIMBA

forcing.

6.4 Modelled distribution of lakes at pre-industrial times

This section considers the distribution of thermokarst lakes at pre-industrial times. First, the modelled LF with the CLIMBA forcing is evaluated against the modelled LF with the ECHAM5 forcing. Then, the modelled LF with the CLIMBA forcing is evaluated against satellite based observations from ESACCI (Santoro et al., submitted).

6.4.1 Evaluation of model runs with ECHAM5 and CLIMBA forcing

The modelled LFs are quite similar and show a similar distribution of TKL (see Fig. 6.4). With ECHAM5 forcing, the TAPAS model simulates a larger LF in Alaska, eastern Siberian lowlands, the source region of the Lena river, Canadian archipelago, and also in northwestern Russia. In most parts more lakes are modelled. Therefore, TAL is larger than in the TAPAS model run with CLIMBA forcing (as visible in Fig. 6.3). One reason is that ECHAM5 shows a stronger cooling in the Arctic than CLIMBA (see Fig. 6.1). Due to colder air-temperature permafrost increases in area and a larger number of lakes can develop because more areas are available. This is the case in the western Siberian lowlands, northwestern Russia, in the source region of the Lena river, and in central and southern Alaska (see Fig. 6.4). (Permafrost is erroneously modelled in northwestern Russia and will be discussed below). However, in the other regions with higher LF, there is continuous permafrost in both TAPAS model runs and PF is not larger in any of them. Less excess-ice is modelled with ECHAM5 forcing than with CLIMBA forcing in the eastern Siberian lowlands, in parts of northern Siberia, and on the north slope of Alaska. There a different equilibrium state has developed between the formation of new lakes and drainage of lakes. A larger lake fraction develops due to a larger number of disturbances and, therefore, more excess-ice is melted.

In other regions like in central Canada, in Quebec, and along the Lena river LF is smaller if the TAPAS model is driven with ECHAM5 forcing. Different processes can lead to a decrease in LF. In central Canada, both IC and LF are smaller. Smaller ice content can be caused by a larger number of lakes which melt the excess ice, but this is not the case there because LF decreases as well. In principal, the area covered with TKL depends on PF, excess-ice depth, and slope. The slope can be disregarded because this study focuses on the same region. PF is the same in both model runs (see Fig. 6.5). The same area is available for lake formation. Therefore, LF is smaller because IC is smaller. Excess-ice is modelled in regions with an annual mean air temperature of less than -1°C (as explained in Sect. 3.3.5). This is not the reason for smaller IC because ECHAM5 and CLIMBA both show an annual mean air temperature of less than -5°C . Draining water is used for simulating accumulation of excess-ice, which is limited if not enough liquid water is available for ice formation. In central Canada, drainage is smaller in ECHAM5 forcing than in CLIMBA forcing. Therefore, less water is available for ice formation.

Along the Lena river, LF is smaller and IC higher. This probably relates to a smaller number

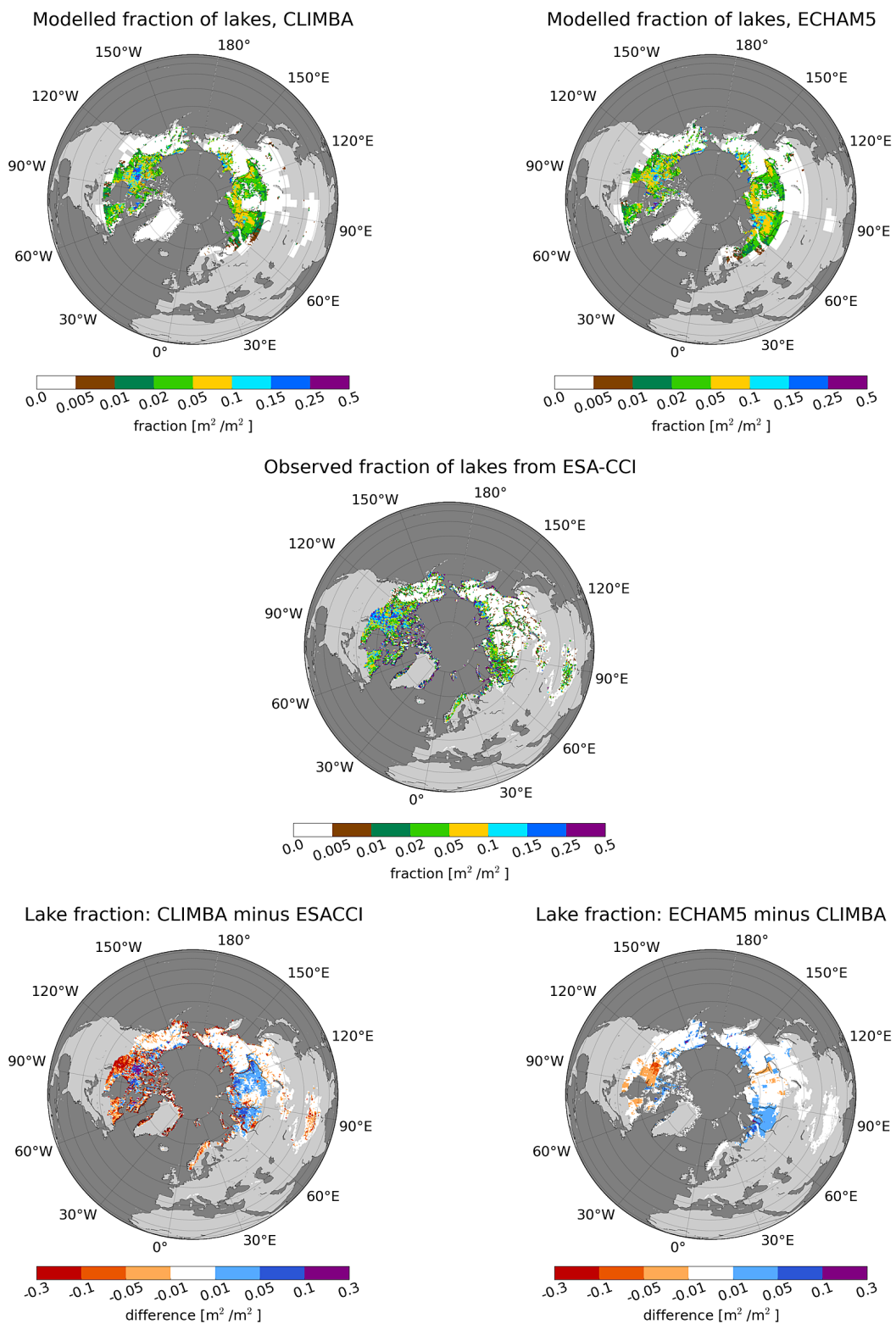


Figure 6.4: Simulated lake fraction at pre-industrial times simulated with CLIMBA forcing (upper left panel) and with ECHAM5 forcing (upper right panel) in comparison to ESACCI observations (Santoro et al., submitted) in NSIDC permafrost areas (Brown et al., 1998) (middle panel). Difference between CLIMBA and ESACCI (lower left panel) and the difference between ECHAM5 and CLIMBA (lower right panel).

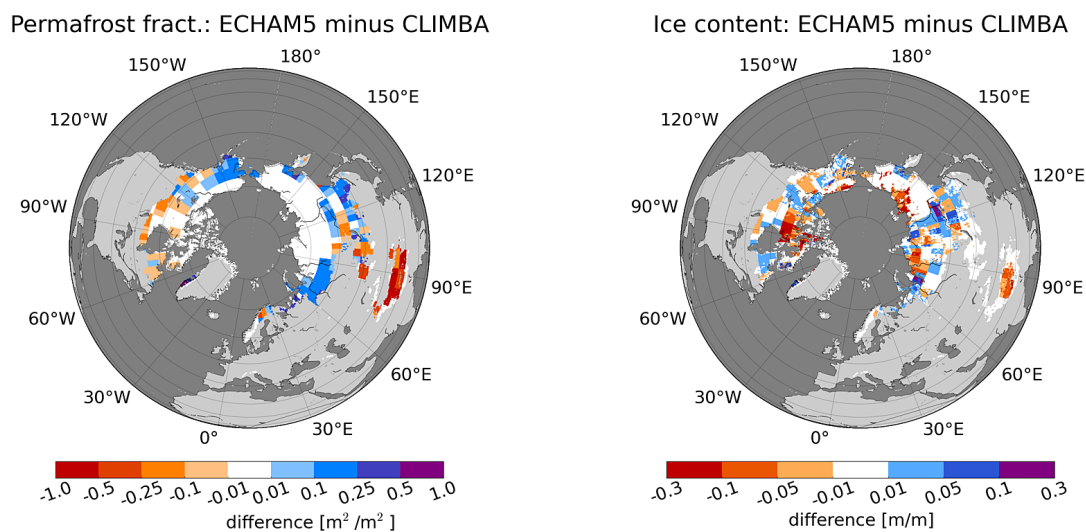


Figure 6.5: This figure shows modelled PF (left panel) and IC (right panel) with CLIMBA forcing in comparison to modelled PF and IC with ECHAM5 forcing. The regions are masked with NSIDC permafrost regions.

of TKL, which melt the excess-ice. Also in Quebec, a smaller LF is modelled with ECHAM5 forcing. This may be caused either by a smaller number of disturbance events or by a higher drainage. PF is smaller (see Fig. 6.5) and less lakes are present in Quebec due to the larger drainage probability of lakes. Therefore, less ice is melted and IC increases. However, the active layer depth increases if PF decreases due to a higher soil-temperature. Excess-ice reaches a smaller depth and, therefore, IC usually decreases if PF is smaller like in southern central Canada and in Tibet. Probably, less melting due to a smaller number of TKL counteracts a smaller excess-ice depth in Quebec. In comparison, this is not the case in southern Canada.

In Tibet, IC and PF are much smaller in the TAPAS model run with ECHAM5 forcing than with CLIMBA forcing (see Fig. 6.5). PF is computed as a function of annual mean air temperature (see Eqn. 3.17). ECHAM5 shows warmer annual means than CLIMBA at pre-industrial times. Therefore, PF is smaller and fewer areas are available for aggregation of excess-ice and formation of thermokarst lakes. LF is not severely affected because the TAPAS model cannot produce the observed LF there (see Fig. 6.4), as described in section 6.4.2.

6.4.2 Evaluation against satellite based observations

As visible in figure 6.4, the TAPAS model simulates too small LF in mountainous regions like in Tibet, in the Brooks Range (Alaska), in eastern Siberian mountains, and in southern Siberian mountains. This has several reasons. ESACCI observes all types of water bodies including topographic lakes, glacier lakes, rivers, and thermokarst lakes. For example in the Brooks Range, there are no TKL (G. Grosse, 2014, pers. comm.). In Tibet, there might be TKL because the region consists of high plateaus and large valleys. Flat areas are available for aggregation of excess-ice and formation of TKL. The TAPAS model applies mean topographic slope on a

0.5° grid as derived from the GTOPO30 data set by Stacke and Hagemann (2012). A slope dependent limitation function is applied to reduce aggregation of excess-ice in mountainous areas. Excess-ice aggregates in areas with a slope of up to 0.035 m/m or 2.0° (as discussed in Sect. 3.3.5). In most parts of Tibet and the eastern Siberian mountains, the mean slope is above 0.04 m/m. Therefore, the TAPAS model does not model the observed IC there (see Fig. 6.6). Considerably less lakes are modelled by TAPAS than observed by ESACCI in the southern part of central Canada. There most lakes are not formed due to thermokarst (Grosse et al., 2013). Glaciers of the last glacial period have carved out hollows in the barren ground, which are now filled with water now. Satellites cannot distinguish between the origins of different lakes. They just see black water bodies. The modelled excess-ice content and permafrost fraction coincide with observations.

Too many lakes are modelled by TAPAS in western Siberian lowlands and in central Siberia. Maybe modelled PF exceeds observed PF from NSIDC. A larger permafrost area could explain the positive bias in LF. However, modelled regions with continuous and discontinuous permafrost agree with observations from NSIDC within the experimental error. As it is visible in figure 6.7, too much permafrost is modelled in northwestern Russia, in Quebec, and at the southern edges of permafrost region in Asia. PF is computed as a function of annual mean air temperature only. Snow influences PF due to isolation of soil against atmosphere during winter, as discussed in section 3.2.1. However, PF would become too small in large parts of Siberia, if snow is considered.

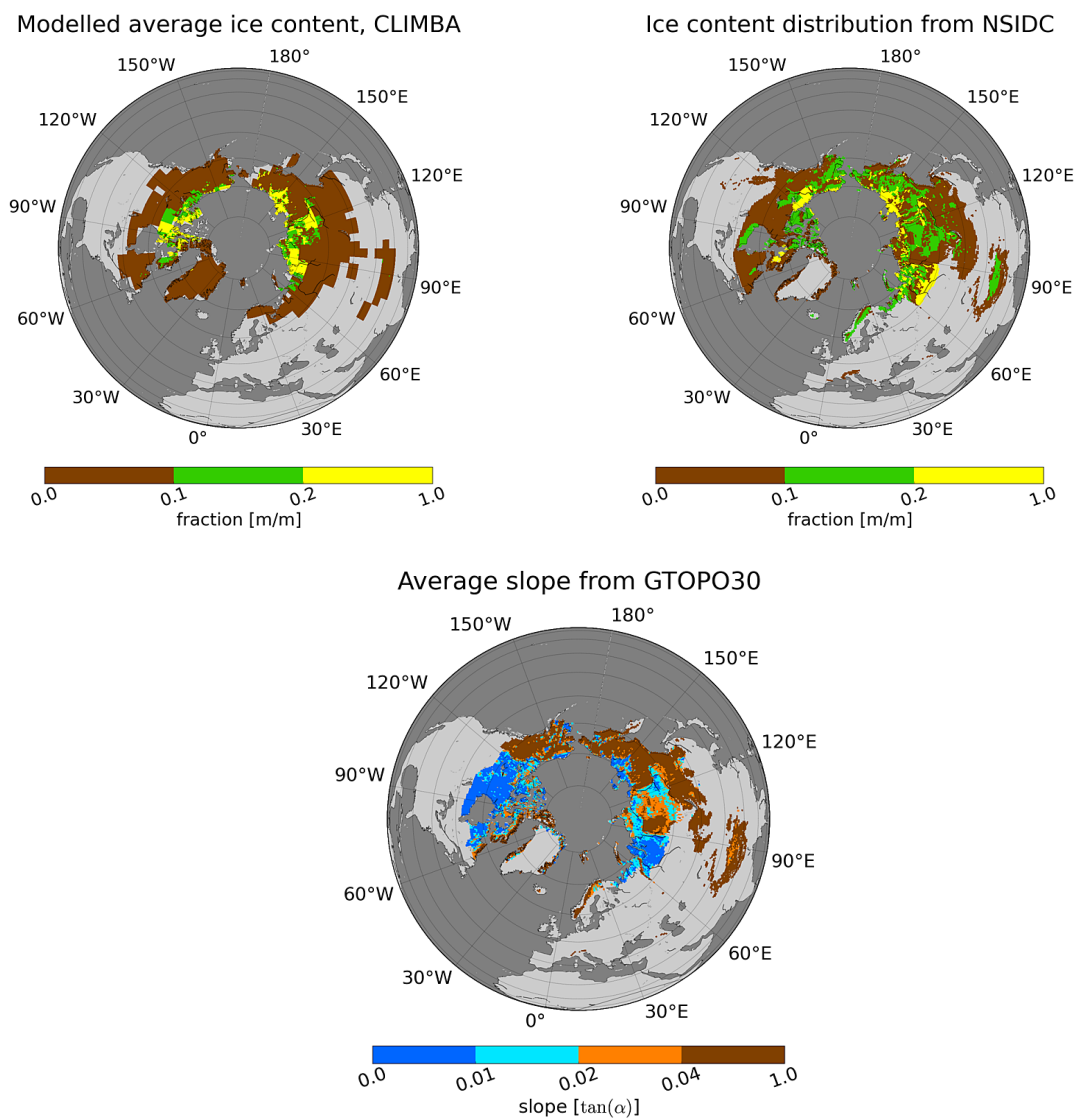


Figure 6.6: This figure shows modelled ice content with CLIMBA forcing (upper left panel), observed ice content from NSIDC (Brown et al., 1998) (upper right), and mean slope (Stacke and Hagemann, 2012) (lower panel).

Generally, the regions of western Siberia and central Siberia are lowlands with a slope of less than 0.02 m/m in central Siberia and less than 0.01 m/m in western Siberia. Aggregation of excess-ice is not severely limited by slope. Nevertheless, too small IC is modelled in most parts of these regions in comparison to observations (see Fig. 6.6). Too many lakes are formed there and thaw too large a permafrost area and melt the excess-ice. Therefore, IC is too low. Too many lakes can also be formed if drainage is too low. The drainage probability is modelled as being independent of soil properties. However, this is not reality. Soil is structured in different layers with different properties of percolation (one process of lake drainage). Some areas are covered with coarse grained sediments and others with fine grained sediments. Barren ground inhibits infiltration and allows only horizontal flow of water. Also small-scale topographic heterogeneities influence drainage of lakes. Thus, the reason for modelling too many lakes can

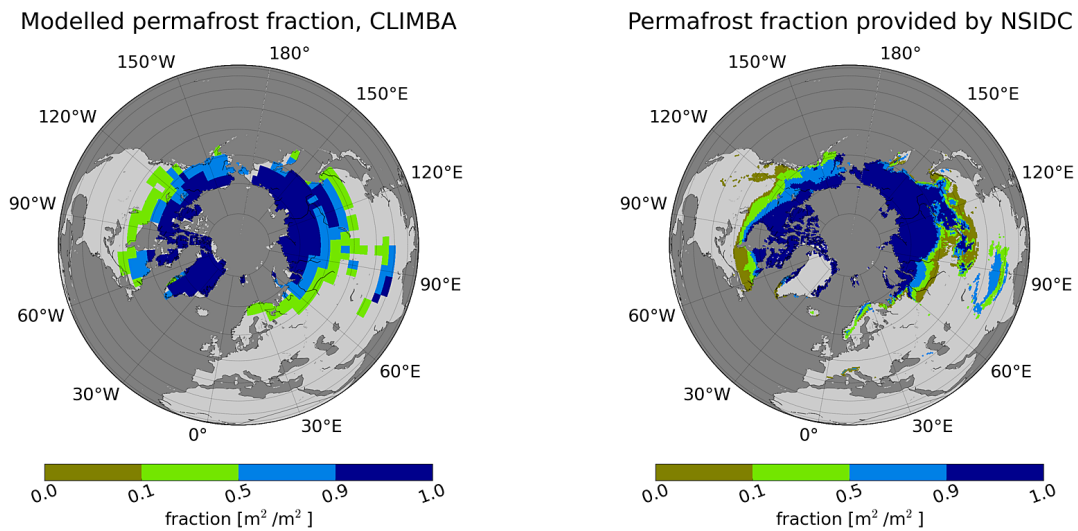


Figure 6.7: This figure shows the simulated permafrost fraction at pre-industrial times for CLIMBA forcing (left panel) and observed permafrost fraction from NSIDC (Brown et al., 1998) (right panel).

either be because too many lakes are triggered due to disturbance events or because the drainage is too low. In northern Siberia between the Lena river and west of the river Yenissei, the TAPAS model overestimates formation of TKL. A lot of lakes are observed by ESACCI, where the soil consists of ice-rich sediments (NSIDC) (see Fig. 6.6). However, TAPAS simulates too large LF and too high IC. More excess-ice is melted and a larger surface area is covered with melting water. These regions are not completely flat like the western Siberian lowlands. The average slope ranges between 0.01 m/m and 0.02 m/m (see Fig. 6.6). Probably, limitation of excess-ice aggregation due to slope is underestimated in these areas.

The TAPAS model works best in typical regions for thermokarst. Those regions are the Lena river delta, the Mackenzie river delta, the north slope of Alaska, and the eastern Siberian lowlands (Grosse et al., 2013). The areas are flatlands with a slope of less than 0.01 m/m. TAPAS simulates high IC as observed by NSIDC. Also the observed high LF is well captured. The TAPAS model aims to follow the different steps of thermokarst. The model parameters were tuned to reach a reliable equilibrium between formation of new lakes and drainage of old lakes and between LF and IC.

The aim of this thesis was to simulate the today's distribution of TKL and to confine it within satellite based observations of water bodies. To decide if the TAPAS model fails the goal of the study the following question is asked. Are the modelled LFs significantly different from each other or from the ESACCI observation? This significance is tested with the two-sample Kolmogorov–Smirnov test. The modelled LF of each model run is clustered in $0.01 \text{ m}^2/\text{m}^2$ intervals between $0.0 \text{ m}^2/\text{m}^2$ and $0.36 \text{ m}^2/\text{m}^2$, which is the maximum LF as modelled with ECHAM5 or with CLIMBA forcing. Both model runs are significantly different from ESACII observations on the 99 % level, but they simulate a similar distribution of LF and are not significantly different on the 95 % level. To conclude, CLIMBA and ECHAM5 simulate the same climate and, therefore, in ideal case the modelled lake fraction would be the same. In

general, the observed areas with thermokarst are captured by the TAPAS model with respect to permafrost, excess-ice, and slope distributions. However, the regional distribution of lakes is significantly different from observations and shows potential for improvements due to regional over- and underestimations of lake fraction. The lake fraction is limited by soil properties like permafrost, slope, and excess-ice content. While permafrost is well captured, excess-ice is sometimes over- or underestimated leading to a discrepancy between observed and modelled lake fraction. Despite the problem with the regional distribution of TKL, the TAPAS model shows very good agreements to observations in lowlands with ice-rich permafrost soils like for instance the north slope of Alaska, in eastern Siberian lowlands, in the Lena river delta, and in the Mackenzie river delta.

7 Concluding remarks

7.1 Summary

Thermokarst is a coupled thermal–hydrological process, which leads to enhanced thawing of ice-rich permafrost soils. This study is motivated by the necessity to provide boundary conditions for biochemical modelling of methane and carbon-dioxide emissions in permafrost areas. The aim is to dynamically solve the water balance between excess-ice within the permafrost soil and the area covered with water at the surface. A larger number of thermokarst lakes (TKL) is expected by the end of this century due to Arctic-climate amplification. This dissertation focuses on the development of the first global-scale thermokarst model (TAPAS). TAPAS is used to investigate the potential impacts of climate warming on thermokarst.

The TAPAS successfully simulates the major steps of the thermokarst cycle on a global scale in accordance with previous research. New ponds are triggered by climate extreme events in response to disturbances of the soil's thermal balance. The ponds promote thawing during summer and impeded freezing-up during fall and winter. Within the TAPAS model, this mechanism is approximated with a parameterized initial increase of the maximum thawing depth. The ponds expand to large lakes over a time scale of several millennia. Sudden drainage events stop the expansion of lakes and empty basins are left, where permafrost recovers and excess-ice aggregates. The TAPAS model simulates processes over a wide range of lakes and basins. Their properties are highly dependent on age and on thermal as well as hydrological states. Therefore, the model includes an age class scheme to resolve the different physical mechanisms. Several parameters are introduced to approximate changes within the thermal and hydrological states.

In the experiments presented in this dissertation, TAPAS is forced with data from different Holocene runs to simulate the full cycle of thermokarst and permafrost changes over the past 6000 years until pre-industrial times. Several climate scenarios are designed with a prescribed climate change during a 100-year period. In the warming scenario, a large number of new ponds develop due to a higher number of disturbances. In this warming scenario, less excess-ice accumulates because the thawing depth increases; the area of evolving TKL decreases because less ice is melted. Permafrost fraction decreases. One stabilizing factor is lost and therefore drainage of lakes increases resulting in a smaller number of TKL. Furthermore, fewer areas are available for thermokarst because the southern boundary of permafrost shifts northward. The climate scenarios have shown thermokarst needs approximately 2200 years to adjust to a new climate state. Then a new equilibrium is reached between lakes and excess-ice.

In general, the observed areas with thermokarst are captured by the TAPAS model with respect to permafrost, excess-ice, and slope distributions. The modelled distribution of TKL is

evaluated against today's satellite based observations. There are two major uncertainties: On the one hand, satellites cannot distinguish between TKL and water bodies of different origin. On the other hand, the TAPAS model applies forcing data until pre-industrial times resulting in a time shift of about 150 years. The regional distribution of lakes is significantly different from observations and shows potential for improvements due to regional over- and underestimations of lake fraction. The TAPAS model however shows very good agreement to observations in lowlands with ice-rich permafrost soils, for instance in the north slope of Alaska and the eastern Siberian lowlands, the Lena river delta, and the Mackenzie River delta. The differences can be reduced by better representation of topographic heterogeneities with respect to excess-ice accumulation. The TAPAS model successfully simulates disturbance events on global scale, which are caused by high summer temperature, high winter snow depth, flooding, and wildfires. Regional climate and soil conditions are not considered within this model version, but may influence the sensitivity to different disturbance events and thus the number of TKL formed.

The main research questions stated in section 1.2 are answered as follows.

1. Which parameterizations are needed to model thermokarst on global scale? An age-class scheme is implemented to represent the different physical mechanisms behind the major steps of the thermokarst cycle. Parameterizations of following processes are important to simulate thermokarst on global scale. New ponds are formed with a prescribed initial area. Expansion rate increases with the area of a lake in four steps. Drainage probability changes exponentially with the age of a lake and with the permafrost fraction. Growth of excess-ice decreases over time and depends on the predefined time scale. In reality, also different soil and topographic properties influence drainage and expansion of lakes and new parameterizations are needed for consideration of the probability to connect to river networks or to subterranean drainage passages. Parameterization is required in respect to development of thermal contraction cracks during winter because they are a precondition for excess-ice aggregation in form of ice-wedges.
2. How does thermokarst respond to climate change? Generally, a time period of 2200 years is needed to reach a new equilibrium state. On a time scale of several millennia the total number and area of TKL increases in the cooling scenario and decreases in the warming scenarios. In the warming scenario, the number of lakes increases first due to a higher number of disturbances, but then decreases due to a larger drainage of lakes. On a time scale of several millennia, changes in lake-size distribution relate to changes within permafrost and excess-ice.
3. How has thermokarst potentially developed during the Holocene under different forcings? The TAPAS model is sensitive to forcing with respect to evolution of temperature over time, because air temperature drives permafrost area and therefore the potential area of excess-ice aggregation and thermokarst formation. Forced with CLIMBA, the total area of TKL in the Arctic (TAL) increases by 1 % from 6000 BP until pre-industrial times, and when forced with ECHAM5 by 13 %. With ECHAM5 forcing, TAL decreases until 5000 BP. Then it increases again and reaches a temporary peak in 2800 BP followed by a slight decrease. TAL increases then again from 1800 BP until pre-industrial times.

In this dissertation, a novel multi-process-based thermokarst model has been developed.

Thermokarst develops, where climate, area, and topographic slope are favourable. However, large biases occur on regional scale. By application of some modifications and implementation of further parameterizations for considering regional soil properties and climate conditions, it will be possible to implement the TAPAS model into an Earth system model and thus to substantially improve the process representation of permafrost-related small-scale processes in global models.

7.2 Outlook

The validation of the TAPAS model against observed lake fraction and ice content indicates potential for improvements with respect to formulation of different thermokarst processes and the evolution of TKL. The following suggestions may improve the model performance:

- Although the age classes are attributed with different slopes as derived from the sub-grid slope distribution function from Stacke and Hagemann (2012), the representation of topographic heterogeneities could be improved. The reason is that slope is averaged within one age class between the slope of entering lakes and the slope of remaining lakes. Thus, the slope approaches the average slope of all permafrost areas within one grid-cell. Therefore aggregation of excess-ice is limited by the average slope. The representation of topographic heterogeneities could be improved by computing the average limitation within one grid cell derived from the slope-distribution function.
- The slope limitation of excess-ice aggregation is prescribed as the cosine of the slope. Unfortunately, the relationship between slope and excess-ice could not be investigated, because ice data were not available in sequential but only in categorized form. Therefore, I suggest a further investigation of the excess-ice distribution.
- Disturbance events are computed as a function of anomaly above mean and standard deviation for all regions in the Arctic. Regional climate and soil conditions should be accounted in more detail. For instance, disturbances due to infiltration are best computed in months of snow-melt. However, the time-period of snow-melt varies over time and depends on regional climate conditions. A better representation of infiltration disturbances can be reached if the month with the largest snow melt is considered. The representation of summer-temperature disturbances may be improved by accounting for the thermal properties of the soil. Soil inherits different thermal properties depending on moisture and on organic-carbon content, which result in the different thermal properties of the soil. A larger heat conductivity leads to a higher temperature change and therefore to larger impact of extremely hot summers. Therefore, soil properties are of special interest for future studies accounting for calculation of summer-temperature disturbances.
- Unfortunately, it is not known, to which extent each type of disturbance event contributed to today's observed distribution of TKL. Long-term observations of lakes are needed to correlate changes in the number of lakes to chronologies of extreme events. Up to now this investigation was technically difficult because not enough data were available.
- Energy balance is not implemented in the context of this dissertation. Thawing and melting

are approximated with empirical functions based on results from simulations of single lakes in previous studies. The implementation of energy transfer will be a major task if the TAPAS model is coupled with a global ESM. The TAPAS model provides ice content and lake fraction on yearly time scale based on estimates of the excess-ice depth. Water fluxes can potentially be derived from changes within the excess-ice depth. Then, an energy balance can be derived between released and absorbed latent energy in thermokarst areas.

- The drainage probability of lakes is derived as an exponential function of the age of a single lake and of the permafrost fraction. It might potentially be improved by introducing a heat transfer scheme to determine insulation of the soil. A dynamical vegetation scheme could then be applied. Previous observation studies show that depressions form after a disturbance event due to the melting of excess-ice and soil subsidence. In the early stages, they are very shallow and vegetation can still grow there with the potential to provide higher insulation from the atmosphere and to reverse the thermokarst process. In comparison, if evaporation exceeds precipitation, then thermokarst is delayed only because depressions have already formed, which can be filled with water again. A delay within the development of TKL due to changes in the water balance did not significantly change the lake fraction.
- If the TAPAS model is coupled with an ESM it can be applied to obtain boundary conditions for biochemically computing the permafrost-carbon cycle. It would provide the area covered with lakes and thus the area where soil organic carbon is decomposed via aerobic or anaerobic processes.
- The TAPAS model is useful for studies concerning climate variations during glacial periods because a representation of shifts within the lake distribution can improve simulation of carbon-dioxide emissions in permafrost areas and thus changes of atmospheric CO₂ concentration during glacial periods. Since thermokarst develops on a time-scale of several millennia, the full natural variability of the total lake area in the Arctic is better investigated on a time period of several 1×10^4 years.
- The TAPAS model also allows an investigation of potential changes within the distribution of TKL on a shorter time-period of 100 years, for instance. One climate warming scenario was designed with a prescribed warming of 4 °C during the 100-year period between 5000 - 4900 BP. During this period, the total area of TKL decreased by 5 %, although more lakes were formed. Due to a larger drainage from lakes the total number of TKL decreased by 4 %. Thus, due to future climate warming the water-covered area may decrease due to changes in permafrost area and excess-ice depth, which will largely affect the hydrological state of periglacial environments.

List of Symbols

A_{ave}	...	Average area of lakes within one age class [m^2]
A_0	...	Initial area of new ponds [m^2]
A_{box}	...	Area of grid-cell [m^2]
A_{lakes}	...	Surface area of all lakes within one age class [m^2]
A_{land}	...	Land area of grid-cell [m^2]
A_{ratio}	...	Ratio of thermokarst affected area covered with water [m^2/m^2]
a_{infil}	...	Coefficient for retrieving number of disturbances due to <i>infil</i>
a_{wsnow}	...	Coefficient for retrieving number of disturbances due to SWE_{winter}
a_{stemp}	...	Coefficient for retrieving number of disturbances due to $T2M_{summer}$
b_{infil}	...	Coefficient for retrieving number of disturbances due to <i>infil</i>
b_{wsnow}	...	Coefficient for retrieving number of disturbances due to SWE_{winter}
b_{stemp}	...	Coefficient for retrieving number of disturbances due to $T2M_{summer}$
$burn$...	Burned area fraction of grid-cell [m^2/m^2]
C_{snow}	...	Heat capacity of snow
$dist_{exp}$...	Fraction of grid-cell disturbed due to expansion of thermokarst lakes [m^2/m^2]
$dist_{fract}$...	Fraction of grid-cell disturbed by thermokarst [m^2/m^2]
$drain$...	Drainage probability of lakes [##]
$drain_{100}$...	Drainage probability of lakes with an age of 100 years [##]
$drain_{1000}$...	Drainage probability of lakes with an age of 1000 years [##]
$drain_{ampl}$...	Drainage amplification due to decreasing permafrost [##]
$expand$...	Expansion rate of lakes [m/y]
$expand1$...	Expansion rate of lakes < 1 ha [m/y]
$expand2$...	Expansion rate of lakes > 1 ha [m/y]
$expand3$...	Expansion rate of lakes > 10 ha [m/y]
$expand4$...	Expansion rate of lakes > 40 ha [m/y]
F	...	Freezing index [-]
f	...	Cumulative fraction of one grid cell [m^2/m^2]
f_{zero}	...	Zero slope fraction of one grid cell [m^2/m^2]
FDD	...	Freezing Degree Days [$^{\circ}C$]
h_{lakes}	...	Average depth of all lakes within one age class [m]
h_{melt}	...	Melted thickness of ice layer [m]
h_{soil}	...	Height of subsided soil [m]
h_{talik}	...	Depth of talik [m]
ice_{ave}	...	Average ice content of a grid box [m/m]
ice_{cont}	...	Average ice content of one age class [m/m]
ice_{max}	...	Maximum ice content of soil [m/
$infil$...	Monthly infiltration rate between May and August [mm]
k_{burn}	...	Coefficient to compute number of disturbances due to <i>burn</i>
l_{summer}	...	Length of summer [d]
l_{winter}	...	Length of winter [d]
$lake_{esacci}$...	ESACCI observed fraction of grid-cell covered lakes [m^2/m^2]
$lake_{fract}$...	Fraction of grid-cell covered with thermokarst lakes [m^2/m^2]
$land_{fract}$...	Fraction of grid-cell covered with land [m^2/m^2]
n_{lakes}	...	Number of lakes [#]
$ndist_{burn}$...	Number of disturbances due to burned area fraction [#]

$ndist_{infil}$...	Number of disturbances due to high infiltration rate [#]
$nlakes_{new}$...	Total number of new thermokarst lakes triggered by disturbances [#]
$ndist_{stemp}$...	Number of disturbances due to high summer temperature [#]
$ndist_{wsnow}$...	Number of disturbances due to high winter snow-water-equivalent depth [#]
$pore_{size}$...	Pore-size of soil
r_{ave}	...	Average radius of lakes within one age class [m]
s_{max}	...	Maximum slope of one grid cell [m/m]
s_{minmod}	...	Virtual minimum slope derived from slope(f) [m/m]
s_{off}	...	Slope offset for correction of slope(f) [m/m]
$s(f)$...	Sub-grid slope distribution function [m/m]
$slope_{mean}$...	Average slope of one age class [m/m]
$stemp$...	Average summer air temperature between June and August [°C]
$surf$...	Yearly total surface runoff [mm]
SWE_{winter}	...	30-year mean winter snow water equivalent depth [m]
$T2M_{summer}$...	30-year mean temperature of summer season [°C]
$T2M_{winter}$...	30-year mean temperature of winter season [°C]
$T2M_{ymean}$...	Yearly mean air temperature [°C]
$T2M_{ymean_{snow}}$...	Yearly mean air temperature regarding the effect of snow [°C]
TDD	...	Thawing Degree Days [°C]
$thres_{ice1}$...	Upper threshold of ice formation [°C]
$thres_{ice2}$...	Threshold of pore size limitation [°C]
$thres_{ice3}$...	Lower threshold of ice formation [°C]
$thres_{infil}$...	Threshold for triggering thermokarst due to $infil$ [mm]
$thres_{wsnow}$...	Threshold for triggering thermokarst due to SWE_{winter} [m]
$thres_{surf}$...	Threshold for pausing early stage evolution of thermokarst lakes due to little surface runoff [mm]
$thres_{stemp}$...	Threshold for triggering thermokarst due to $T2M_{summer}$ [°C]
u_{winter}	...	Average wind speed during winter [m/s]
V_{ice}	...	Volume of accumulated excess-ice [m ³]
V_{ice}^{max}	...	Maximum volume of excess-ice [m ³]
V_{lakes}	...	Volume of water stored in all lakes within one age class [m ³]
$wsnow$...	Average snow water equivalent depth between November and April [m]
z_{ice}	...	Depth of accumulated ice [m]
z_{ice}^{max}	...	Maximum depth of excess-ice [m]
z_{snow}	...	Damping depth of snow [m]
α_{slope}	...	Angle corresponding to slope [rad]
α_{snow}	...	Thermal diffusivity of snow
λ_{snow}	...	Thermal conductivity of snow
Δ_{diff}	...	Difference of the discrepancies of modelled lake fraction between two model runs [m ² /m ²]
μ_{infil}	...	30-year long-term mean of monthly infiltration rate [mm]
μ_{stemp}	...	30-year long-term mean of average summer temperature [°C]
μ_{surf}	...	30-year long-term mean of total surface runoff [mm]
μ_{wsnow}	...	30-year long-term mean of average snow water equivalent depth [m]
ρ_{snow}	...	Density of snow [kg/m ³]
σ_{infil}	...	30-year long-term standard deviation of monthly infiltration rate [mm]
σ_{stemp}	...	30-year long-term standard deviation of average summer temperature [°C]
σ_{surf}	...	30-year long-term standard deviation of total surface runoff [mm]
σ_{wsnow}	...	30-year long-term standard deviation of average snow water equivalent depth [m]
τ	...	Time-scale of ice accumulation [y]

List of Abbreviations

ALD	...	Active Layer Depth
AWI	...	Alfred Wegener Institute
CH ₄	...	Methane
CLIMBER	...	CLIMate and BiosphERe Model
CMIP5	...	Coupled Model Intercomparison Project Phase 5
CO ₂	...	Carbondioxide
ECHAM	...	Atmospheric circulation model of the MPI-M, Hamburg
ECMWF	...	European Center for Medium-range Weather Forecast
ESA	...	European Space Agency
ESA-DUE	...	ESA Data User Element
ESM	...	Earth System Model
GCM	...	Global Climate Model
GHG	...	GreenHouse Gas
IPCC	...	Intergovernmental Panel on Climate Change
JSBACH	...	Jena Scheme for Both Atmosphere and Climate in Hamburg
MODIS	...	Moderate-resolution Imaging Spectroradiometer
MPI-M	...	Max-Planck-Institute for Meteorology
RCM	...	Regional Climate Model
PAGE21	...	changing Permafrost in the Arctic and its Global Effects in the 21 st century
PF	...	Permafrost Fraction
TAPAS	...	Thermokarst Affecting Permafrost And Soil
TKL	...	ThermoKarst Lake
WATCH	...	WATer and global CHange
WFD	...	WATCH Forcing Data

List of Figures

2.1	Arctic climate	8
2.2	Permafrost distribution and landscape	11
2.3	Vertical profile of permafrost	13
2.4	Thermokarst lakes	14
2.5	ESA-CCI water bodies	15
2.6	Stages of thermokarst process	17
2.7	Ice wedge polygons	18
3.1	Sketch of the thermokarst model	22
3.2	Area covered with water and slope	28
3.3	Potential limnicity	29
3.4	Permafrost Fraction	31
3.5	Comparison of PF models	33
3.6	Disturbances by summer temperature	36
3.7	Disturbances by wildfires	37
3.8	Disturbances by winter snow depth	38
3.9	Disturbances by infiltration	39
3.10	Age specific lakes properties	43
3.11	Observed and modelled ice content	49
3.12	Threshold of ice formation	50
3.13	Ice and slope distribution	55
4.1	Reference-1 lake fraction	62
4.2	Reference-1 ice content	63
4.3	Tuning ice accumulation time-scale	65
4.4	Tuning pore-size influence	66
4.5	Tuning expansion rates	68
4.6	Tuning drainage of older lakes	69
4.7	Tuning drainage of younger lakes	70
4.8	Reference-3 lake fraction and ice content	71
4.9	Ref-3 vs Ref-1 and NSIDC ice content	72
4.10	Tuning infiltration disturbance thresholds	73
4.11	Tuning temperature disturbance threshold	74
4.12	Tuning snow disturbance threshold	75
4.13	Tuning fire disturbance	76
4.14	Disturbance events computed with different b_{stemp}	77
4.15	Tuning temperature disturbance	78
4.16	Tuning number of disturbance events	79

4.17	Retuning pore-size influence and drainage amplification	80
4.18	Retuning initial area and ice aggregation time-scale	82
4.19	Retuning expansion rate and drainage after 1000 years	83
4.20	Retuning drainage after 100 years	84
5.1	Climate scenarios	86
5.2	Lake evolution under different climates modelled with constant permafrost areas	88
5.3	Lake number under different climates at two time-steps	90
5.4	Area of lakes under different climates at pre-industrial times	92
5.5	Thermokarst under different climates modelled with variable permafrost areas .	93
5.6	Lake fraction under different climates at pre-industrial times	97
6.1	Difference of annual mean temperature between pre-industrial times and 6000 BP	102
6.2	Time-series of annual mean temperature from CLIMBA and ECHAM5	103
6.3	Evolution of thermokarst lakes modelled with different forcing	104
6.4	Lake fraction modelled with CLIMBA and ECHAM5 forcing	106
6.5	Ice content and permafrost fraction modelled with CLIMBA and ECHAM5 forcing	107
6.6	Modelled ice content and slope	109
6.7	Modelled and observed permafrost fraction	110

List of Tables

2.1	NSIDC permafrost fraction	12
3.1	Structure of age classes	24
3.2	Development of talik	41
3.3	Drainage Probability	46
3.4	NSIDC ice content	49
4.1	Thermokarst model parameters	60
4.2	Tuning list of parameters	61
4.3	Tuning pore-size influence	66
4.4	Tuning expansion rates	67
4.5	Disturbance events: factor and exponent	77
4.6	Tuning number of disturbance events	79
4.7	Retune expansion rates	82
5.1	Arctic climate change in RCP-4.5 scenario	86
5.2	Overview of modelled climate scenarios	87
5.3	Evolution of lake area and number under different climates modelled with constant permafrost areas	89
5.4	Thermokarst under different climates modelled with variable permafrost areas .	93

Acknowledgements

I like to express my deepest gratitude to my supervisors Stefan Hagemann and Victor Brovkin, in particular for their guidance and scientific advice. Stefan and Victor have always been available for discussions and encouraged me a lot with their forbearing willingness to support me with my issues. I also thank my advisory panel chair Eva-Maria Pfeiffer for her large interest in my research. With her suggestions during the panel meetings, she kept me motivated for progressing with my work. They all have enabled me for a successful completion of my dissertation.

I am also thankful for the support from the staff of the International Max Planck Research School on Earth System Modelling, namely Antje Weitz, Cornelia Kampmann, and Wiebke Böhm. They helped a lot by taking care of all the administrative tasks involved during my dissertation. Especially I would like to thank Antje for her exceptional care of my progress and well-being.

Furthermore, I am very grateful to the former and current members of the Terrestrial-Hydrology working group for their personal and scientific support. Especially Tobias Stacke and Tanja Blome supported me a lot with their willingness to help. They never got tired of explaining complex coherencies of the topic in a comprehensible way. Therefore they played a major role for the successful completion of my dissertation. I would also like to thank Martin Claussen and the whole Land in the Earth System department for the inspiring working environment. I am also very thankful to some external colleagues of the PAGE21 project, namely Lars Kutzbach, Moritz Langer, and Sina Muster. They supported me a lot with their scientific advice and their interest in my research during and beyond the project meetings.

Moreover, I would like to thank my colleagues and friends of the Max-Planck-Institute for their scientific advice as well as for the pleasant time I could spend with them during lunch breaks, barbecue sessions, sport, and evening drinks. Many thanks to Andreas Veira, Cedrick Ansorge, Fabio Cresto-Aleina, Felix Wiß, Jian Peng, Jörg Burdanowitz, Matthias Bittner, Philipp de Vrese, Sebastian Müller and Thomas Keitzl.

Of course I like to thank my parents as well. They have supported me with their confidence and trust that I can carry out and finish my dissertation. I also want to thank my brothers and all my friends for the nice hours and experiences beside my study. Many thanks to my neighbours as well, who have made my stay in Hamburg as comfortable as possible.

Finally I like to express my gratitude to the entire Institute for making this doctorate a truly great experience.

Bibliography

- ACIA (2005). *Arctic Climate Impact Assessment*. Scientific Report 22. Cambridge University Press, 1042p. (Cit. on p. 1).
- Bartsch, A. et al. (2012). 'Final Report v2'. In: *ESA DUE Permafrost Deliverable* 19. (Cit. on p. 47).
- Battle, M. et al. (2000). 'Global carbon sinks and their variability inferred from atmospheric O₂ and $\delta^{13}\text{C}$ '. In: *Science* 287.5462, pp. 2467–2470. (Cit. on p. 2).
- Black, Robert F (1976). 'Periglacial features indicative of permafrost: ice and soil wedges'. In: *Quaternary Research* 6.1, pp. 3–26. (Cit. on pp. 19, 27, 41, 42, 48, 51).
- Brovkin, V. et al. (2002). 'Carbon cycle, vegetation, and climate dynamics in the Holocene: Experiments with the CLIMBER-2 model'. In: *Global Biogeochemical Cycles* 16.4, pp. 86–1. (Cit. on p. 101).
- Brovkin, V. et al. (2009). 'Global biogeophysical interactions between forest and climate'. In: *Geophysical Research Letters* 36.7. (Cit. on pp. 100, 101).
- Brown, J. et al. (1997). *Circum-Arctic map of permafrost and ground-ice conditions*. Washington, DC: U.S. Geological Survey in Cooperation with the Circum-Pacific Council for Energy and Mineral Resources. Tech. rep. CP-45. scale 1:10,000,000. Circum-Pacific Map Series. (Cit. on pp. 1, 11, 14).
- Brown, J. et al. (1998). *Circum-arctic map of permafrost and ground ice conditions*. Technical Reports 22. Boulder, CO: National Snow and Ice Data Center. (Cit. on pp. 4, 8, 9, 11, 12, 15, 29–31, 49, 50, 56, 57, 63, 87–89, 102, 103, 106, 109, 110).
- Bruecher, T. et al. (2014). 'Comparing modelled fire dynamics with charcoal records for the Holocene'. In: *Climate of the Past* 10, pp. 811–824. (Cit. on pp. 2, 4, 21, 36, 57, 91, 99, 101, 102).
- Burn, C.R. (2000). 'The thermal regime of a retrogressive thaw slump near Mayo, Yukon Territory'. In: *Canadian Journal of Earth Sciences* 37.7, pp. 967–981. (Cit. on p. 40).

- Ekici, A. et al. (2013). 'Improved soil physics for simulating high latitude permafrost regions by the JSBACH terrestrial ecosystem model'. In: *Geosci Model Dev Discuss* 6, pp. 2655–2698. (Cit. on p. 2).
- Fedorov, A.N. et al. (2014). 'Estimating the water balance of a thermokarst lake in the middle of the Lena River basin, eastern Siberia'. In: *Ecohydrology* 7.2, pp. 188–196. (Cit. on p. 24).
- Fischer, N. and J.H. Jungclaus (2010). 'Effects of orbital forcing on atmosphere and ocean heat transports in Holocene and Eemian climate simulations with a comprehensive Earth system model'. In: *Climate of the Past* 6, pp. 155–168. (Cit. on pp. 2, 4, 99–101).
- French, H.M. (2007). *The Periglacial Environment*. Wiley. ISBN: 9780470865903. (Cit. on pp. 1, 2, 9, 10, 12–20, 27, 45, 48).
- Ganopolski, A. et al. (2001). 'CLIMBER-2: a climate system model of intermediate complexity. Part II: model sensitivity'. In: *Climate Dynamics* 17.10, pp. 735–751. (Cit. on p. 101).
- Gesch, D.B. et al. (1999). 'New land surface digital elevation model covers the Earth'. In: *EOS, Transactions American Geophysical Union* 80.6, pp. 69–70. (Cit. on p. 54).
- Grosse, G. et al. (2008). 'Distribution of thermokarst lakes and ponds at three Yedoma sites in Siberia'. In: *Proceedings of the 9th International Conference on Permafrost, Fairbanks, USA*, 551–556. (Cit. on pp. 14, 23).
- Grosse, G. et al. (2011). 'Vulnerability of high-latitude soil organic carbon in North America to disturbance'. In: *Journal of Geophysical Research: Biogeosciences (2005–2012)* 116.G4. (Cit. on pp. 1, 2, 27, 34, 45).
- Grosse, G. et al. (2013). 'Thermokarst lakes, drainage, and drained basins'. In: (cit. on pp. 1, 14, 64, 95, 108, 110).
- Hagemann, S. and L.D. Gates (2003). 'Improving a subgrid runoff parameterization scheme for climate models by the use of high resolution data derived from satellite observations'. In: *Climate Dynamics* 21.3-4, pp. 349–359. (Cit. on p. 54).
- Hagemann, S. and T. Stacke (2014). 'Impact of the soil hydrology scheme on simulated soil moisture memory'. In: *Climate Dynamics* 44.7-8, pp. 1731–1750. (Cit. on p. 38).
- Hinkel, K.M. et al. (2007). 'Methods to assess natural and anthropogenic thaw lake drainage on the western Arctic coastal plain of northern Alaska'. In: *Journal of Geophysical Research: Earth Surface (2003–2012)* 112.F2. (Cit. on pp. 27, 45).
- Hinzman, L.D. et al. (2005). 'Evidence and implications of recent climate change in northern Alaska and other arctic regions'. In: *Climatic Change* 72.3, pp. 251–298. (Cit. on p. 1).

- Hopkins, David M. (1949). 'Thaw lakes and thaw sinks in the Imuruk Lake area, Seward Peninsula'. In: *The Journal of Geology* 57.2, pp. 119–131. (Cit. on p. 1).
- Huissteden, J. van et al. (2011). 'Methane emissions from permafrost thaw lakes limited by lake drainage'. In: *Nature Climate Change* 1.2, pp. 119–123. ISSN: 1758-678X. DOI: 10.1038/NCLIMATE1101. (Cit. on p. 4).
- IPCC (2007). *Contribution of Working Group I to the Fourth Assessment Report of the Intergovernmental Panel on Climate Change*. Ed. by S. Solomon et al. Cambridge, UK and New York, USA: Cambridge University Press. (Cit. on p. 1).
- (2014). *Climate Change 2013: The physical science basis: Working group I contribution to the fifth assessment report of the Intergovernmental Panel on Climate Change*. Cambridge University Press. (Cit. on p. 86).
- Johnston, G.H. and R.J.E. Brown (1961). 'Effect of a lake on distribution of permafrost in the Mackenzie River Delta'. In: (cit. on p. 40).
- Jones, B.M. et al. (2011). 'Modern thermokarst lake dynamics in the continuous permafrost zone, northern Seward Peninsula, Alaska'. In: *Journal of Geophysical Research: Biogeosciences* (2005–2012) 116.G2. (Cit. on pp. 23, 24, 27, 42, 44–47, 58, 62, 69).
- Jorgenson, M. Torre et al. (2010). 'Resilience and vulnerability of permafrost to climate change'. In: *Canadian Journal of Forest Research* 40, 1219–1236. (Cit. on p. 1).
- Kessler, M.A. et al. (2012). 'Simulating the decadal-to millennial-scale dynamics of morphology and sequestered carbon mobilization of two thermokarst lakes in NW Alaska'. In: *Journal of Geophysical Research: Biogeosciences* (2005–2012) 117.G2. (Cit. on pp. 4, 23, 27, 40, 41, 48, 51).
- Konrad, Jean-Marie (1990). 'Theoretical modelling of massive icy beds'. In: *Proceedings of the Fifth Canadian Permafrost Conference, Quebec City, Canada, Coll. Nord*. Vol. 54, pp. 31–35. (Cit. on pp. 27, 41).
- Kubny, H. (Aug. 2014). *Arktis - Überraschende Klimabilanz*. <http://www.polarnews.ch/arktis/forschung-umwelt/705-arktis-ueberraschende-klimabilanz>. (Cit. on p. 14).
- Lehner, B. and P. Döll (2004). 'Development and validation of a global database of lakes, reservoirs and wetlands'. In: *Journal of Hydrology* 296.1, pp. 1–22. (Cit. on p. 14).
- Ling, F. and T. Zhang (2003). 'Numerical simulation of permafrost thermal regime and talik development under shallow thaw lakes on the Alaskan Arctic Coastal Plain'. In: *Journal of Geophysical Research: Atmospheres* (1984–2012) 108.D16. (Cit. on p. 4).

- Marsland, S.J. et al. (2003). 'The Max-Planck-Institute global ocean/sea ice model with orthogonal curvilinear coordinates'. In: *Ocean modelling* 5.2, pp. 91–127. (Cit. on p. 100).
- Morgenstern, A. et al. (2011). 'Spatial analyses of thermokarst lakes and basins in Yedoma landscapes of the Lena Delta'. In: *The Cryosphere Discussions* 5, pp. 1495–1545. (Cit. on pp. 5, 16, 17, 27, 44, 50).
- Muster, S. et al. (2012). 'Subpixel heterogeneity of ice-wedge polygonal tundra: a multi-scale analysis of land cover and evapotranspiration in the Lena River Delta, Siberia'. In: *Tellus B* 64. (Cit. on p. 5).
- Nelson, F.E. and S.I. Outcalt (1983). 'A frost index number for spatial prediction of ground-frost zones'. In: *Permafrost-Fourth International Conference Proceedings*. Vol. 1, pp. 907–911. (Cit. on p. 30).
- (1987). 'A computational method for prediction and regionalization of permafrost'. In: *Arctic and Alpine Research*, pp. 279–288. (Cit. on pp. 30–32).
- Pelletier, J.D. (2005). 'Formation of oriented thaw lakes by thaw slumping'. In: *Journal of Geophysical Research: Earth Surface* (2003–2012) 110.F2. (Cit. on p. 4).
- Petoukhov, V. et al. (2000). 'CLIMBER-2: a climate system model of intermediate complexity. Part I: model description and performance for present climate'. In: *Climate dynamics* 16.1, pp. 1–17. (Cit. on pp. 101, 102).
- Pidwirny, M. (2006). *Periglacial Processes and Landforms*. <http://www.physicalgeography.net/fundamentals/10ag.html>. (Cit. on p. 13).
- Plug, L.J. and J.J. West (2009). 'Thaw lake expansion in a two-dimensional coupled model of heat transfer, thaw subsidence, and mass movement'. In: *Journal of Geophysical Research: Earth Surface* (2003–2012) 114.F1. (Cit. on p. 4).
- Péwé, R.J.E. and T.L. Brown (1973). 'Distribution of permafrost in North America and its relationship to the environment: a review, 1963-1973'. In: *Permafrost: North American Contribution [to The] Second International Conference*. Vol. 2. National Academies, p. 71. (Cit. on p. 12).
- Péwé, T.L. (1983). 'Alpine permafrost in the contiguous United States: a review'. In: *Arctic and Alpine Research*, pp. 145–156. (Cit. on p. 13).
- Raddatz, T.J. et al. (2007). 'Will the tropical land biosphere dominate the climate–carbon cycle feedback during the twenty-first century?' In: *Climate Dynamics* 29.6, pp. 565–574. (Cit. on pp. 100, 101).

- Reick, CH. et al. (2013). 'Representation of natural and anthropogenic land cover change in MPI-ESM'. In: *Journal of Advances in Modeling Earth Systems* 5.3, pp. 459–482. (Cit. on p. 101).
- Roeckner, E. et al. (2003). 'The atmospheric general circulation model ECHAM 5. PART I: Model description'. In: (cit. on p. 100).
- Romanovsky, V.E. et al. (2010). 'Permafrost thermal state in the polar Northern Hemisphere during the international polar year 2007–2009: a synthesis'. In: *Permafrost and Periglacial Processes* 21.2, pp. 106–116. (Cit. on p. 1).
- Santoro, M. et al. (submitted). 'Strengths and weaknesses of multi-year Envisat ASAR backscatter measurements to map permanent open water bodies at global scale'. In: *Remote Sensing of Environment*. (Cit. on pp. 3, 14, 15, 64, 105, 106).
- Schirrmeister, L. et al. (2011). 'Sedimentary characteristics and origin of the Late Pleistocene Ice Complex on north-east Siberian Arctic coastal lowlands and islands - A review'. In: *Quaternary International* 241, pp. 3–25. DOI: 10.1016/j.quaint.2010.04.004. (Cit. on p. 1).
- Schuur, E.A.G. et al. (2008). 'Vulnerability of permafrost carbon to climate change: Implications for the global carbon cycle'. In: *BioScience* 58.8, pp. 701–714. (Cit. on p. 2).
- Smith, L.I.C. et al. (2005). 'Disappearing arctic lakes'. In: *Science* 308.5727, pp. 1429–1429. (Cit. on pp. 60, 94).
- Stacke, T. and S. Hagemann (2012). 'Development and validation of a global dynamical wetlands extent scheme'. In: *Hydrology and Earth System Sciences Discussions* 16, pp. 2915–2933. (Cit. on pp. 2, 23, 29, 30, 50, 51, 54, 55, 108, 109, 115).
- Taylor, A.E. et al. (2008). 'Thermal impact of Holocene lakes on a permafrost landscape, Mackenzie Delta, Canada'. In: *Ninth International Conference on Permafrost, Univ. of Alaska Fairbanks, Fairbanks*. (Cit. on p. 4).
- Thieler, E.R. et al. (2009). *The Digital Shoreline Analysis System (DSAS) Version 4.0-An ArcGIS Extension for Calculating Shoreline Change*. Tech. rep. US Geological Survey. (Cit. on p. 42).
- Tricart, Jean (1968). 'PERIGLACIAL LANDSCAPES Periglacial landscapes'. In: *Geomorphology*. Springer, pp. 829–833. (Cit. on p. 9).
- Van Everdingen, R.O. (1998). *Multi-language glossary of permafrost and related ground-ice terms*. Boulder, CO: National Snow Ice Data Center for Glaciology. (Cit. on pp. 7, 16).
- Wallace, Robert E. (1948). 'Cave-In Lakes in the Nabesna, Chisana, and Tanana River Valleys, Eastern Alaska'. In: *The Journal of Geology* 56.3, pp. 171–181. (Cit. on p. 1).

- Walter, K.M. et al. (2007). 'Methane bubbling from northern lakes: present and future contributions to the global methane budget'. In: *Philosophical Transactions of the Royal Society of London A: Mathematical, Physical and Engineering Sciences* 365.1856, pp. 1657–1676. (Cit. on p. 1).
- Washburn, A.L. (1980). 'Permafrost features as evidence of climatic change'. In: *Earth-Science Reviews* 15.4, pp. 327–402. (Cit. on pp. 19, 20, 49, 50, 67).
- Weedon, G.P. et al. (2011). 'Creation of the WATCH forcing data and its use to assess global and regional reference crop evaporation over land during the twentieth century'. In: *Journal of Hydrometeorology* 12.5, pp. 823–848. (Cit. on pp. 8, 9, 49, 50).
- West, J.J. and L.J. Plug (2008). 'Time-dependent morphology of thaw lakes and taliks in deep and shallow ground ice'. In: *Journal of Geophysical Research: Earth Surface* (2003–2012) 113.F1. (Cit. on pp. 4, 23, 40, 41, 51).
- Yi, S et al. (2014). 'Freeze/thaw processes in complex permafrost landscapes of northern Siberia simulated using the TEM ecosystem model: impact of thermokarst ponds and lakes'. In: *Geoscientific Model Development* 7.4, pp. 1671–1689. (Cit. on pp. 24, 25, 27, 40, 44, 51).
- Yoshikawa, K. and L.D. Hinzman (2003). 'Shrinking thermokarst ponds and groundwater dynamics in discontinuous permafrost near Council, Alaska'. In: *Permafrost and Periglacial Processes* 14.2, pp. 151–160. (Cit. on p. 45).
- Zhang, T. et al. (1999). 'Statistics and characteristics of Permafrost and ground ice Distribution in the Northern Hemisphere'. In: *Polar Geography* 23.2, pp. 132–154. (Cit. on pp. 1, 11).
- Zhou, W. and S.L. Huang (2004). 'Modeling impacts of thaw lakes to ground thermal regime in northern Alaska'. In: *Journal of cold regions engineering* 18.2, pp. 70–87. (Cit. on p. 4).

